NAVAL POSTGRADUATE SCHOOL

Monterey, California

THESIS

THE ONSET OF BREAKDOWN IN A FAST PULSED VACUUM DIODE

by

Michael P. Hallal, Jr

June, 1991

Thesis Advisor: F. Schwirzke

Approved for public release; distribution is unlimited

SECURITY CLASSIFICATION OF THIS PAGE

REPORT DOCUMENTATION PAGE

1a. REPORT SECURITY CLASSIFICATION Unclassified	1b. RESTRICTIVE MARKINGS
2a. SECURITY CLASSIFICATION AUTHORITY	3. DISTRIBUTION/AVAILABILITY OF REPORT Approved for public release; distribution is unlimited.
2b. DECLASSIFICATION/DOWNGRADING SCHEDULE	
4. PERFORMING ORGANIZATION REPORT NUMBER(S)	5. MONITORING ORGANIZATION REPORT NUMBER(S)
6a. NAME OF PERFORMING ORGANIZATION Naval Postgraduate School 6b. OFFICE SYMBOL (*If applicable*) 33	7a. NAME OF MONITORING ORGANIZATION Naval Postgraduate School
6c. ADDRESS (*City, State, and ZIP Code*) Monterey, CA 93943-5000	7b. ADDRESS (*City, State, and ZIP Code*) Monterey, CA 93943-5000
8a. NAME OF FUNDING/SPONSORING ORGANIZATION 8b. OFFICE SYMBOL (*If applicable*)	9. PROCUREMENT INSTRUMENT IDENTIFICATION NUMBER
8c. ADDRESS (*City, State, and ZIP Code*)	10. SOURCE OF FUNDING NUMBERS Program Element No. / Project No. / Task No. / Work Unit Accession Number

11. TITLE (*Include Security Classification*)
THE ONSET OF BREAKDOWN IN A FAST PULSED VACUUM DIODE

12. PERSONAL AUTHOR(S) Michael P. Hallal, Jr.

13a. TYPE OF REPORT	13b. TIME COVERED	14. DATE OF REPORT (*year, month, day*)	15. PAGE COUNT
Master's Thesis	From To	June 1991	128

16. SUPPLEMENTARY NOTATION
The views expressed in this thesis are those of the author and do not reflect the official policy or position of the Department of Defense or the U.S. Government.

17. COSATI CODES			18. SUBJECT TERMS (*continue on reverse if necessary and identify by block number*)
FIELD	GROUP	SUBGROUP	onset of breakdown, vacuum diode, whisker

19. ABSTRACT (*continue on reverse if necessary and identify by block number*)

The mechanism by which plasma forms in a fast pulsed vacuum diode is not yet well understood. The most popular model of the phenomenon is the explosive emission model. Current densities required by the explosive emission model are much larger than can be provided by space charge limited currents. This study presents experimental results to support a new model which takes into account the ion current density resulting from ionization processes in front of the cathode surface. It is shown that ion heating of the surface is several orders of magnitude more efficient than Joule heating in exploding a whisker. The treatment of the model for an ideal diode predicts the voltage at which plasma formation begins. It also predicts the time delay between the voltage onset and the onset of plasma formation. The voltage at which the onset of plasma formation occurs and the time delay between the voltage onset and the plasma onset have been experimentally determined in this work. The experimental results compare favorably to the new model.

20. DISTRIBUTION/AVAILABILITY OF ABSTRACT	21. ABSTRACT SECURITY CLASSIFICATION	
☒ UNCLASSIFIED/UNLIMITED ☐ SAME AS REPORT ☐ DTIC USERS	Unclassified	
22a. NAME OF RESPONSIBLE INDIVIDUAL F.Schwirzke	22b. TELEPHONE (*Include Area code*) (408) 646-2635	22c. OFFICE SYMBOL PhSw

DD FORM 1473, 84 MAR 83 APR edition may be used until exhausted
All other editions are obsolete

SECURITY CLASSIFICATION OF THIS PAGE
Unclassified

Approved for public release; distribution is unlimited.

The Onset of Breakdown in a Fast Pulsed Vacuum Diode

by

Michael P. Hallal, Jr.
Lieutenant, United States Navy
B.S., Tulane University, 1984

Submitted in partial fulfillment
of the requirements for the degree of

MASTER OF SCIENCE IN PHYSICS

from the

NAVAL POSTGRADUATE SCHOOL
June 1991

ABSTRACT

The mechanism by which plasma forms in a fast pulsed vacuum diode is not yet well understood. The most popular model of the phenomenon is the explosive emission model. Current densities required by the explosive emission model are much larger than can be provided by space charge limited currents. This study presents experimental results to support a new model which takes into account the ion current density resulting from ionization processes in front of the cathode surface. It is shown that ion heating of the surface is several orders of magnitude more efficient than Joule heating in exploding a whisker. The treatment of the model for an ideal diode predicts the voltage at which plasma formation begins. It also predicts the time delay between the voltage onset and the onset of plasma formation. The voltage at which the onset of plasma formation occurs and the time delay between the voltage onset and the plasma onset have been experimentally determined in this work. The experimental results compare favorably to the new model.

TABLE OF CONTENTS

ACKNOWLEDGEMENT

I would like to extend my deepest appreciation to those who helped make this report possible. I thank Dr. Fred Schwirzke for his theoretical guidance and for inspiring the experiment. I thank Dr. Xavier Maruyama for his experimental guidance and support. I thank Mr. Harold Rietdyk for his technical help and extreme patience during the setup and conduct of the experiment. Harold was always available to help me and to operate the Flash X-Ray machine for the experiment. I thank Mr. George Jaksha for machining all of the modifications to the Flash X-Ray machine and Mr. B. Bernstein of Physics International Company for his technical advice in the design of the modifications. I also thank Mr. Robert Sanders, Mr. Donald Snyder, and Mr. Dale Galarowicz for their technical support during this project as well as their contributions to the maintenance and operations of the FXR and other Physics Department resources.

Michael P. Hallal, Jr.

6 June 1991

I. INTRODUCTION

Pulsed power technology is a rapidly growing field with numerous applications ranging from controlled thermonuclear fusion experiments to strategic defense research. Breakdown and plasma formation on electrode surfaces is a fundamental process in pulsed power technology and is therefore of great interest to both researchers and practitioners of pulsed power [Ref. 1]. Sources of high current, high voltage particle beams operate during the time period between plasma formation and diode gap closure [Ref. 2]. This makes the understanding and prediction of the onset of plasma formation essential. Though the breakdown process in diodes has been studied extensively since the 1920's, the onset of plasma formation in a fast pulsed vacuum diode is not yet well understood [Ref.2]. If the physics of the breakdown process can be understood, it may be possible to design diodes which have the precise characteristics required by the application.

Previous work at the Naval Postgraduate School Flash X-Ray facility has shown that unipolar arc craters are formed on the cathode surface of a fast pulsed vacuum diode [Ref. 3]. These craters are the result of plasma interactions with a metal surface [Ref.3] and thus indicate that a plasma was present during the operation of the diode.

The purpose of this study is to describe the processes involved in the onset of plasma formation in the fast pulsed vacuum diode.

This work has two major parts. The first part describes a simple theoretical model for plasma formation in a highly idealized vacuum diode. This model makes quantitative predictions for the time delay of the onset of plasma formation. The second part describes an experiment performed to time resolve the plasma formation process in an actual fast pulsed vacuum diode. In particular, two pieces of data will be obtained from the experiment. First is the time delay between the onset of the voltage pulse across the diode and the onset of plasma formation. This data will be compared for different operating voltages of the diode. From the time delay information, it will be possible to determine the voltage across the diode at which plasma formation begins. The actual time delay and voltage at onset can then be compared to those predicted by the model. In addition to the time resolved data, time lapsed photographs (taken with shutter open for entire diode discharge process) will be used to give qualitative data about the diode plasma.

The vacuum diode used in the experiment is the diode of the Naval Postgraduate School Flash X-ray machine. Modifications were made to the Flash X-ray machine to allow the observation of plasma formation. These modifications will be described fully as part of this thesis.

II. REVIEW OF PLANAR DIODE PHYSICS

A planar diode is composed of two large parallel planar electrodes separated by a distance which is small as compared to the dimensions of the electrodes. Though many diodes used in applications are not actually planar diodes, it is still instructive to study the physics of the planar diode. Each of the following sections will discuss a different aspect of the planar diode.

A. RELATIVISTIC PLANAR DIODE

A diode is considered relativistic if a charged particle (usually an electron) in the diode gap is accelerated to speeds comparable to the speed of light. The most common way to characterize the relativistic property of a charged particle is through the dimensionless Lorentz parameter, γ. γ for a given particle with velocity v is defined as

$$\gamma = \frac{1}{\sqrt{1 - \frac{v^2}{c^2}}} \qquad (2.1)$$

where c is the speed of light in a vacuum. For a charged particle in an electric field γ is given by

$$\gamma = \gamma_0 + \frac{e\Phi}{mc^2} \qquad (2.2)$$

where γ_0 is the γ of the particle when it enters the electric field, e is the magnitude of the charge, Φ is the magnitude of the electric potential at the particle's position ,and m is the rest mass of the particle. For small values of γ (say near 1), the particle behaves non relativistically. For large values of γ (say near 100), the particle is extremely relativistic. Figure 2.1 provides a comparison of the

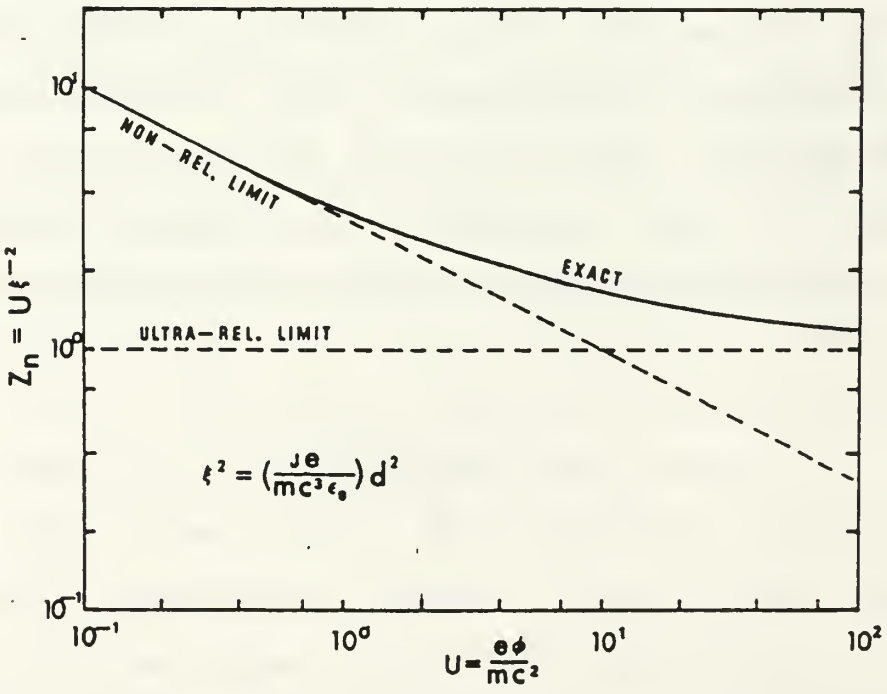

Figure 2.1 A comparison of the relativistic and non-relativistic solutions for the impedance of a one-dimensional planar diode [Ref. 4].

normalized diode impedance for the relativistic and non-relativistic planar diode. Z_n is the normalized diode impedance and is given by $Z_n=U/\xi^2$, where $U=e\Phi/mc^2$ and $\xi^2=[je/(mc^3\epsilon_o)]d^2$. Figure 2.1 is useful to find the diode potential at which the behavior of a charged particle traversing a planar diode departs from the non-relativistic limit. [Ref. 4]

B. ELECTRIC FIELD

The electric field, E, in a planar diode with no current through the diode is given by

$$E = \frac{\Phi_o}{d} \tag{2.3}$$

where Φ_o is the voltage applied across the diode, and d is the anode-cathode spacing of the diode. Once a current begins to flow through the diode, the electric field and hence the electric potential distribution in the diode are altered by the presence of "electron space charge" (see Figure 2.2) [Ref. 4].

C. FIELD EMISSION OF ELECTRONS

Electrons will be emitted into the vacuum diode from the cold cathode if the applied electric field is sufficiently strong ($E > 10^9$ V/m) [Ref.2]. This effect is known as field emission and it is described by the Fowler-Nordheim (FN)

equation. The FN equation is a complicated expression which will not be covered here. The important result of the FN equation is the functional relationship between the field emitted current density and the electric field strength. This relationship is given by

$$j_{fe} = c_1 \beta^2 E^2 \exp\left(-\frac{C_2}{\beta E}\right) \qquad (2.4)$$

where j_{fe} is the field emitted current density, β is the field

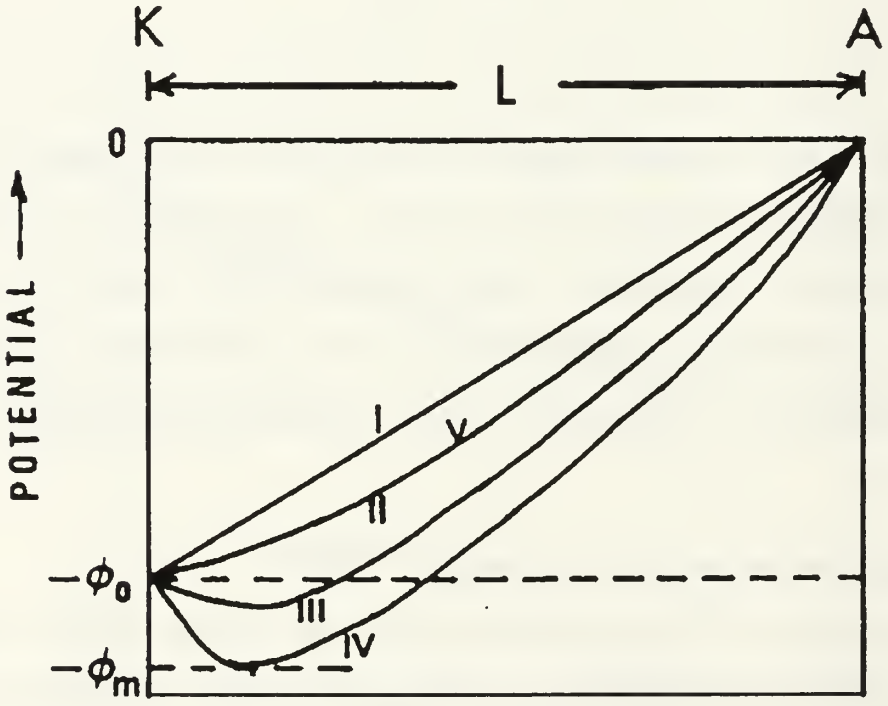

Figure 2.2 Electrostatic potential in diode including electron space charge. A time dependent potential minimum forms near cathode(K) surface. I through V are sequential in time. Anode(A) is distance L from K. [Ref. 4]

enhancement factor, and c_1 and c_2 are constants. For large values of electric field j_{fe} is essentially proportional to E^2.

D. SPACE CHARGE LIMITED CURRENT DENSITY

The buildup of space charge due to current flowing through the diode limits the maximum current density which can flow from one electrode to the other. A fully relativistic treatment of this phenomenon for a planar diode leads to the relativistic Child-Langmuir equation [Ref.4]. This equation is quite complicated. In the non-relativistic limit, which is sufficient for the conditions of the experiment in Chapter IV (e.g., U≤3 in Figure 2.1), the Child-Langmuir current density limit is given by

$$j_{CL} = \frac{4}{9}\epsilon_o\left(2\frac{e}{m}\right)^{\frac{1}{2}}\frac{\Phi_o^{\frac{3}{2}}}{d^2} \qquad (2.5)$$

where ϵ_o=8.85x10^{-12} F/m is the permittivity of free space, e is the magnitude of charge of the charge carriers, m is the mass of the charge carrier, Φ_o is the magnitude of the electric potential across the diode, and d is the distance the charge carriers must travel from the zero potential surface to the potential Φ_o. Before plasma formation begins, d is simply the distance between the electrodes.

E. PARAPOTENTIAL FLOW

High currents through the diode can result in a significant azimuthal self magnetic field. This magnetic field may result in a self focusing effect (especially for electron flow). The effect is commonly referred to as the parapotential flow. Parapotential flow drastically complicates calculations. Therefore, it is important to know when the effect can be ignored. The critical electron current through the diode below which parapotential flow can be neglected is given by

$$I_c = 2\pi\epsilon_o \frac{\gamma mc^3}{e} \frac{r_c}{d} \qquad (2.6)$$

where r_c is the cathode radius, and d is the anode-cathode spacing [Ref. 4]. For the conditions of the NPS Flash X-ray Machine, the self magnetic field is negligible and parapotential flow is not important.

III. MODEL FOR CATHODE SPOT FORMATION

A. PROBLEM WITH THE WHISKER EXPLOSIVE EMISSION MODEL

One popular model to describe the formation of cathode spots is the whisker explosive emission model [Ref. 5]. In this model, a voltage is applied across a vacuum diode which has micron sized protrusions (whiskers) on the cathode surface. The electric field in the diode is enhanced near the whiskers thus causing field emission of electrons from the whiskers. The whisker explosive emission model requires that the field emitted current (Equation 2.4) heats the whisker within nanoseconds until an explosive formation of plasma occurs. From there on the current to the anode is space charge limited with the current density j_{CL} as given by Equation 2.5.

In general one would expect that $j_{fe} << j_{CL}$. The Child-Langmuir current to the anode represents an upper limit. For example, a diode voltage of 1 MV and a gap of 2.54 cm, produces a uniform electric field of $E=3.9\times10^{7}$ V/m (Equation 2.3). Equation 2.5 gives $j_{CL}=3.6\times10^{6}$ A/m^2. This is much smaller than the $j_{FE}\approx10^{12}$-10^{13} A/m^2 required to explode a whisker by joule heating within a few nanoseconds [Ref. 6]. The field emitted electron current will become space charge limited at a value which is insufficient for the explosive

like transition of the whisker into a dense plasma. Furthermore, the externally applied electric field vanishes near the cathode surface when the current becomes space charge limited. This should turn off the field emission current. The question, then, is how can the relatively small field emission current lead to the "explosive" formation of a cathode spot within nanoseconds? This discrepancy can not be explained with the whisker explosive model.

B. CONDITIONS INSIDE A DIODE

Electrode surfaces are usually far from ultra high vacuum clean. Adsorbates are weakly bound to the surface by van der Waals interactions, ~0.25 eV/molecule. Whiskers, dust particles, oxide spots and similar microscopic nonuniformities provide enhanced field emission of electrons if a sufficiently high electric field, $E > 10^7$ V/m is applied. The electric field, the emission of electrons, and the impact of ions stimulate desorption. Moving with sound velocity $v \approx 330$ m/s, a suddenly released monolayer of 2×10^{19} molecules/m^2 forms a dense neutral gas layer. After an arbitrary time of 3 nanoseconds, the average particle density of the neutrals is $n_o=(2\times10^{19}/m^2)/vt=2\times10^{25}/m^3$ with $vt=1.0\times10^{-6}$ m. For comparison, the atmospheric particle density at 0° C is 2.7×10^{25} m^{-3}. The field emitted electrons will begin to ionize the desorbed neutral gas layer when the cross section for ionization becomes sufficient (see Figure 3.1). [Ref. 7]

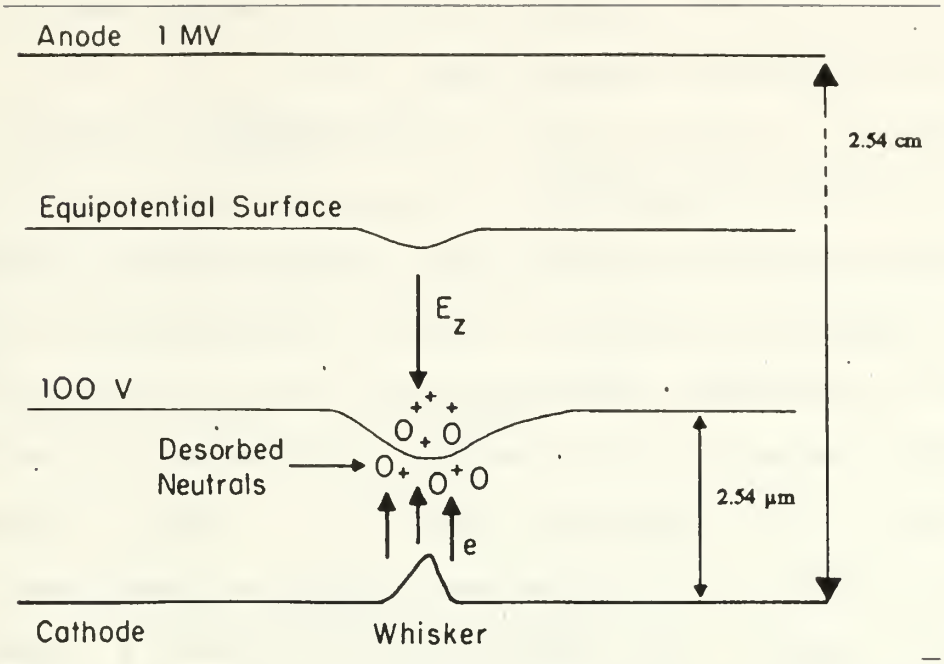

Figure 3.1. Ionization of desorbed neutrals near the 100 V equipotential surface where the ionization cross section has its maximum value [Ref. 7].

C. DESCRIPTION OF NEW MODEL

This model describes the early stages prior to the formation of a plasma and breakdown of a vacuum diode. One dimensional geometry is used in which the distance z is measured perpendicular to the cathode surface. The diode has a gap of 2.54 cm and a 1.0 MV potential applied. This produces an electric field of $E=3.9\times10^{7}$ V/m which is assumed to be uniform and constant in the model. At z=2.54 μm the potential is 100 volts. A source of field emitted electrons is present, presumably from a whisker. These emitted electrons are accelerated toward the anode by the electric field. These

electrons cause desorption of neutrals from the surface which in turn can then be ionized [Ref. 7].

Figure 3.2 depicts what may be a typical ionization cross section as it changes with the energy gained by the electrons as they accelerate away from the cathode surface. Figure 3.2 also schematically depicts a neutral density profile for the onset of ionization. The cross section for ionization of the neutrals (assumed to be oxygen) by the electrons is maximum at the 100 volt potential [Ref. 8]. The "ionization region" is the region where the ionization cross section and neutral density are sufficient to have a reasonable probability for ionization of neutrals. This region is approximated as having a thickness of d=1 μm and is centered on the 100 volt potential.

On average the ions are produced at z=2.54 μm. These ions are accelerated toward the whisker and deliver 100 eV of energy each to the surface layer. This surface layer may be many monolayers thick. The surface layer is heated by ion bombardment as well as by ohmic heating (see Figure 3.3).

D. CALCULATION BASED ON NEW MODEL

1. Time Frames of Interest

Since the 100 volt potential is where ionization of neutrals by electrons is most likely, the time required for electrons to reach the 100 volt potential is of interest.

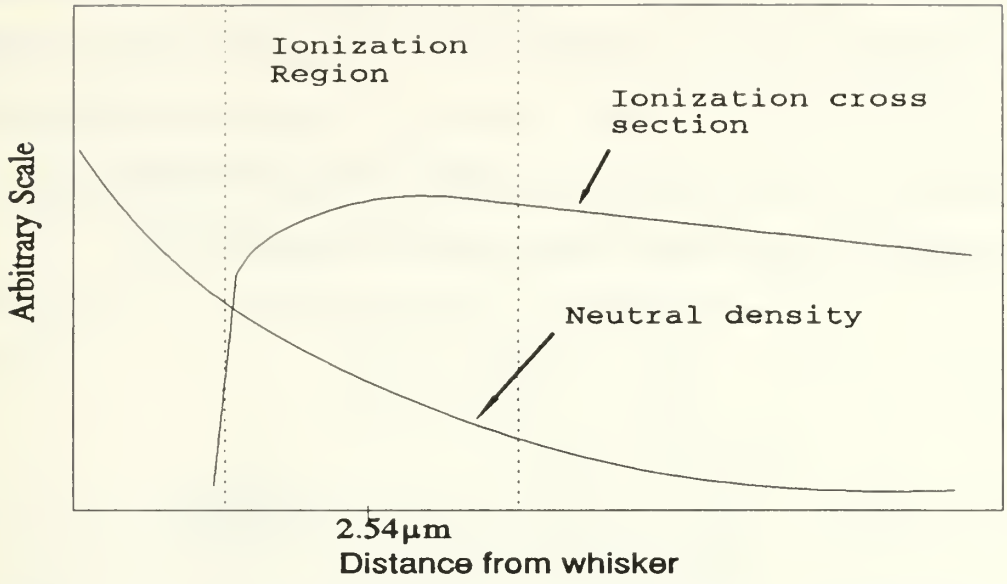

Figure 3.2. Schematic figure of typical ionization cross section and neutral density distribution at a time shortly after the voltage is applied.

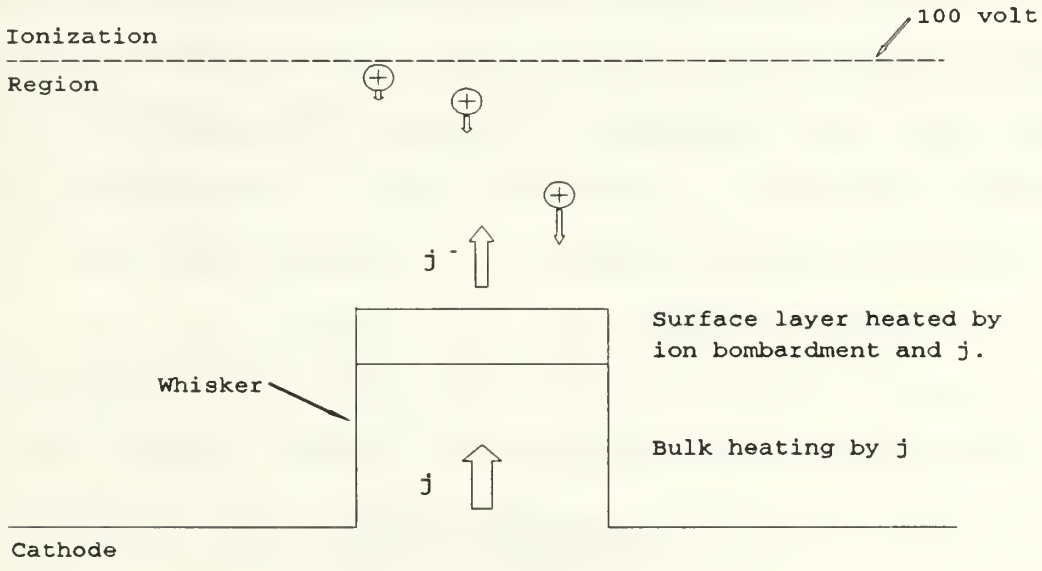

Figure 3.3. Basic setup of the model.

Because of their larger mass, the ions produced accelerate back toward the cathode at a much slower rate. Since there cannot be significant ionization of desorbed neutrals until they arrive at the 100 volt potential, the time required for the neutrals to reach that distance is also of interest. For a 1 MV applied potential, the times of interest are

$$\begin{aligned} \Delta t^{-} &= 8.6 \times 10^{-13} \text{ sec} \\ \Delta t^{+} &= 1.5 \times 10^{-10} \text{ sec} \\ \Delta t^{\circ} &= 7.7 \times 10^{-9} \text{ sec} \end{aligned} \qquad (3.1)$$

where Δt^{-} is the time of flight for an electron initially at rest to travel 2.54 μm in a constant electric field of $E=3.9 \times 10^{7}$ V/m , Δt^{+} is the time of flight for an oxygen ion initially at rest to travel 2.54 μm in the same electric field, and Δt° is the time for a neutral atom to travel 2.54 μm at the speed of sound (approximately 330 m/s). Note that if the constant electric field of this model were allowed to vary on a nanosecond time scale, the electrons and ions would experience a relatively "quasi steady state" electric field.

2. OHMIC HEATING

The power dissipated per unit volume in the surface layer of the whisker due to ohmic heating is given by

$$\frac{OHMIC\ POWER}{VOLUME} = \frac{j^2 \rho\ A\ L}{A\ L} = j^2 \rho \qquad (3.2)$$

where A is the surface area of the whisker, ρ is the resistivity of the whisker material, L is the depth of the surface layer, and j is the current density flowing through the whisker.

3. ION SURFACE HEATING

The power dissipated per unit volume in the surface layer due to ion bombardment is given by

$$\frac{ION\ POWER}{VOLUME} = \frac{(j^{+}\ A)\ 100\frac{eV}{ion}\frac{1.6x10^{-19}J}{eV}}{(A\ L)\ 1.6x10^{-19}\frac{C}{ion}} = \frac{100j^{+}}{L} \qquad (3.3)$$

where j^{+} is the ion return current density, L is the depth of the surface layer in which the ions deposit all of their energy, and A is the surface area of the whisker. This model assumes each ion is singly ionized and falls from the 100 volt equipotential surface thus delivering 100 eV of energy to the whisker. Recombination energy is relatively small and thus will be neglected.

4. ION CURRENT DENSITY VS. ELECTRON CURRENT DENSITY

Let $\lambda=1/n_o\sigma_o$ be the mean free path of electrons in a neutral cloud of density n_o and ionization cross section σ_o. Then for a neutral cloud of thickness d, λ/d electrons will produce one ion. The ratio of current densities is given by

$$\frac{j^+}{j^-} = \frac{\frac{e}{\text{area } \Delta t^-}}{\frac{e\lambda/d}{\text{area } \Delta t^-}} = \frac{d}{\lambda} \qquad (3.4)$$

where j^- is the current density of electrons emitted from the surface of the whisker and Δt^- is the time of flight for an electron at rest on the surface of the whisker to travel to the ionization region (see Figure 3.4). Thus

$$j^+ = \frac{d}{\lambda} j^- = d\, n_o \sigma_o\, j^- . \qquad (3.5)$$

5. TOTAL CURRENT DENSITY INSIDE WHISKER

For every ion that falls back to the surface of the whisker there is an image electron that travels within the whisker to meet and recombine with the ion. Therefore the total current density inside the whisker is

$$j = j^- + j^+ . \qquad (3.6)$$

In terms of the emitted electron current density

$$j = j^- + \frac{d}{\lambda} j^- = j^-(1 + d n_o \sigma_o) . \qquad (3.7)$$

6. RATIO OF OHMIC + ION HEATING TO OHMIC HEATING

Let R be the ratio of ohmic + ion heating to ohmic heating in the surface layer. Then from Equations 3.2 and 3.3,

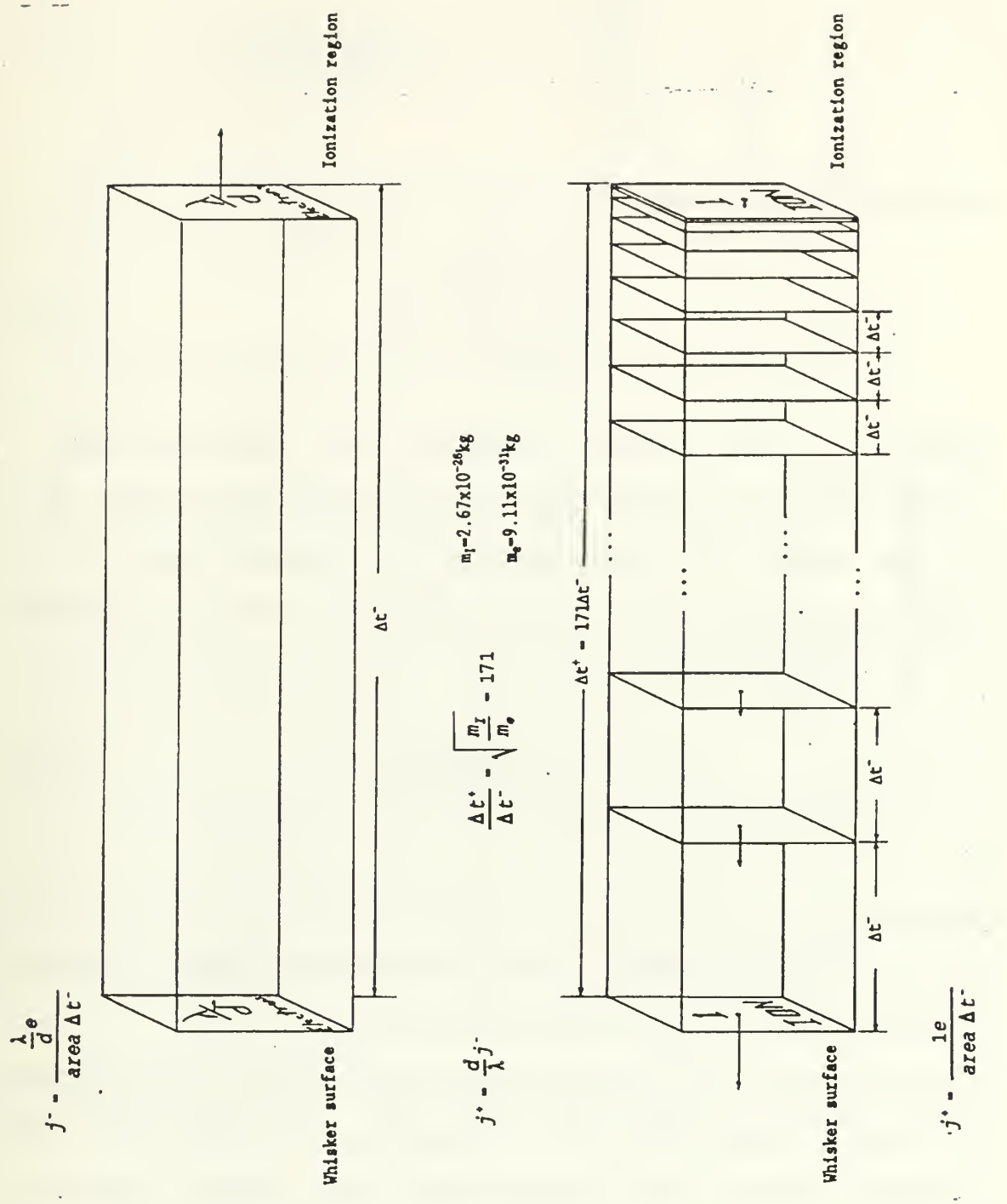

Figure 3.4. Graphic representation of the relationship between electron and ion (oxygen) current densities. The j^- is arbitrary. The rectangles indicate locations of accelerated charges at equal time increments.

$$R = 1 + \frac{\frac{100 j^+}{L}}{j^2 \rho} = 1 + \frac{100\, d\, n_o \sigma_o}{j^- L\, \rho (1 + d\, n_o \sigma_o)^2} \quad . \tag{3.8}$$

Inserting the values

$$\begin{aligned} d &= 1x10^{-6}\ m \\ \sigma_o &= 1x10^{-20}\ m^2 \\ \rho &= 7x10^{-8}\ \Omega\text{-}m \\ L &= a_o k \end{aligned} \tag{3.9}$$

where a_o is the lattice parameter for stainless steel ($2.9x10^{-10}$ m), ρ is the resistivity for stainless steel, and k is the number of monolayers in the surface layer of the whisker through which the ions penetrate, the ratio becomes

$$R = 1 + \frac{5x10^{-8} n_o}{(1 + 10^{-26} n_o)^2 j^- k} \quad . \tag{3.10}$$

This ratio, R, is plotted in Figures 3.5 and 3.6 as a function of j^-, n_o, and k. These figures demonstrate that the heating of the surface of the whisker due to return ion current is far more efficient than the heating of the whisker bulk due to ohmic heating. For example, if the Child-Langmuir current density of $j_{CL}=3.6x10^6\ Am^{-2}$ were passed through a neutral density of $n_o=10^{25}\ m^{-3}$ and the return ions penetrated only one monolayer into the whisker surface, the ratio of total heating to ohmic heating in that monolayer would be

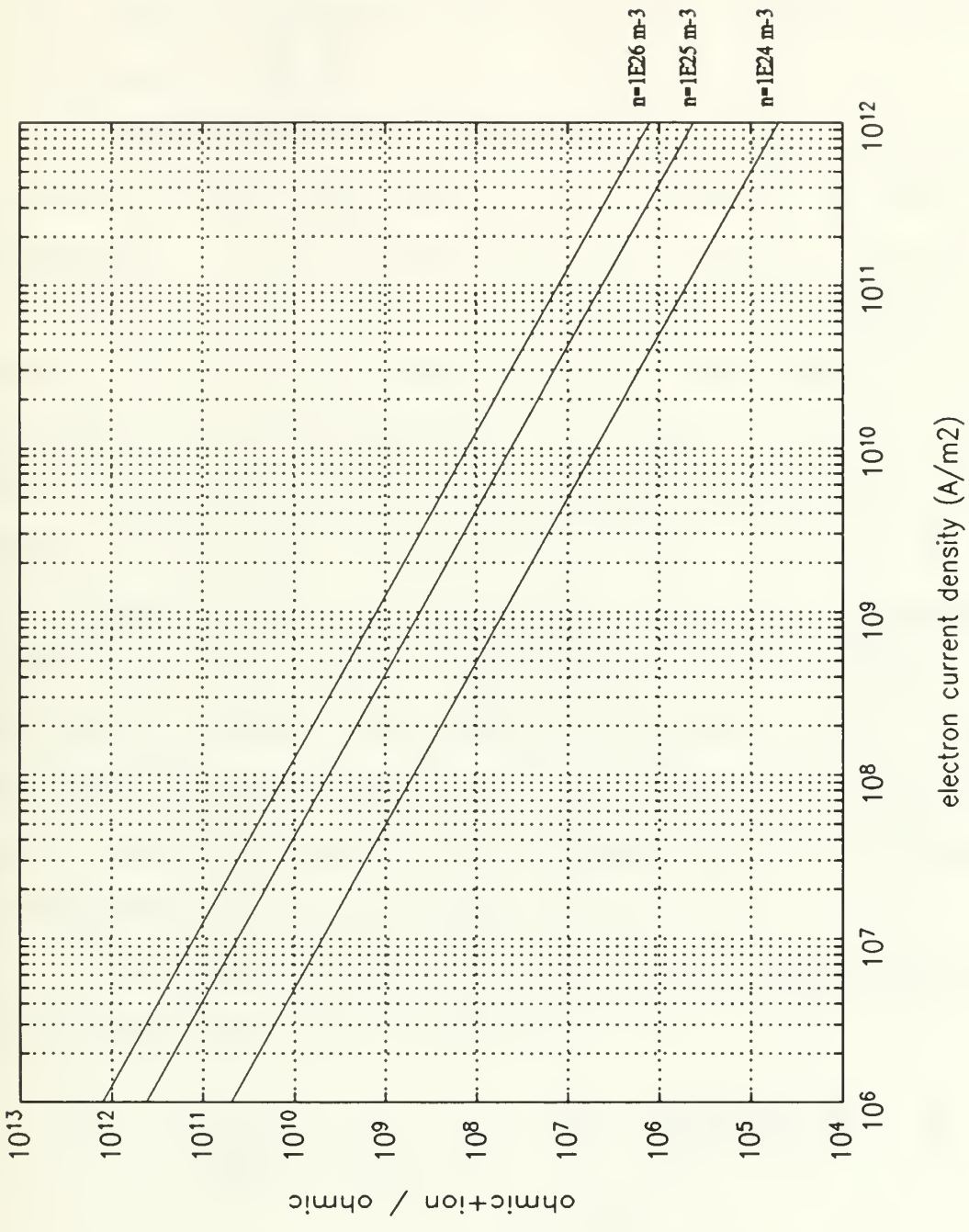

Figure 3.5. Ratio of ohmic + ion heating to ohmic heating vs. electron current density. The solid lines are plots of Equation 3.10 for k=1 and various neutral densities (n).

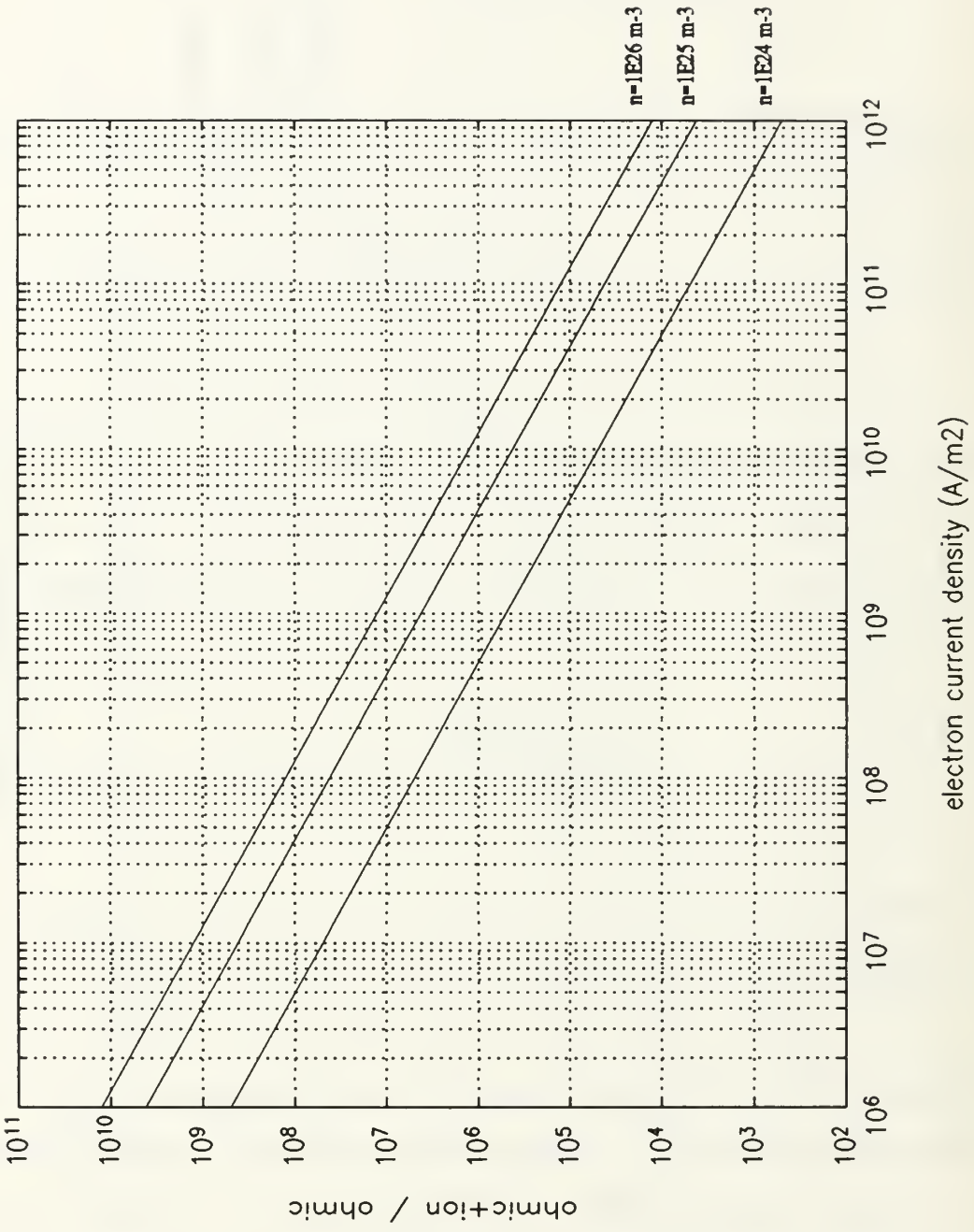

Figure 3.6 Ratio of ohmic + ion heating to ohmic heating vs. electron current density. The solid lines are plots of Equation 3.10 for k=100 and various neutral densities (n).

$R=10^{11}$. It is important to note that the return ions deposit their energy into a highly localized volume.

7. ENERGY DEPOSITION PER ATOM IN THE SURFACE LAYER (IN eV)

To determine the current density required to explode a whisker in the new model, it is necessary to make two assumptions. First assume that the energy required to liberate an atom from the surface of the cathode is approximately 5 eV (the binding energy). Then assume that, on average, the energy deposited by return ions is evenly distributed throughout the volume of the surface layer. Thus, if each of the atoms in the surface layer is given 5 eV in a short period of time, the layer will "explode." With these assumptions, a simple calculation will provide the relationship between field emitted electron current density and energy deposited per surface atom (eV/atom). The current density required to explode the whisker is that which leads to a deposition of 5 eV per atom.

The energy per atom deposited in the surface layer of the whisker due to ohmic heating is

$$\frac{Energy}{Atom}(ohmic) = \frac{(j^2\,\rho)\,\Delta t \dfrac{1eV}{1.6x10\text{-}19J}}{\rho_m} \qquad (3.11)$$

where ρ_m is the number density of the whisker material and Δt is the duration of the current flow in seconds.

The total energy per atom deposited in the surface layer of the whisker due to both ohmic and ion heating is

$$\frac{Energy}{atom}(total) = R \times \frac{Energy}{atom}(ohmic) \ . \qquad (3.12)$$

Using $\rho_m = 8.2 \times 10^{28}$ atoms/m^3 for steel and expressing the total current density in terms of the field emitted electron current density, Equations 3.4, 3.11, and 3.12 give

$$\frac{Energy(eV)}{atom}(total) = R \times 5 \times 10^{-18} \ (j^-)^2 (1 + 10^{-26} n_o)^2 \Delta t. \qquad (3.13)$$

Values of eV/atom are plotted in Figures 3.7 and 3.8 as a function of j^-, n_o, and for $\Delta t = 10^{-9}$ sec. Figure 3.7 shows that the field emitted current density required to explode a one monolayer surface of the whisker within a nanosecond is still greater than the Child-Langmuir limit discussed earlier ($j_{CL} = 3.6 \times 10^6$ A/m^2). Figure 3.8 shows that to explode a 100 monolayer thick section of the whisker surface requires an even higher current density.

These figures indicate that a sufficient field emitted current density to explode the whisker still can not be achieved. Whisker explosion is therefore not the primary

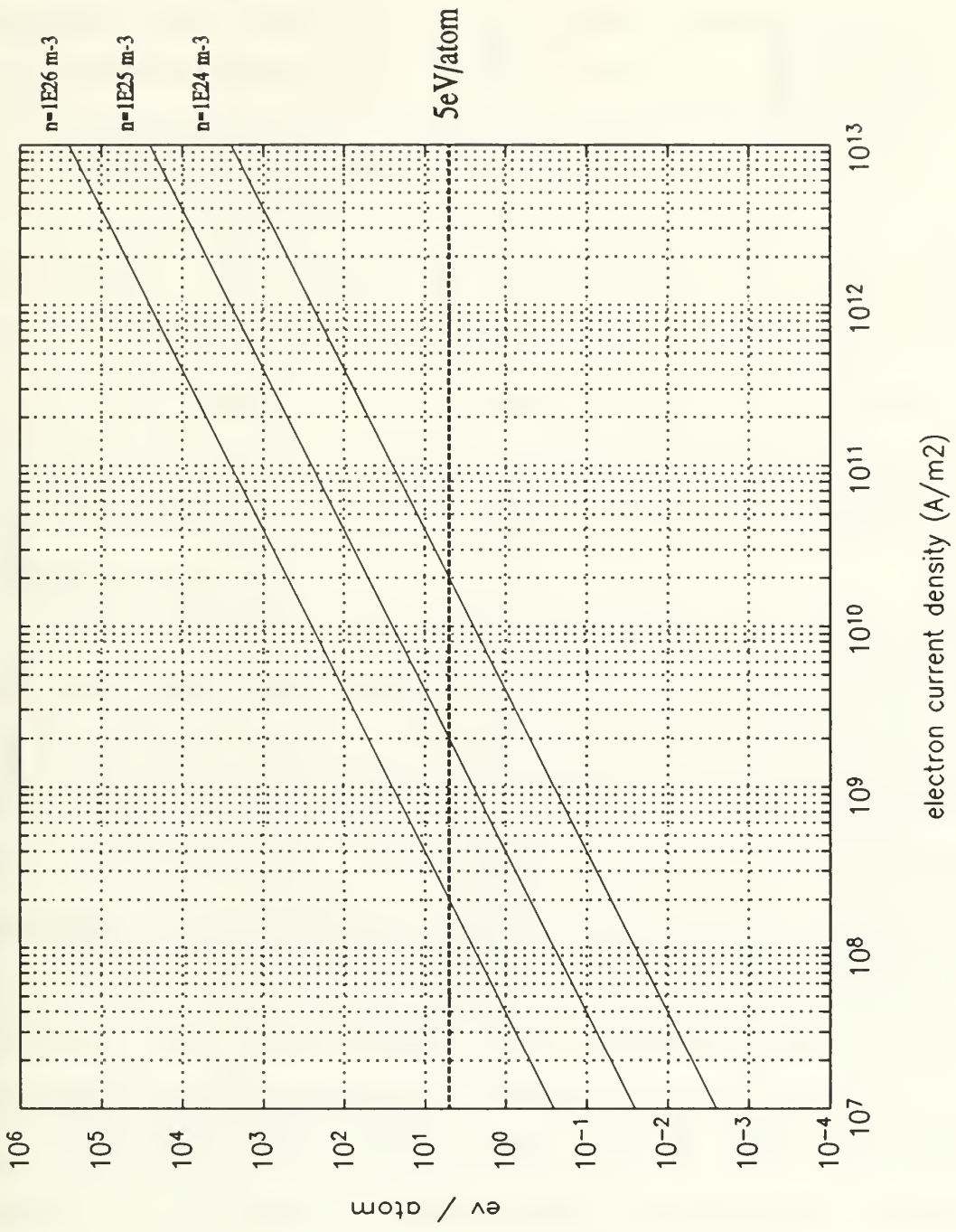

Figure 3.7. Electron volts per surface atom vs. electron current density. The solid lines are plots of Equation 3.13 for k=1, $\Delta t=10^{-9}$ sec, and various neutral densities (n). The dashed line is 5 eV/atom.

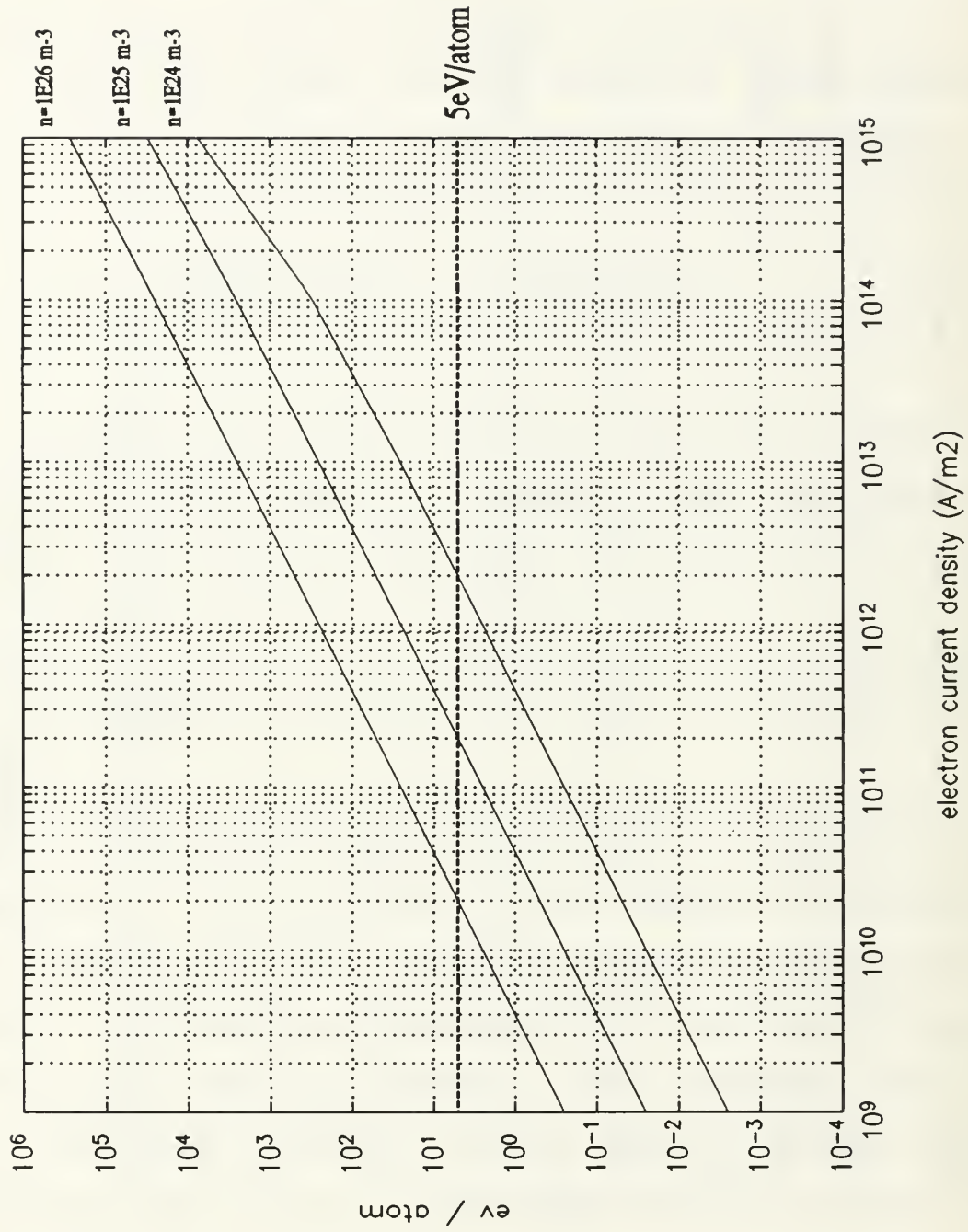

Figure 3.8 Electron volts per surface atom vs. current density. The solid lines are plots of Equation 3.13 for k=100, $\Delta t=10^{-9}$ sec, and various neutral densities (n). The dashed line is 5 eV/atom.

mechanism for the onset of plasma formation. The new model proposes that ionization of a dense region of desorbed neutrals is the mechanism of the onset of plasma formation.

E. DEVELOPMENT OF PROCESS AFTER ONSET

The new model assumes "quasi" steady state conditions. This is not a bad assumption based on the fact that electron and ion transport times are relatively negligible as compared to the time required for the neutral density to change. The neutral density will change on the nanosecond time scale and thus the entire plasma formation process should change on the nanosecond time scale.

The scenario for the development of the dynamic process from the steady state model will now be discussed. The return ion bombardment leads to further desorption of neutrals thus increasing the neutral density. The increased neutral density will reduce the mean free path for ionization of neutrals by electrons thus increasing the ionization rate. As more ions are produced, the positive space charge presence enhances the electric field and through the Fowler-Nordheim relation strongly enhances the field emitted electron current. Also due to the enhanced electric field, the 100 volt equipotential surface moves closer to the cathode surface into a region of higher neutral density. This effect also increases the ionization rate. The whole process rapidly becomes unstable and leads to dense plasma formation and finally the formation

of a unipolar arc [Ref. 7]. The unipolar arc model allows current densities in excess of the Child-Langmuir limit to flow from the metal surface, into the plasma, and back to same surface. The unipolar arc current density in combination with the ion bombardment would most likely be sufficient to explode the whisker. For a more detailed discussion of the unipolar arc model refer to Schwirzke [Ref. 9].

F. PREDICTIONS OF NEW MODEL

1. Time Delay of Onset of Plasma Formation

The ionization of the desorbed neutrals does not become significant until the neutrals reach the 100 volt equipotential surface. Therefore, the onset of plasma formation should be delayed from the onset of desorption by the time of flight of the neutrals to the 100 volt equipotential surface, $\Delta t^{o}=7.7 \times 10^{-9}$ sec.

2. Prediction of Onset of Plasma Formation in a Transient Diode

For a diode which experiences a "quasi" steady voltage which varies on the nanosecond time scale, the model will still be valid. As the voltage is applied across the diode, the 100 volt equipotential surface moves from the anode side of the diode toward the cathode. The desorbed neutrals expand from the cathode surface toward the anode. The onset of plasma formation will not occur until the 100 volt equipotential surface and the desorbed neutral density reach

the same position. For a given time varying voltage waveform and diode gap, the time delay of the onset of plasma formation can be predicted using the following procedure:

a. Step 1

For the voltage waveform compute the position of the 100 volt equipotential surface away from the cathode as a function of time.

b. Step 2

Compute the positions of desorbed neutrals which were released at the onset of the voltage pulse as a function of time.

c. Step 3

Plot both of these functions on the same time axis.

d. Step 4

The intersection of the two functions occurs at the predicted onset time.

This procedure is used to generate plots such as Figure 5.40 predicting the onset of plasma formation.

IV. EXPERIMENT

A. OVERVIEW OF THE EXPERIMENT

The purpose of this experiment is to determine the voltage across the diode at which plasma formation begins so that a comparison can be made to the model discussed in Chapter III. The time delay from the onset of the voltage pulse to the onset of plasma formation can also be measured during the experiment and compared to the model. Aside from the quantitative data taken in the experiment, time lapsed photographs are taken to display some qualitative information about the diode plasma.

The diode used in the experiment is the fast pulsed vacuum diode of the Naval Postgraduate School (NPS) Flash X-Ray (FXR) Facility (see Appendix A). The basic layout of the FXR facility is shown in Figure 4.1 [Ref. 10]. The voltage and current across the diode are measured with the pre-installed voltage and current monitors supplied with the FXR generator. The plasma is observed through the viewing window of the FXR generator using an avalanche photodiode sensitive to visible light. (For description of the sensors used in this experiment, see Appendix B). The primary source of light from the FXR diode is emission from de-excitation and recombination within the plasma [Ref.2]. Time resolved data from the

voltage, current, and photodiode sensors are monitored simultaneously on three 1 GHz bandwidth, Tektronix oscilloscopes. The current through the diode is measured so that the voltage and current relationships in the actual diode can be compared to the theory discussed in Chapter II.

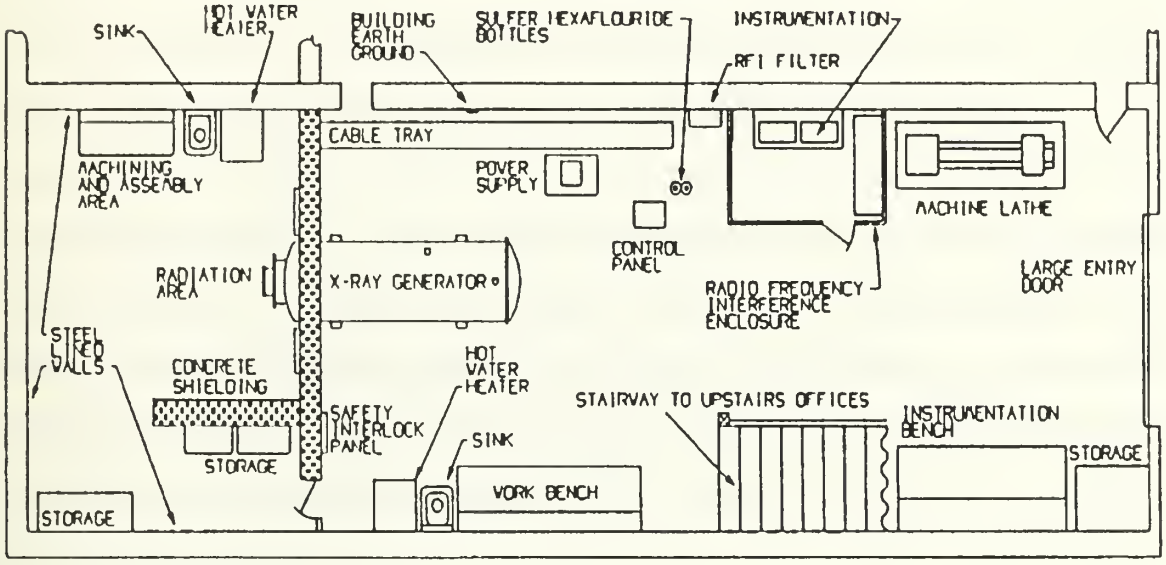

Figure 4.1 Basic layout of the NPS FXR Facility.

B. DISCUSSION OF PROBLEMS ENCOUNTERED

1. Electromagnetic noise

The processes involved in operating the FXR machine generate a wide spectrum of electromagnetic noise [Ref. 10]. The noise is present on both the pulse

forming end and the diode end of the FXR generator. The oscilloscopes and other sensitive electronic equipment which are located near the pulse forming end of the machine are shielded by a radio frequency interference (RFI) enclosure. This enclosure and instruments are grounded to the same earth ground potential as the FXR generator. This shielding method was very successful in reducing electromagnetic noise at the pulse forming end of the FXR generator.

The electromagnetic noise at the diode end of the machine was more difficult to reduce since it was not practical to build a shielded enclosure on the diode end of the FXR generator. The electromagnetic noise was not a major problem for the diode voltage and diode current sensors since those signals were typically in the tens to hundreds of volt ranges. The photodiode signal was typically in the tens of millivolts range and would be masked by the noise. The solution to this problem was to move the photodiode as far away from the diode end of the FXR machine as was practical. This was done by using a fiber optic bundle to transport the light from the window to the photodiode approximately 2 meters away. This arrangement also made it practical to use an RFI enclosure around the photodiode setup. In addition to the RFI enclosure, the coaxial signal cable between the photodiode and the oscilloscope had to be shielded with aluminum foil near the diode end of the FXR machine. Using this arrangement reduced the electromagnetic noise to a manageable level of

between 5 and 10 millivolts with a photodiode signal of greater than 30 millivolts.

2. X-ray Emission

The x-rays generated by the FXR generator were found to produce a considerable signal in the photodiode circuit. This x-ray signal was not of interest to this experiment and tended to obscure the desired photodiode signal. Fortunately, the solution to this problem was the same as the solution to the electromagnetic noise problem. Placement of the photodiode 2 meters away from and perpendicular to the diode end of the FXR generator greatly reduced the magnitude of the x-ray signal. Lead shielding was also placed around the photodiode RFI enclosure to reduce the x-ray dose even further. Ultimately, the x-ray signal was not detectable above the electromagnetic noise.

3. Timing

To reach the goal of the experiment, it was necessary to resolve the diode voltage, diode current, and photodiode signals as precisely as possible in time. The diode voltage and diode current pulses have rise times of between 5 and 10 nanoseconds and the photodiode signal has a rise time of 1 to 2 nanoseconds. When working with such pulses, the difference in time it takes electrical signals to travel the various lengths of coaxial cables and trigger various oscilloscopes is quite significant and must be taken into

account. The method used to synchronize the oscilloscope traces in time is described in detail in Appendix C. In addition to the electrical signal delay due to cable length, there is also an optical delay in the photodiode signal due to the length of the lens system and fiber optic bundle. Unfortunately, the fiber optic bundle used in the experiment was of unknown origin and had no markings to indicate its index of refraction. Therefore, the time delay could not be determined with a simple calculation. The optical time delay had to be determined experimentally. The method used to determine the optical time delay is described in Appendix D.

C. SETUP

1. Optical

Two optical setups were used in this experiment. Setup 1 was used to take time lapsed photographs of the plasma formation. Setup 2 was used to time resolve the light emission from plasma formation.

a. Optical Setup 1

Optical Setup 1 used a Polaroid camera with type 667 (ISO 3000) film. The camera was focused on the center of the cathode-anode gap through the viewing window (see Figure 4.2). Neutral density filters were used to limit the intensity of visible light reaching the camera. The transmittance of these filters ranged from 1% to 10%. The camera shutter was opened prior to the shot and closed after

the shot. The room lights were turned out while the shutter was open to avoid exposing the film to sources of light other than the plasma light.

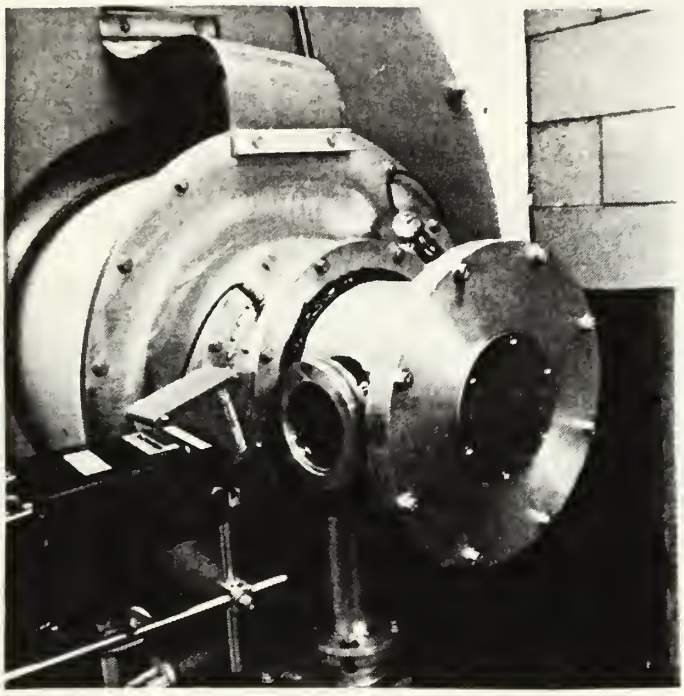

Figure 4.2 Photograph of optical setup 1. Notice the viewing window and camera.

b. Optical Setup 2

Optical Setup 2 used the Opto-Electronics Inc. series PD-30 ultra high speed photodetector (see Appendix B for details). The photodetector was biased to approximately -130 volts with the Opto-Electronics model PS-30 power supply. The setup also used a 3 meter long, 5 millimeter diameter non-coherent fiber optic bundle and a three lens focusing system.

The lens system was used to gather light through the window on the diode end of the FXR machine and transport that light, via the fiber optic bundle, to the photodiode. The lens system consisted of a +20 centimeter focal length lens placed 20 centimeters from the center of the anode-cathode gap. Two shorter focal length lenses were used to focus the light into the fiber optic cable (see Figures 4.3 and 4.4). The photodiode end of the bundle was placed adjacent to the aperture of the photodiode. The center of the bundle was aligned with the active area of the photodiode. This setup provided the ability to focus on a small region inside the anode-cathode gap. The region of focus was the cathode surface for all of the shots using this setup.

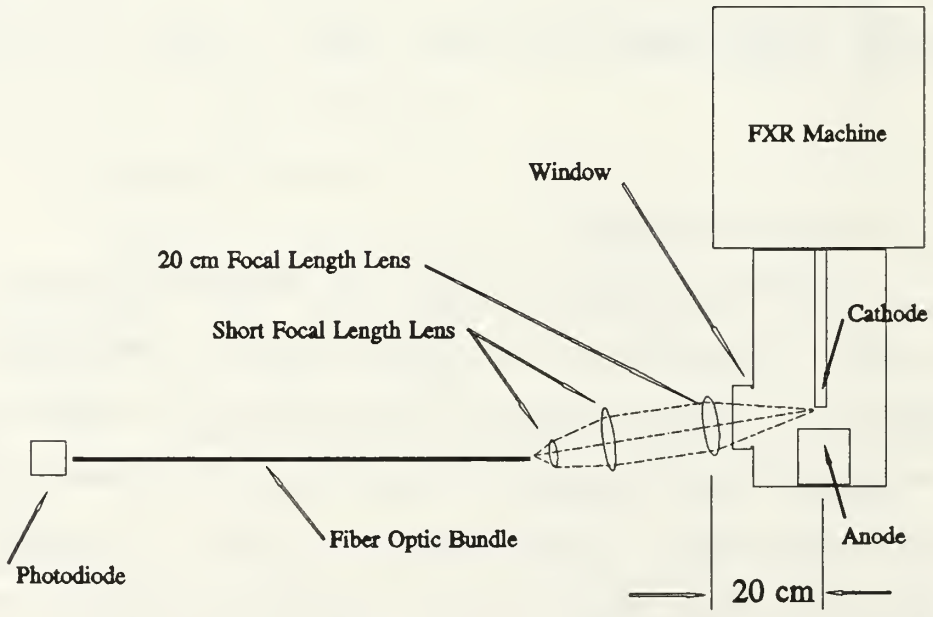

Figure 4.3 Schematic diagram of optical setup 2.

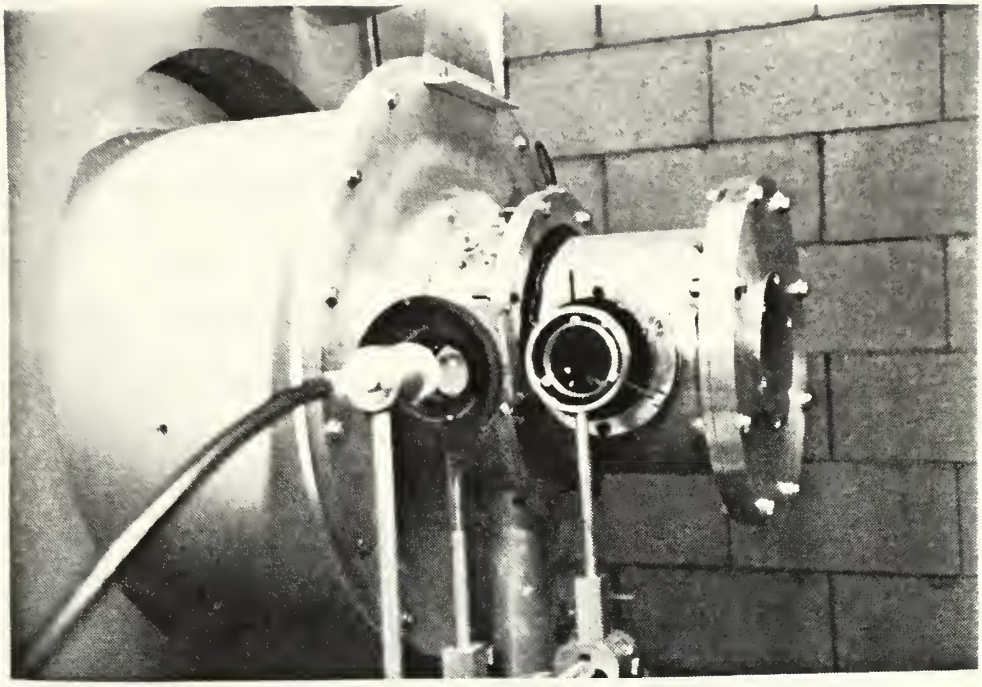

Figure 4.4 Photograph of optical setup 2. Notice lens system and fiber optic bundle.

2. Electronic

To synchronize in time the signals from the diode voltage, diode current, and photodiode detectors, the three oscilloscopes had to be externally triggered prior to the arrival of the signals. This was done by using the Marx voltage signal to trigger a Stanford Research DG-535 multi channel digital delay generator which in turn was used to trigger the oscilloscopes. The Marx voltage was the appropriate choice for a trigger signal because it significantly precedes the arrival of the voltage pulse at the

diode. Also, the Marx voltage detector is located much closer to the RFI instrument room than the diode-end instruments (diode voltage monitor, diode current monitor, and photodiode) and thus uses a much shorter signal cable. This allows the trigger pulse to the DG-535 delay generator to precede the diode-end instrument signals' arrival at the oscilloscopes. Table 4.1 lists the sensors and oscilloscopes used. Figure 4.5 shows the electronic setup for the experiment.

Table 4.1 ELECTRONIC EQUIPMENT USED.

SIGNAL MEASURED	DETECTOR	OSCILLOSCOPE
Diode Voltage (46 dB attenuation at scope input)	PIM-197A-25, Voltage Divider, serial# 8400	Tektronix 7104, 7B92A time base, 7A29 amplifier
Diode Current (20 dB attenuation at scope input)	PIM-199B, Fluxmeter, serial# 8402	Tektronix HB7912, 7B90P time base, 7A16P amplifier
Photodiode	PD-30-03, Avalanche type, serial# 4016	Tektronix 7104, 7B92A time base, 7A29 amplifier

D. PROCEDURE

Procedure 1 is performed to obtain time lapsed photographs of the diode plasma. Procedure 2 is performed to obtain the voltage and time delay associated with plasma formation. In both procedures the diode gap spacing is 2.54 cm and the vacuum chamber is evacuated to 2×10^{-5} Torr as read on the ion

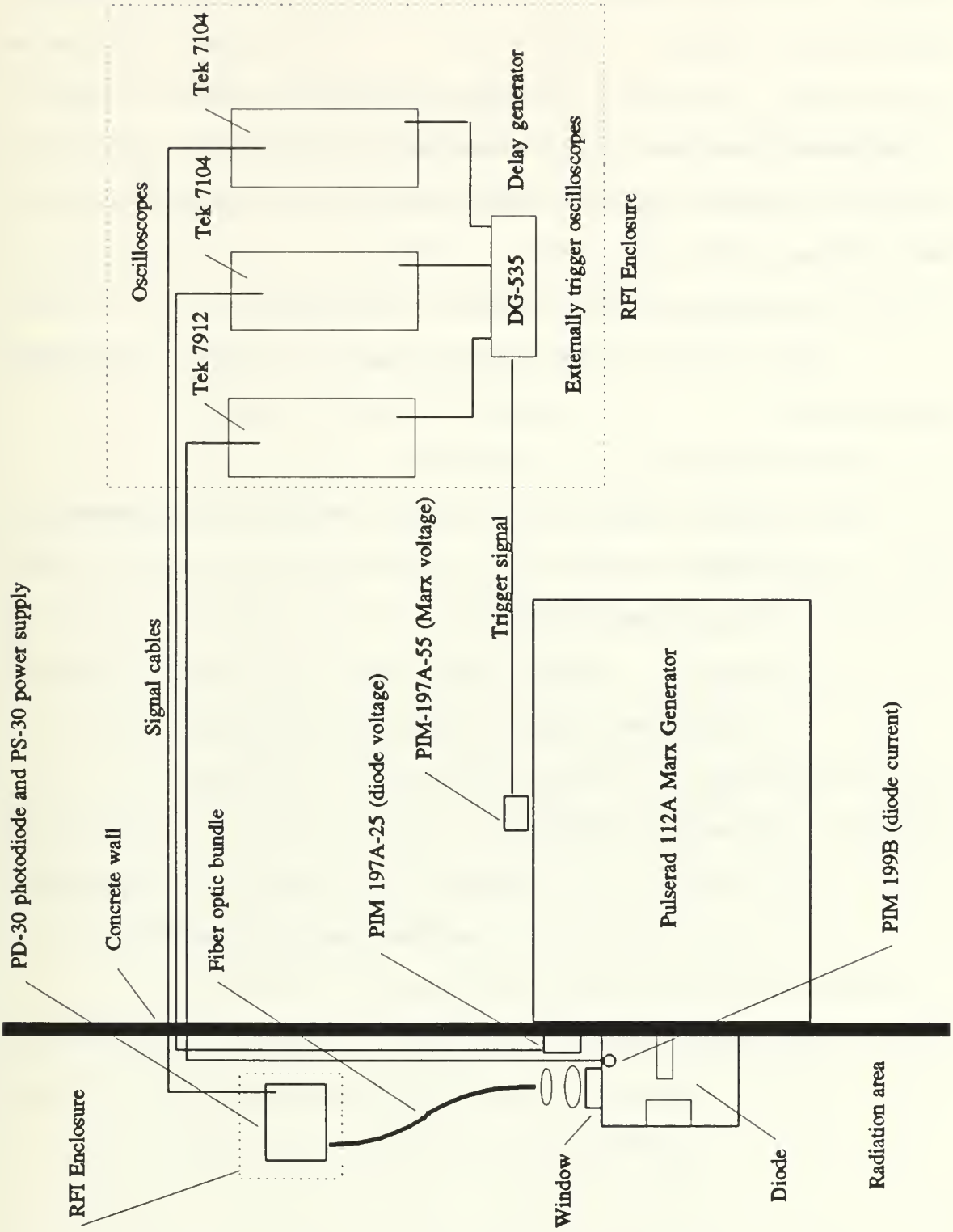

Figure 4.5 Schematic drawing of experimental setup.

gauge. The FXR machine is operated in accordance with the operating manual [Ref. 11]. In the following procedures, the term "fire FXR machine" will refer to the act of discharging the voltage pulse through the diode. Note that these procedures use the same cathode and anode surfaces for all of the shots.

1. Procedure 1: Time Lapsed Photography

The following procedure is used to obtain time lapsed photographs.

a. Step 1

Setup camera in accordance with optical setup.

b. Step 2

Open camera shutter.

c. Step 3

Charge Marx bank to 55 kV.

d. Step 4

Fire FXR machine.

e. Step 5

Close camera shutter and remove exposed picture.

The above procedure is repeated several times each for 55 kV, 75 kV, and 100 kV Marx bank charges.

2. Procedure 2: Time Resolved Plasma Formation

a. Setup

Install optical setup 2.

b. Energize all instruments and set sensitivities

Allow all of the electronic equipment to warm up for approximately 30 minutes. Adjust the sweep speeds and vertical sensitivities on the oscilloscopes to the desired settings. Set PD-30 bias to -130 volts.

c. Perform timing procedure

The timing procedure of Appendix C must be performed each time the sweep speed on an oscilloscope or a delay on the delay generator is changed. Generally, this procedure is done directly before or directly after taking a series of shots at a given Marx charge.

d. Record Parameters

Record all relevant parameters in lab notebook. As a minimum, the vacuum reading, diode gap separation, and Marx charging voltage must be recorded.

e. Data run procedure

(1) Step 1. Charge Marx bank to desired voltage.

(2) Step 2. Open the shutters on the three oscilloscope cameras.

(3) Step 3. Fire the FXR machine.

(4) Step 4. Close shutters on cameras and remove exposed film.

(5) Step 5. For one shot per data run, cover the aperture of the fiber optic bundle with a black piece of paper. This will provide a reference "dark" signal. This is necessary to determine how the electromagnetically, hostile environment near the diode end of the FXR machine affects the photodiode circuit.

(6) Step 6. Repeat steps 1 through 4 approximately 10 times for a given Marx voltage.

f. Repeat procedure.

Perform parts c through e above for 55 kV, 75 kV, and 100 kV Marx bank charges.

E. NOMENCLATURE

For ease of notation, all future reference to shots of the Flash X-ray machine will be classified by their Marx Bank charge. Table 4.2 lists the Marx Bank charges and typical peak diode voltages and peak diode currents observed during the experiment.

Table 4.2 TYPICAL OPERATING PARAMETERS CLASSIFIED BY MARX BANK CHARGE.

Marx Bank Charge (kV)	Typical Peak Diode Voltage (MV)	Typical Peak Diode Current (kA)
55	0.6	4.1
75	1.2	12.2
100	1.8	18.0

V. EXPERIMENTAL RESULTS

A. TIME LAPSED PHOTOGRAPHS

The time lapsed photographs taken using procedure 1 must be interpreted with caution. The camera shutter is open for the entire plasma evolution. The light gathered through the window was so intense that neutral density filters were necessary to prevent overexposure of the film. Enough filters were installed so that only the most intense light reached the film. The luminosity is an indication of the plasma density so that the most intense light should come from the most dense plasma regions. Figure 5.1 shows the long time scale photodiode signal for a 75 kV shot and indicates that the most intense light occurs at the beginning of the diode discharge.

Figure 5.2 is a photograph of a 75 kV shot (typically 1.2 Megavolts peak diode voltage) using a 10% transmittance filter. Figure 5.2 clearly demonstrates the non-uniformity of the plasma evolution. Very intense spots are shown on the cathode surface and extremities. These spots are called "cathode spots" in the literature. The areas around these spots show a spherically fading intensity which must correspond to the plasma expansion away from the cathode spots. This expanding plasma region will be referred to in this report as a cathode flare.

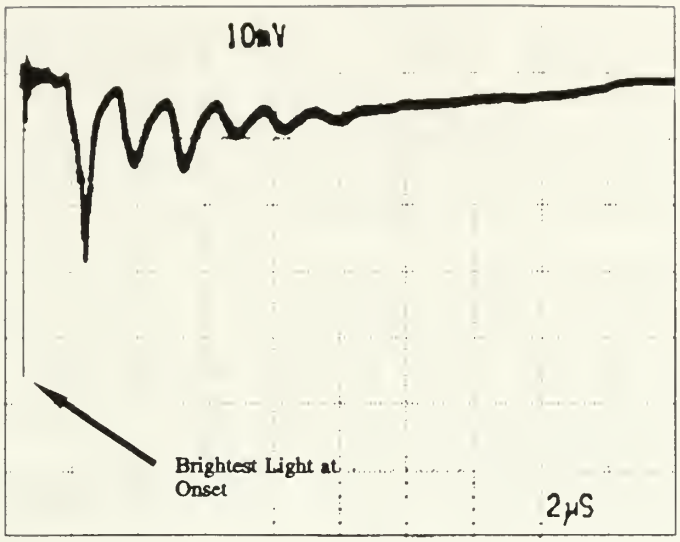

Figure 5.1 Scanned, computer enhanced, photograph of the long time (2 μs/div) photodiode waveform for a 75 kV shot. The brightest light occurs at onset. Later peaks correlate to ringing of the diode voltage and current waveforms.

Figure 5.2 Time lapsed photograph of a 75 kV shot using a 10% transmittance neutral density filter. Notice intense spots on cathode surface (cathode spots).

Figure 5.3 is a photograph of a 75 kV shot using a 2.5% transmittance filter. This figure demonstrates that anode flares also occur. Any cathode flares that may have occurred in this shot were not bright enough to be seen through the darker filter.

Figure 5.4 is a photograph of a 75 kV shot using a 1% transmittance filter. This figure demonstrates that in some shots, both cathode and anode flares are of nearly equal luminosity. The bright region near the center of the gap indicates the collision of the cathode and anode plasmas. The fact that the plasmas collided near the center of the gap suggests that they were both formed at nearly the same time.

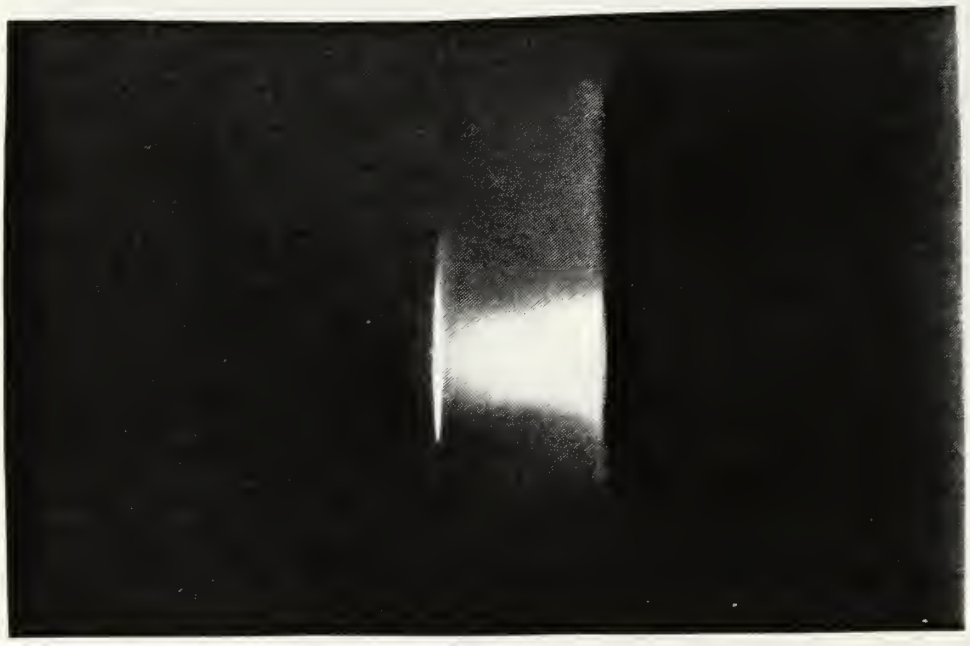

Figure 5.3 Time lapsed photograph of a 75 kV shot using a 2.5% neutral density filter. Notice the anode flare.

Figure 5.5 is a photograph taken for the exact same conditions as in Figure 5.4. Figure 5.5 is included here to emphasize how the long term plasma evolution varies from shot to shot. The variations are likely related to the idea that the plasma formation begins at randomly oriented microscopic sites. Each time the FXR is fired, the violent plasma formation changes the surface, by cratering, such that the next shot begins with a different surface. The only common thread between all of the plasma photographs taken in this experiment is that the brightest plasma regions appear to emanate from the surfaces where the cratering occurs. The only bright regions between the surfaces occur where two expanding plasmas appear to have collided.

Figures 5.6 and 5.7 are photographs taken of 55 kV shots (typically 0.6 Megavolts peak diode voltage) using a 2.5% transmittance filter. Figure 5.8 is a photograph of a 100 kV shot (typically 1.8 Megavolts peak diode voltage) using a 2.5% transmittance filter. These photographs indicate that there is not a significant difference in the character of the plasma evolution between the different voltage shots.

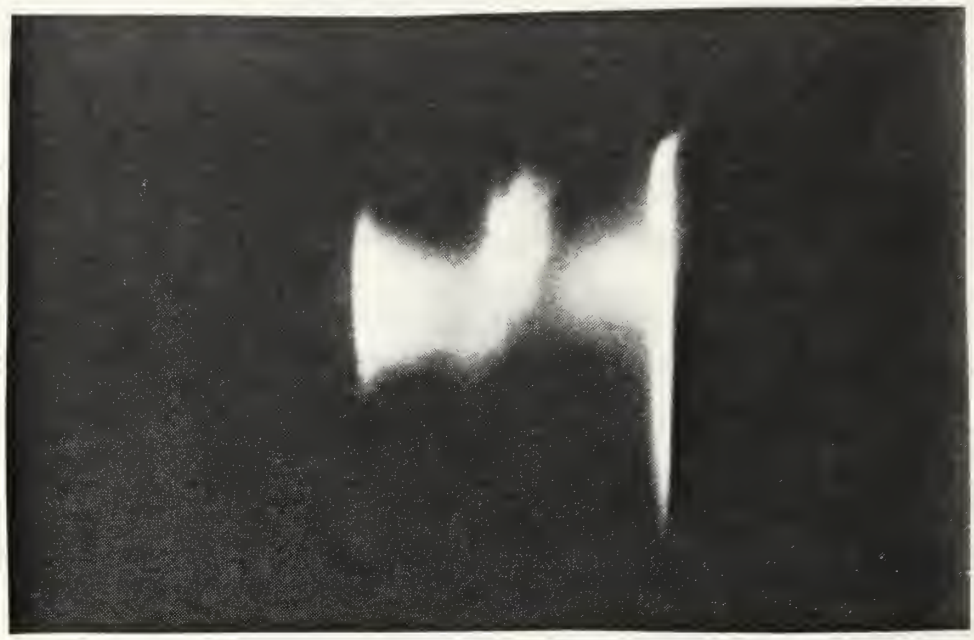

Figure 5.4 Time lapsed photograph of a 75 kV shot using a 1% neutral density filter. Notice interaction of anode and cathode plasmas.

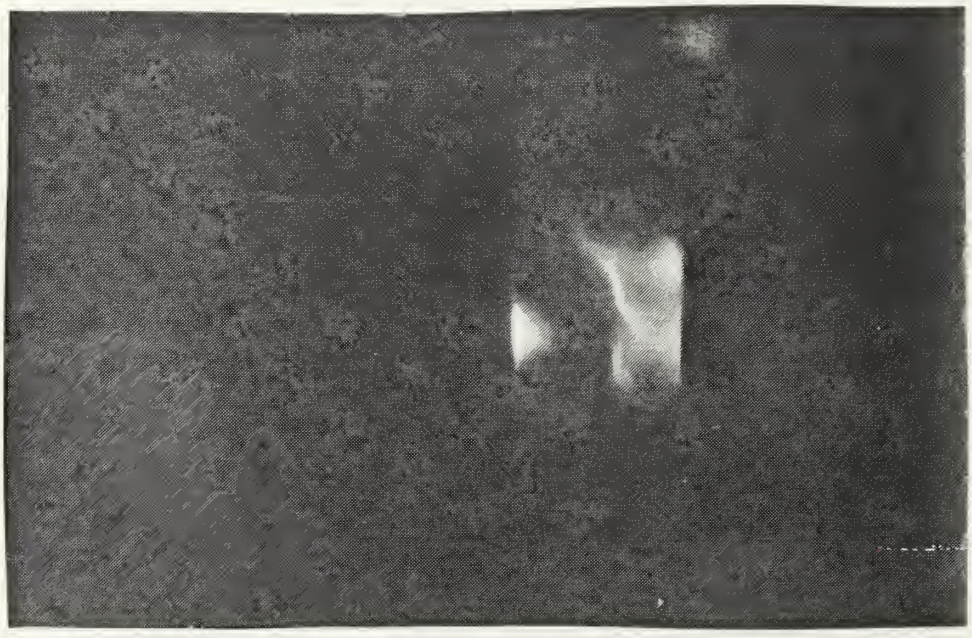

Figure 5.5 Time lapsed photograph of a 75 kV shot using a 1% neutral density filter. Notice interaction of anode and cathode plasmas.

Figure 5.6 Time lapsed photograph of a 55 kV shot using a 2.5% neutral density filter. Notice interaction of two cathode flares.

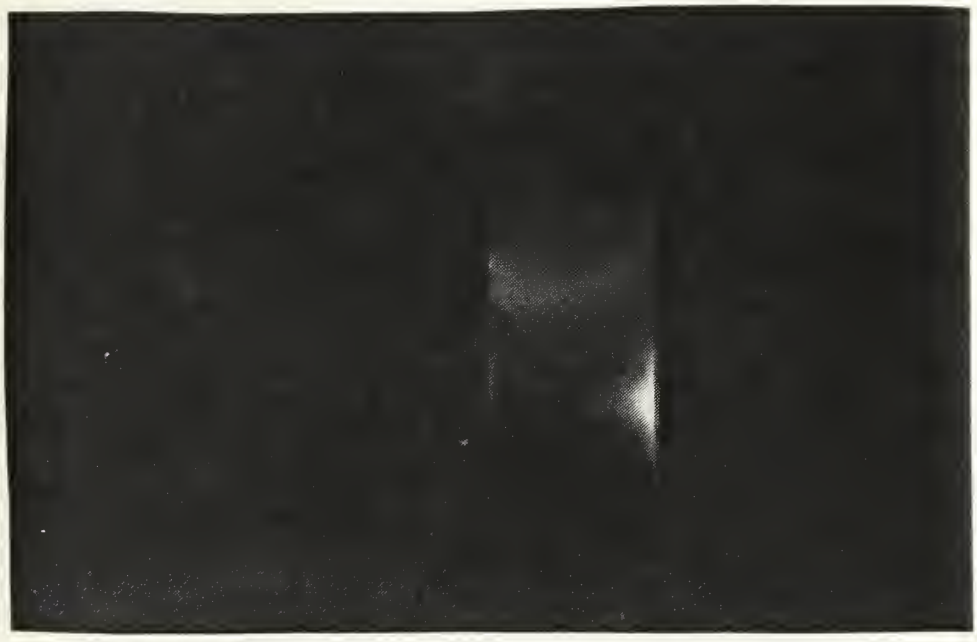

Figure 5.7 Time lapsed photograph of a 55 kV shot using a 2.5% neutral density filter. Notice both anode and cathode flares.

Figure 5.8 Time lapsed photograph of a 100 kV shot using a 2.5% neutral density filter. Notice multiple cathode spots.

B. TIME RESOLVED PLASMA FORMATION

1. Results of Error Analysis

An error analysis for this portion of the experiment has been performed in Appendix E. The results indicate that the timing of diode voltage and diode current waveforms have an accuracy of ± 1 nanoseconds and that the timing of optical signal waveforms have an accuracy of ± 2 nanoseconds. The magnitudes of diode voltage and diode current are measured with an accuracy of ± 12 %. The error analysis above is based on the oscilloscopes being calibrated to within specifications. The oscilloscopes were thought to have been

in calibration prior to the experiment. Comparison of the three oscilloscopes with a calibrated Tektronix model 2901 time mark generator after the experiment revealed that two of them had errors in the horizontal sweep speeds used. The time base errors have been determined (Appendix C) and correction factors have been noted in the figure captions of photographed oscilloscope traces.

2. Actual Data

Approximately 10 shots were fired in each data run. Three data runs were performed at different voltages (55 kV, 75 kV, and 100 kV). A representative data set from each run will be displayed below. Additionally, the reference ("dark") shot for each run will also be displayed. Note that the data from these oscilloscope traces can only be compared by applying both the Time Base Correction Factor (TBCF) and the Time Delay Correction (TDC) discussed in Appendix C. This is done by simply multiplying the raw data by the TBCF and then subtracting the TDC.

Figures 5.9 through 5.11 display the diode voltage, diode current, and photodiode waveforms, respectively, for a typical 55 kV shot. Figure 5.12 displays the "dark" photodiode signal from a similar 55 kV shot. The waveforms for the other shots in the run are similar to those displayed. Notice that the rise time of the diode voltage waveform is

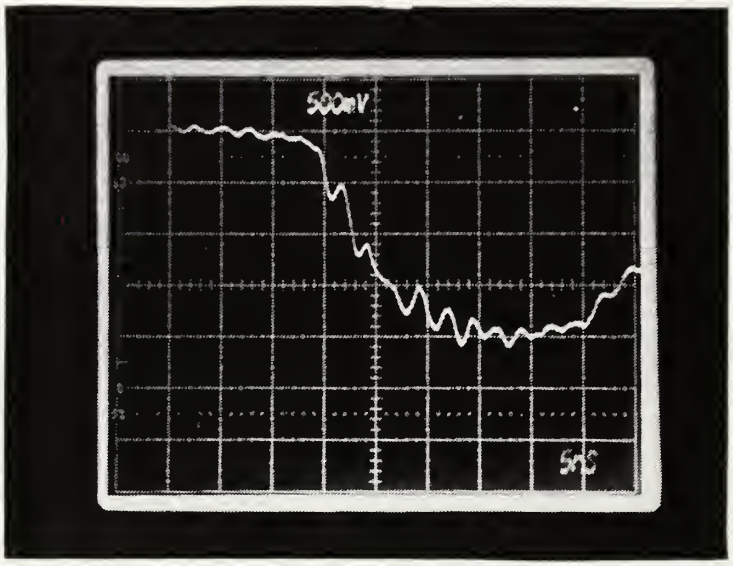

Figure 5.9 Diode Voltage waveform for a 55 kV shot. 0.16 MV/div, 5 ns/div, TBCF=1.08, TDC=3.3 ns.

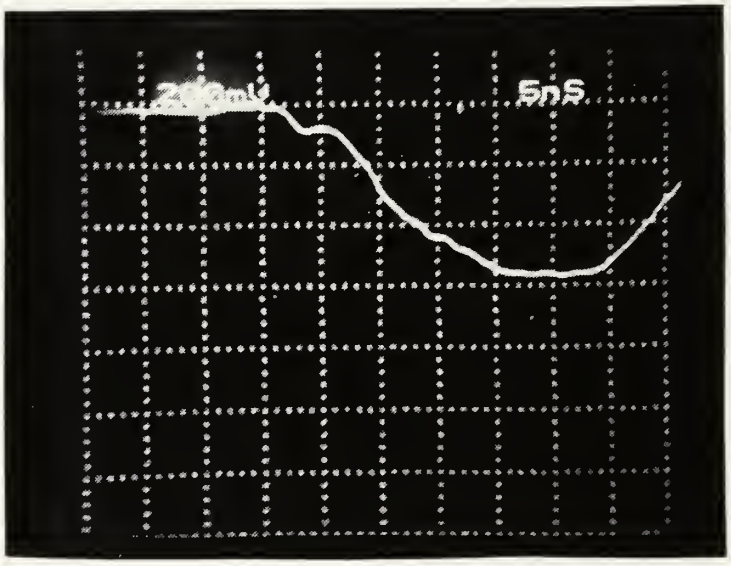

Figure 5.10 Diode Current waveform for a 55 kV shot. 1.46 kA/div, 5 ns/div, TBCF=1, TDC=0 ns.

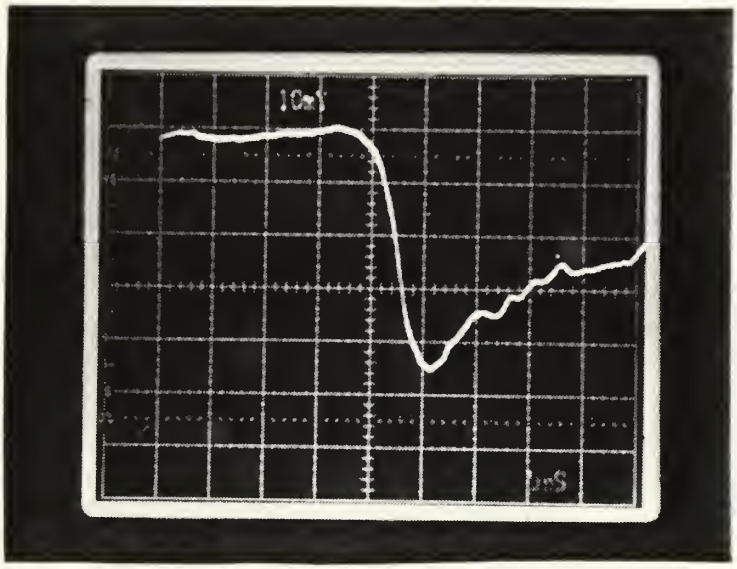

Figure 5.11 Photodiode waveform for a 55 kV shot. TBCF=1.04, TDC=1.9 ns.

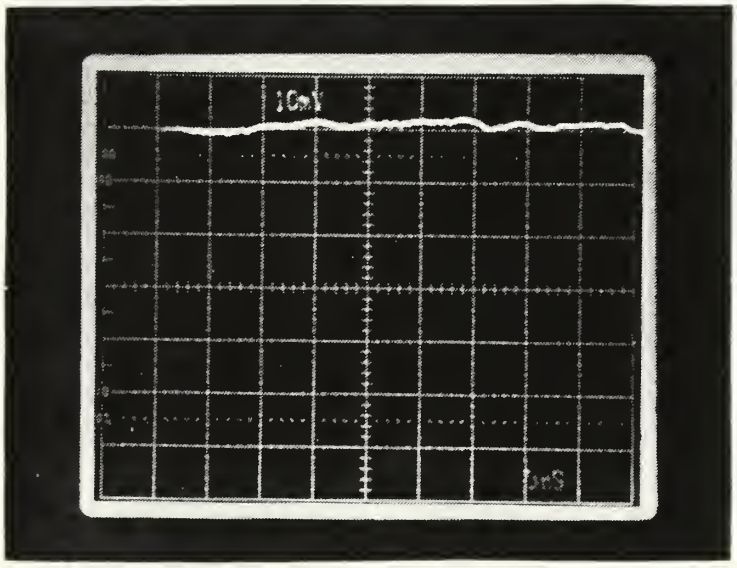

Figure 5.12 Photodiode "dark" signal for a 55 kV shot.

approximately 10 nanoseconds. After some delay, the photodiode signal begins with a very short risetime of approximately 2 nanoseconds. The photodiode signal decays approximately exponentially after the sharp rise.

After correcting the data for the time base discrepancy and the delay correction (Appendix C), the average delay time from the onset of the diode voltage waveform and the onset of the light signal can be calculated. The average time delay for the 9 shots in the 55 kV run was 6.1 nanoseconds with a standard deviation of 0.7 nanoseconds. The average diode voltage at which the onset of the plasma occurred, i.e., the onset of the light pulse, was 390 kV with a standard deviation of 30 kV. Note that the average voltage found here occurs on the rise of the voltage pulse. At that point, the ± 2 ns accuracy of the optical signal could place the actual value anywhere from zero to the maximum voltage. The same is true for the average voltage calculations for the other data runs. The accuracy of the average voltage data based on the ± 2ns time accuracy is approximately +80 kV/-120 kV.

Figures 5.13 through 5.15 display the diode voltage, diode current, and photodiode waveforms, respectively, for a typical 75 kV shot. Figure 5.16 displays the "dark" photodiode signal from a similar 75 kV shot. The waveforms for the other shots in the run are again similar to those displayed. The rise time of the diode voltage waveform and

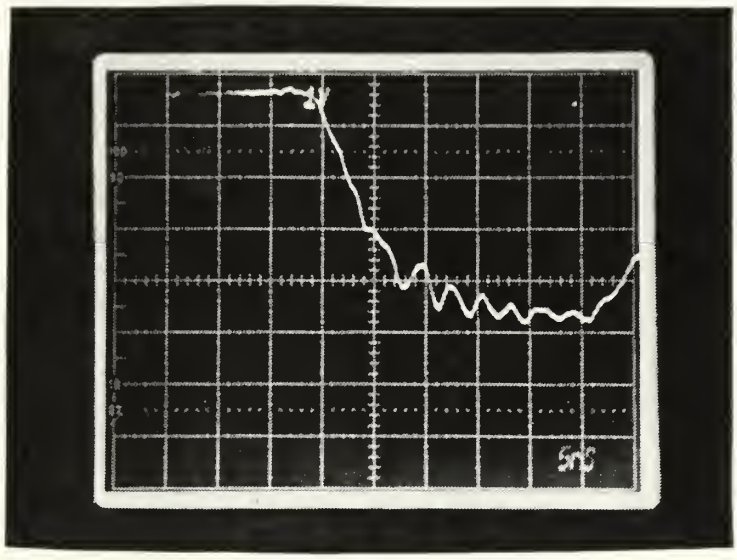

Figure 5.13 Diode Voltage waveform for a 75 kV shot. 0.32 MV/div, 5 ns/div, TBCF=1.08, TDC=2.2 ns.

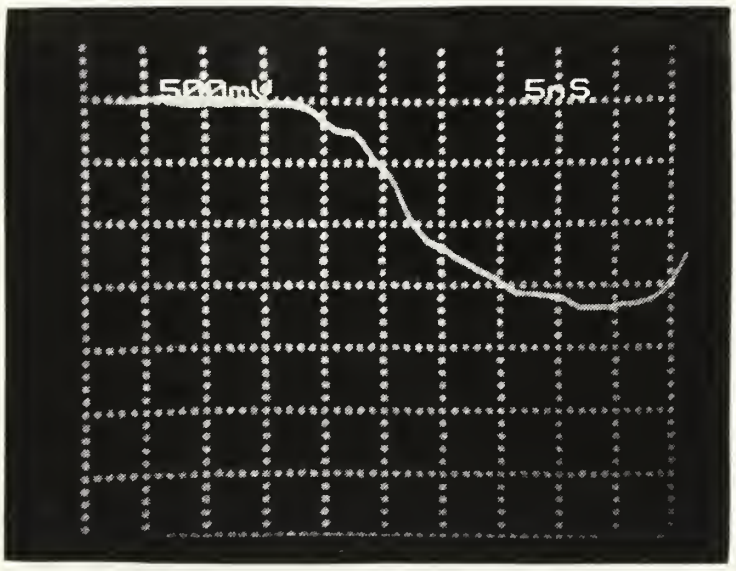

Figure 5.14 Diode Current waveform for a 75 kV shot. 3.66 kA/div, 5 ns/div, TBCF=1, TDC=0 ns.

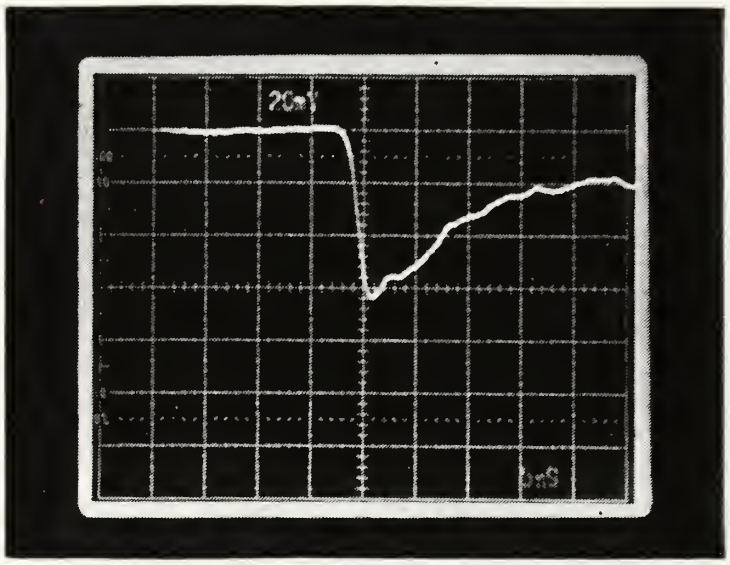

Figure 5.15 Photodiode waveform for a 75 kV shot. TBCF=1.04, TDC=.5 ns.

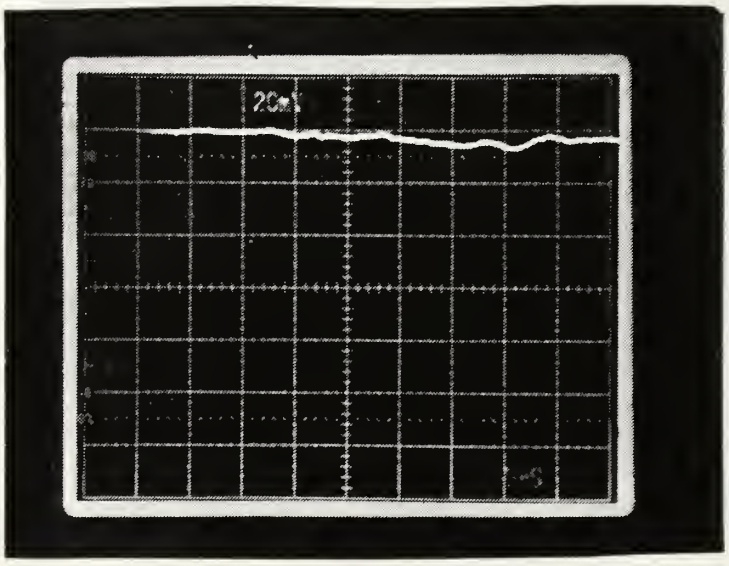

Figure 5.16 Photodiode "dark" signal for a 75 kV shot.

the photodiode signal waveforms are similar to the 55 kV shots.

The average delay time for the 10 shots in the 75 kV run was 5.6 nanoseconds with a standard deviation of 0.8 nanoseconds. The average diode voltage at the onset of plasma formation for the 75 kV shots is 630 kV with a standard deviation of 40 kV. The time accuracy induced error in this average diode voltage is approximately +100 kV/-150 kV.

Figures 5.17 through 5.19 display the diode voltage, diode current, and photodiode waveforms, respectively, for a typical 100 kV shot. Figure 5.20 displays the "dark" photodiode signal from a similar 100 kV shot. Notice the relatively large "dark" signal of the 100 kV shots. This is largely due to the increased electromagnetic pulse as well as the higher energy x-rays produced during the 100 kV shots. The diode voltage and diode current waveforms for the other shots in the run are similar to those displayed.

The shape of the photodiode waveform varies greatly from shot to shot in the 100 kV run. Figure 5.21 is the photodiode waveform for another shot of the 100 kV run. The timing of the onset, however, is similar in all of the photodiode waveforms of the data run. The rise time of the diode voltage pulse is similar to the other data runs but the photodiode signal rise time is slightly longer. This is likely due to the superposition of the slowly rising dark signal on top of the quickly rising photodiode signal.

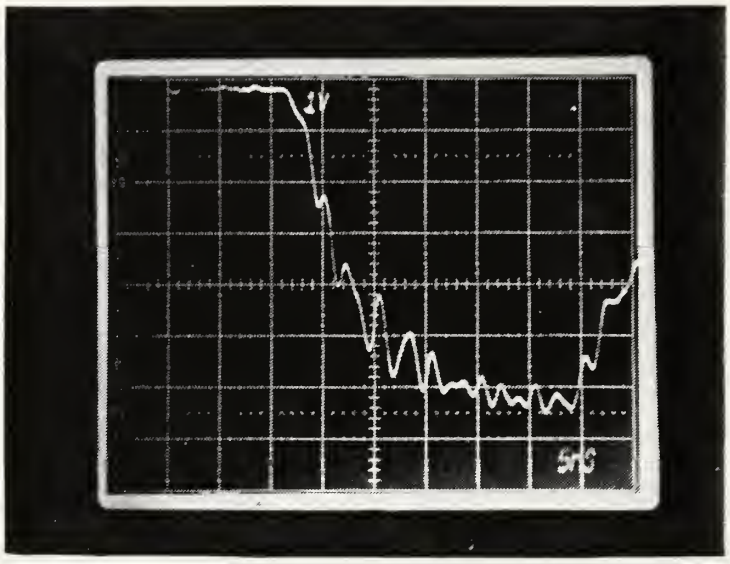

Figure 5.17 Diode Voltage waveform for a 100 kV shot. 0.32 MV/div, 5 ns/div, TBCF=1.08, TDC=3.0 ns.

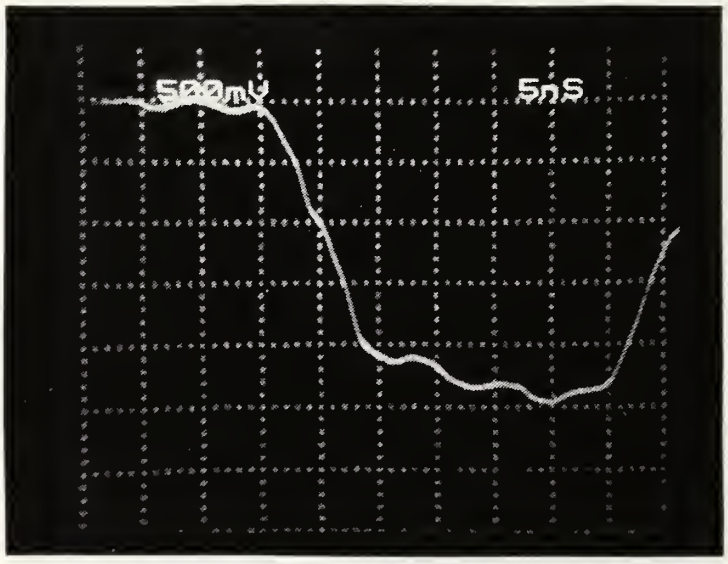

Figure 5.18 Diode Current waveform for a 100 kV shot. 3.66 kA/div, 5 ns/div, TBCF=1, TDC=0 ns.

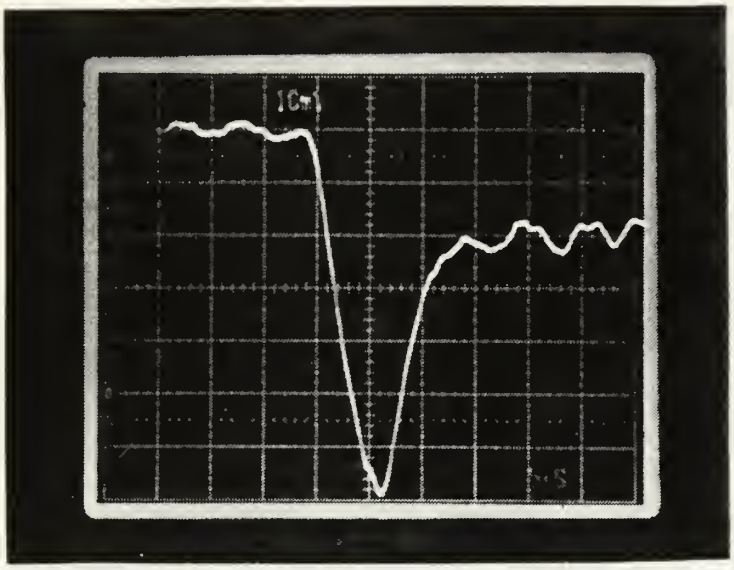

Figure 5.19 Photodiode waveform for a 100 kV shot. TBCF=1.04, TDC=2.0 ns.

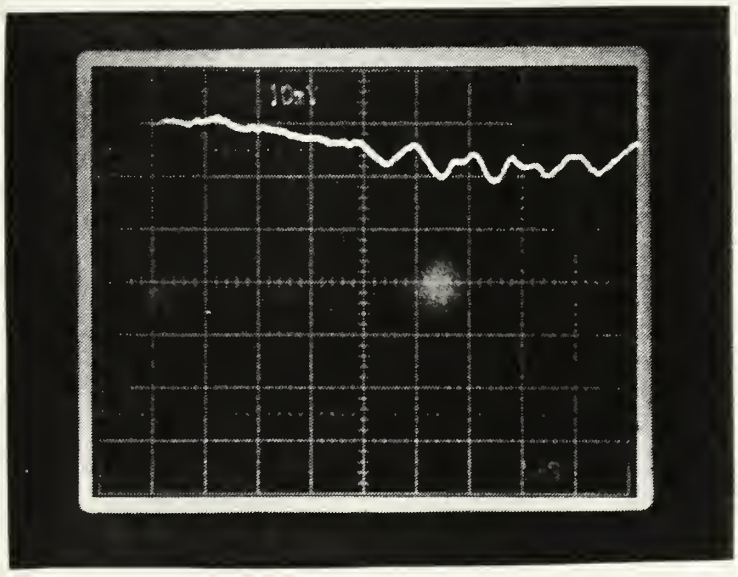

Figure 5.20 Photodiode "dark" signal for a 100 kV shot.

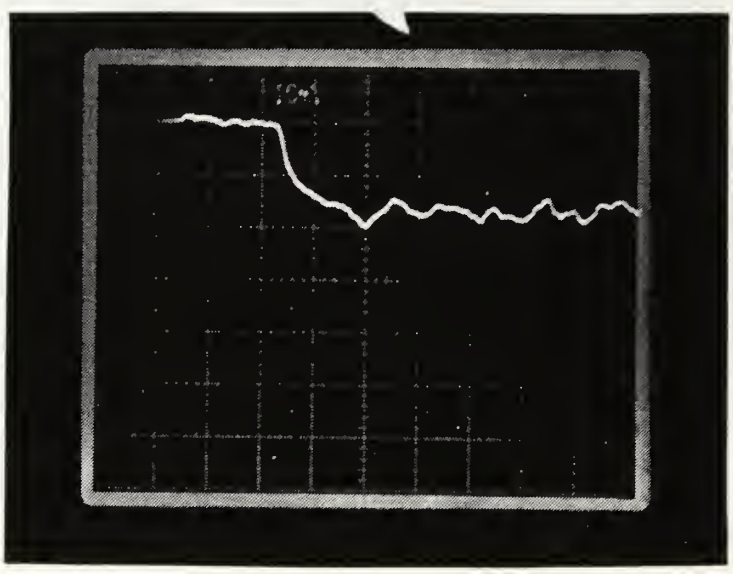

Figure 5.21 Photodiode waveform for a particular 100 kV shot. When compared to Figure 5.19 this illustrates that the photodiode waveforms of the 100 kV shots were not all similar.

The average delay time for the 11 shots of the 100 kV run was 3.7 nanoseconds with a standard deviation of 0.7 nanoseconds. The average diode voltage at the onset of plasma formation for the 100 kV shots is 590 kV with a standard deviation of 90 kV. The time accuracy induced error in this average diode voltage is approximately +500 kV/-300 kV. A summary of the results of all three data runs is given in Table 5.1. The data used to compute the averages are listed in Appendix F. The TBCF and TDC have been applied. Note that the onset of diode voltage signal and onset of the light signal here are arbitrarily defined as the point where each signal begins its steep rise.

Table 5.1 SUMMARY OF RESULTS.

Marx Charge (KV)	Average Time Delay of Onset (ns)	Average Diode Voltage at Onset (kV)
55	6.1 ± 2	390 +80/-120
75	5.6 ± 2	630 +100/-150
100	3.7 ± 2	590 +500/-300

C. ANALYSIS OF DATA

1. Digitizing the Waveforms

The oscilloscope traces in the preceding section are difficult to compare to each other due to the time base discrepancy described earlier. It is also tedious to analyze the physics of the diode while juggling numerous correction factors and instrument sensitivities. Therefore, it is advantageous to digitize the waveforms and load them into a computer for scaling, corrections, and analysis. The diode voltage, diode current, and photodiode waveforms from the representative shots displayed above have been digitized, corrected for the time base discrepancy and delay correction, and converted into the appropriate units. The conversions from oscilloscope vertical deflection to diode voltage and diode current are given in Appendix B. The photodiode signal has been corrected for timing but no conversion of units was done. This is due to the fact that the absolute intensity of

the light measured by the photodiode is not needed to investigate the timing of the plasma formation.

Figures 5.22 through 5.24 are the digitized waveforms of the diode voltage, diode current, and photodiode signal for the 55 kV shot displayed in the previous section. Note that the time axis on all three plots are synchronized and that the zero time is chosen arbitrarily at a time prior to the onset of the voltage pulse. Figure 5.25 plots the three waveforms on an arbitrary vertical scale for easy time comparison.

Figures 5.26 through 5.28 are the digitized waveforms of the diode voltage, diode current, and photodiode signal for the 75 kV shot displayed in the previous section. Figure 5.29 plots the three waveforms on an arbitrary vertical scale.

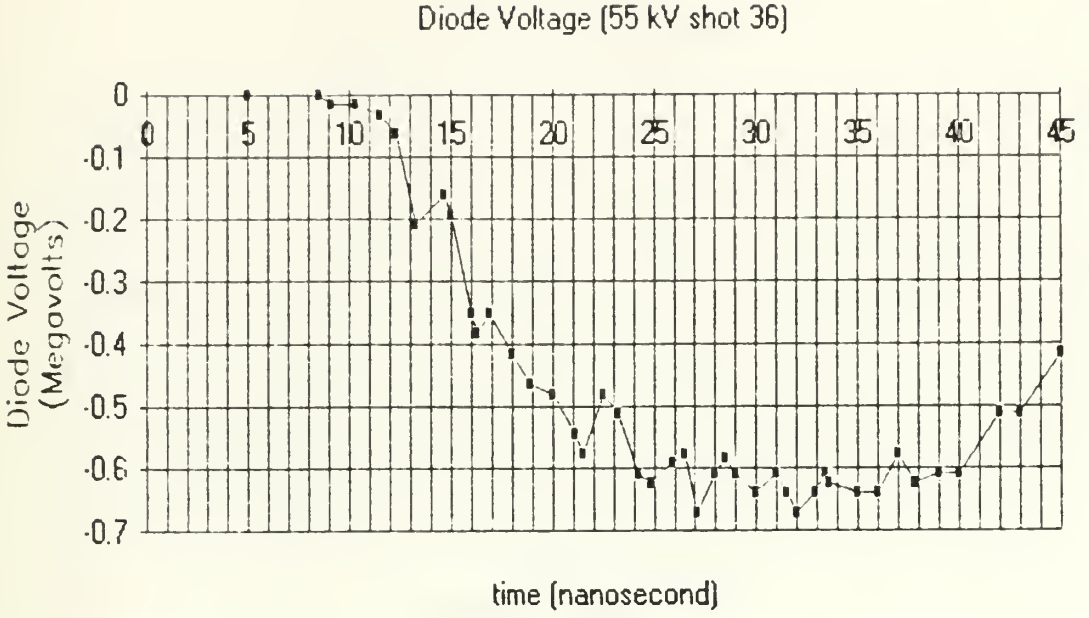

Figure 5.22 Diode Voltage waveform for a 55 kV shot. The zero of time is arbitrarily chosen.

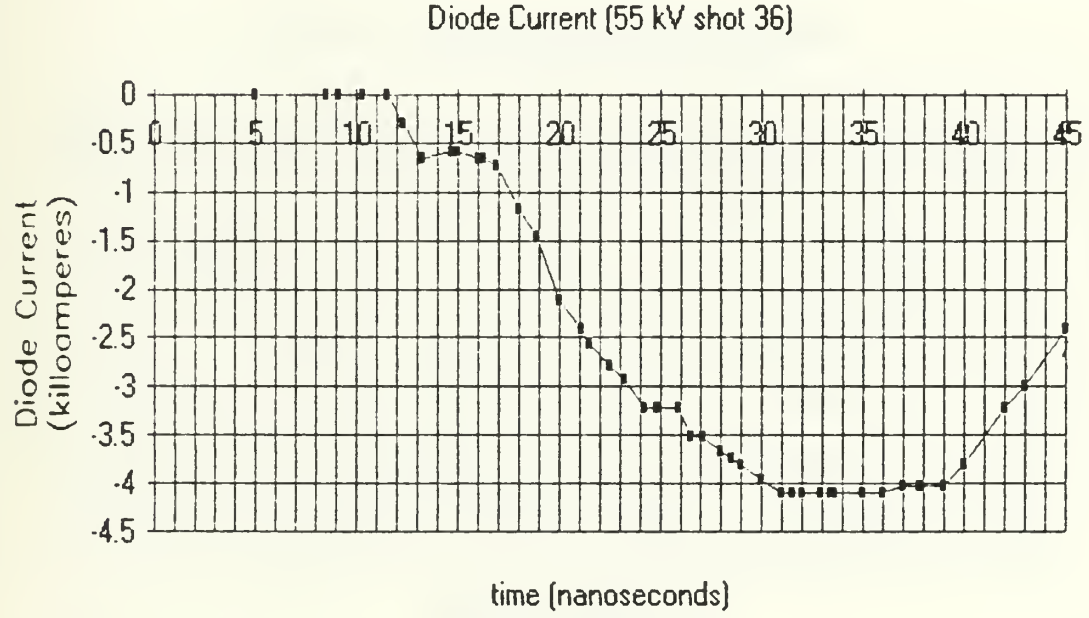

Figure 5.23 Diode Current waveform for a 55 kV shot. Same arbitrary zero time as Figure 5.22.

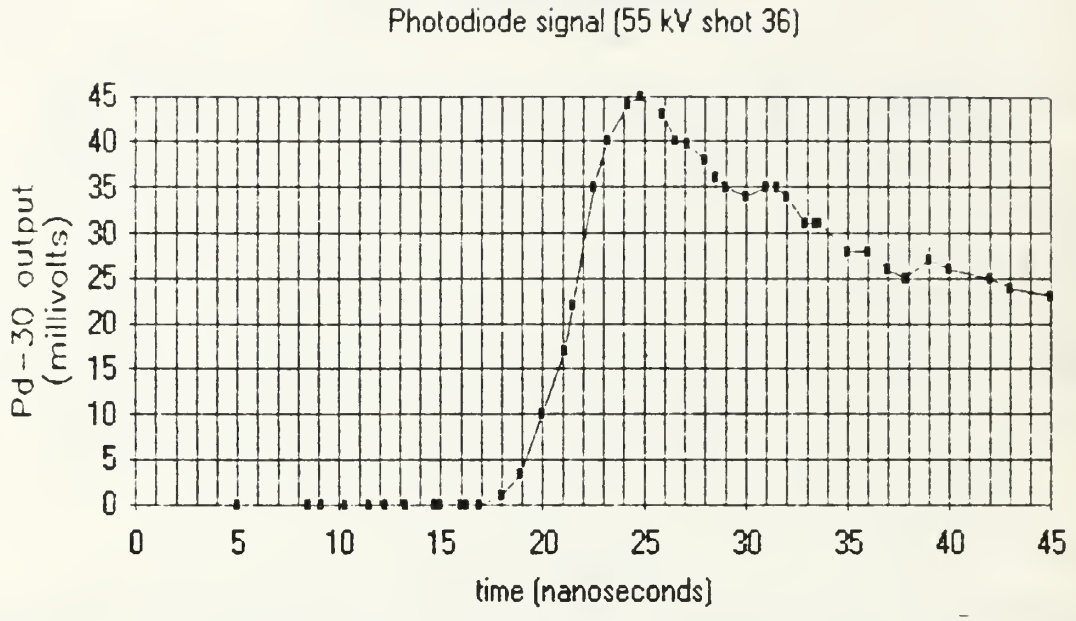

Figure 5.24 Photodiode waveform for a 55 kV shot. Same arbitrary zero time as Figure 5.22.

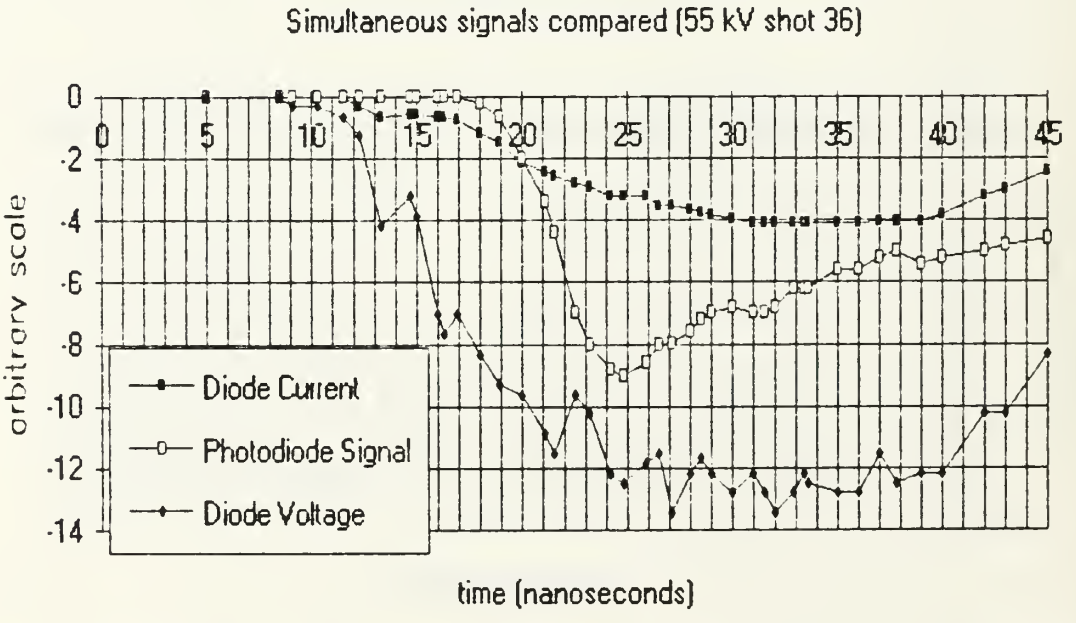

Figure 5.25 Diode Voltage, Diode Current, and Photodiode waveforms for a 55 kV shot plotted on an arbitrary vertical scale.

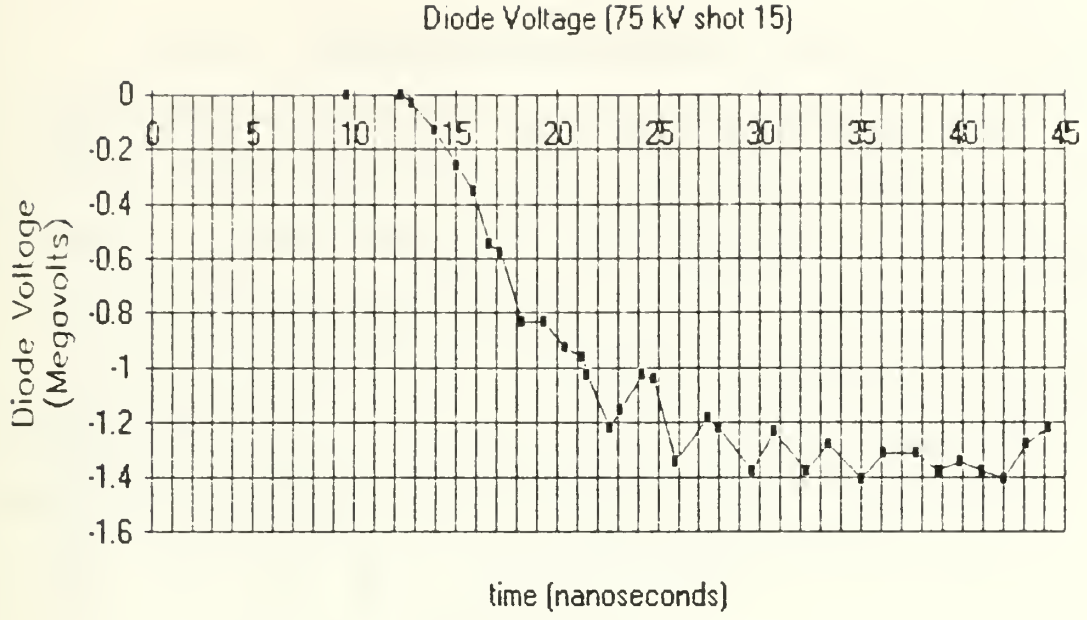

Figure 5.26 Diode Voltage waveform for a 75 kV shot. The zero of time is arbitrarily chosen.

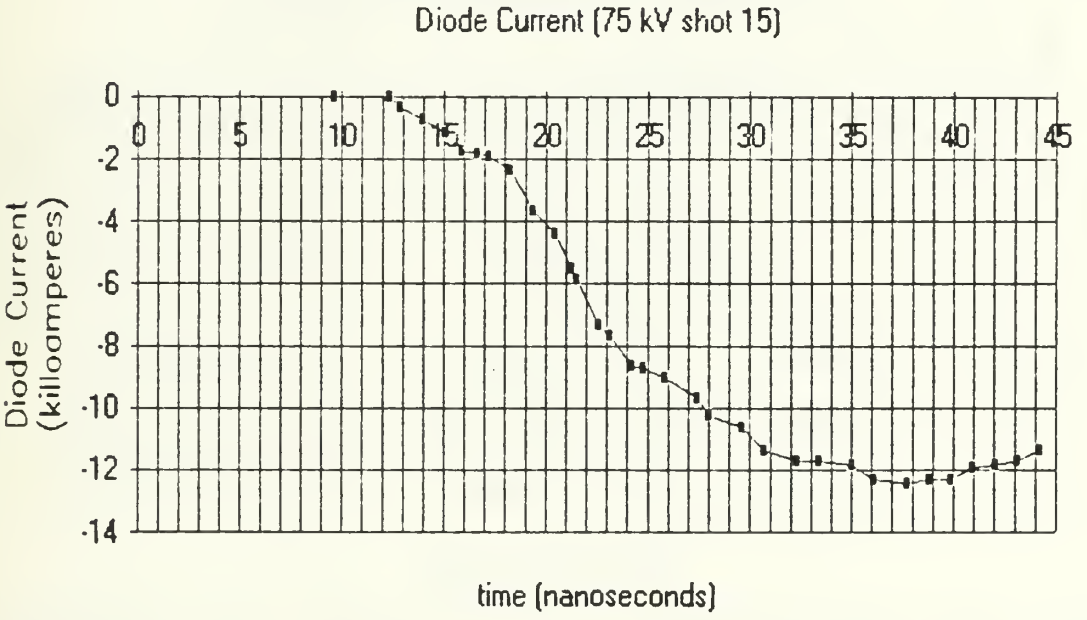

Figure 5.27 Diode Current waveform for a 75 kV shot. Same arbitrary zero time as Figure 5.26.

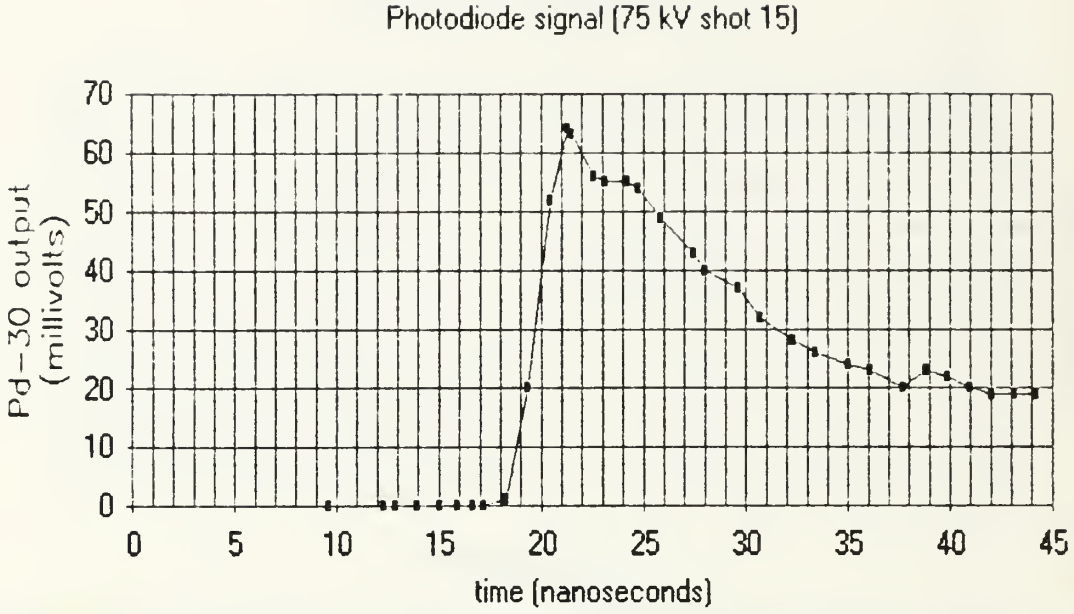

Figure 5.28 Photodiode waveform for a 75 kV shot. Same arbitrary zero time as Figure 5.26.

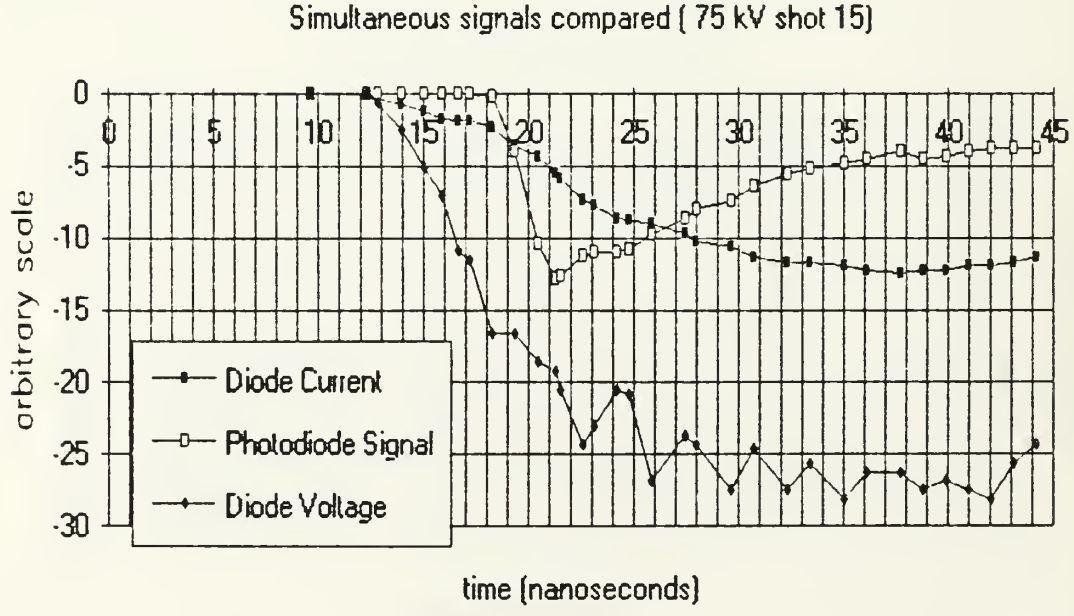

Figure 5.29 Diode Voltage, Diode Current, and Photodiode waveforms for a 75 kV shot plotted on an arbitrary vertical scale.

Figures 5.30 through 5.32 are the digitized waveforms of the diode voltage, diode current, and photodiode signal for the 100 kV shot displayed in the previous section. Figure 5.33 plots the three waveforms on an arbitrary vertical scale.

2. Comparison to Theory

Now that the diode voltage and current waveforms have been digitized, it is trivial to compare them to the theory of the planar diode from Chapter II.

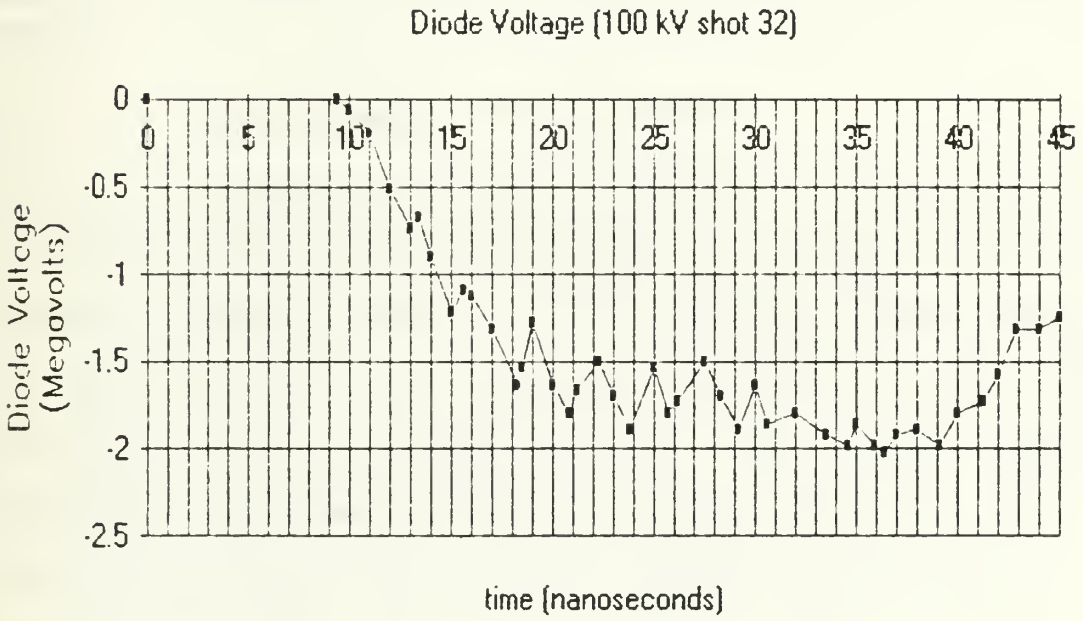

Figure 5.30 Diode Voltage waveform for a 100 kV shot. The zero of time is arbitrarily chosen.

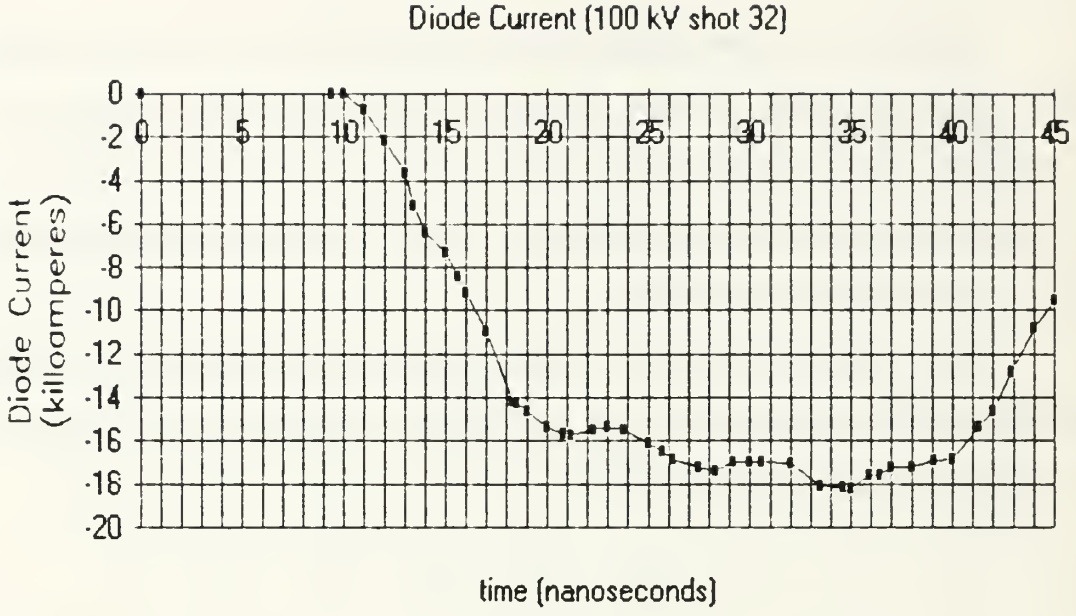

Figure 5.31 Diode Current waveform for a 100 kV shot. Same arbitrary zero time as Figure 5.30.

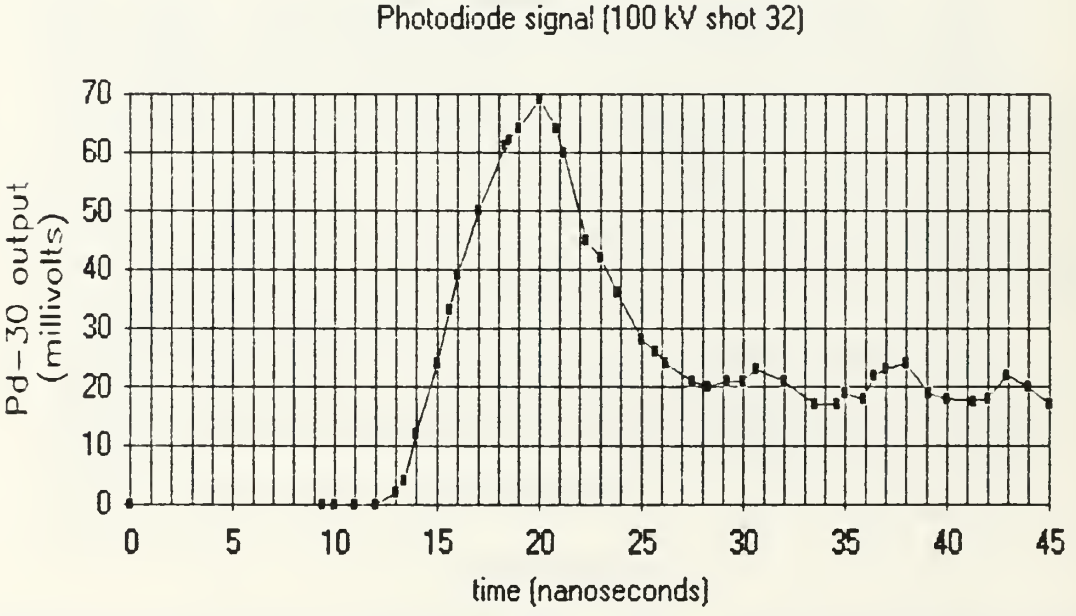

Figure 5.32 Photodiode waveform for a 100 kV shot. Same arbitrary zero time as Figure 5.30.

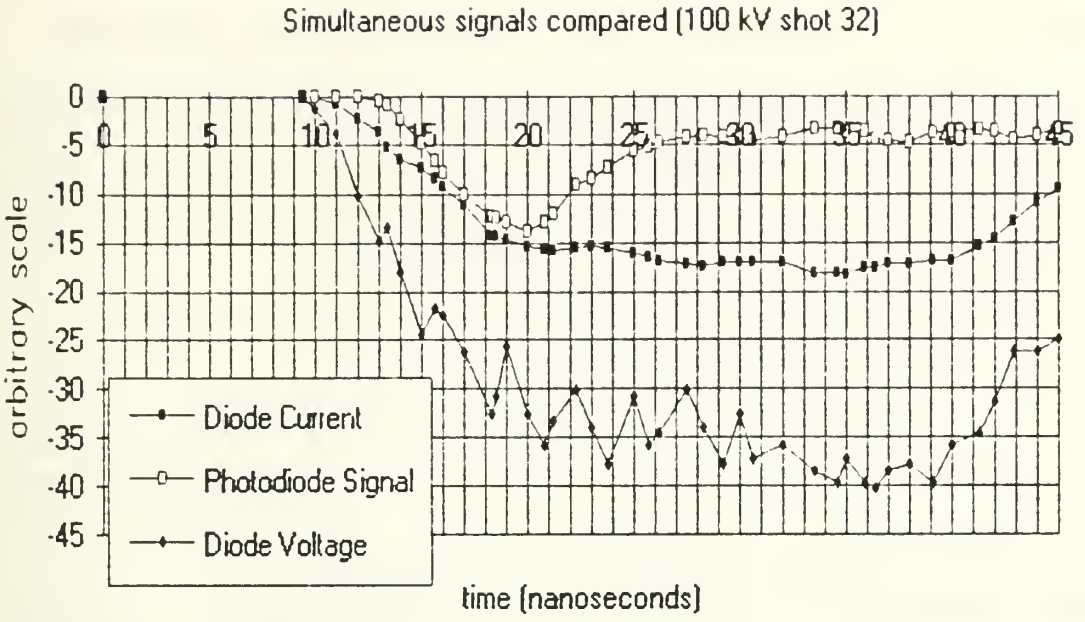

Figure 5.33 Diode Voltage, Diode Current, and Photodiode waveforms for a 100 kV shot plotted on an arbitrary vertical scale.

a. Relativity

It must be determined whether or not the diode is relativistic so the appropriate theoretical treatment can be applied. Using Equation 2.2 and the voltage across the diode, the Lorentz factor, γ, for an electron in the diode can be calculated. The γ changes as the diode voltage changes. Therefore, it is best to calculate the maximum value of γ for each of the shots. The γ for an electron in the diode is 2.2, 3.5, and 5 for the 55 kV, 75 kV, and 100 kV shots respectively. These values can be compared to figure 2.1 to determine if a non-relativistic treatment is justified. Only

the peak voltage of the 100 kV shot begins to deviate significantly from the non-relativistic limit for the diode impedance. Therefore, the non-relativistic treatment is justified for the lower voltage shots and the early portion of the 100 kV shot. Since it is the early portion of the waveforms that are of interest here, the non-relativistic treatment will be used for all of the shots.

b. Parapotential Flow

The cathode radius is measured to be r_c=1.6 cm and the diode gap is d=2.54 cm. Using these values and the values for γ given above in Equation 2.6, the critical current below which parapotential flow is insignificant can be calculated. The result is that I_c= 11.6 kA, 18.5 kA, and 21.2 kA for the 55 kV, 75 kV, and 100 kV shots respectively. Since the peak diode currents obtained in this experiment were 4.1 kA, 12.2 kA, and 18.0 kA for the 55 kV, 75 kV, and 100 kV shots respectively, the parapotential flow can be neglected.

c. Child-Langmuir Limit

Equation 2.5 can be applied to the diode voltage data to determine the Child-Langmuir limited current density. Since the area of conduction is not known for this diode, the current density limit cannot be directly converted into a current limit with which the diode current data can be compared. It is helpful to define a parameter called the effective area such that

$$A_{eff} = \frac{I}{j_{CL}} \quad , \qquad (5.1)$$

where I is the measured diode current. The values for j_{CL} are found by inserting the measured diode voltage data into Equation 2.5. The plasma expands negligibly during the 30 ns pulse width so that the diode gap size can be used for d in the equation. Figures 5.34 through 5.36 plot the effective area as a function of time for the 55 kV, 75 kV and 100 kV shots respectively.

It is important to note that Equation 2.5 does not apply to a displacement current density. When the voltage pulse begins to charge the diode, the diode current monitor detects the displacement current. The Child-Langmuir limit will not apply until a real current is flowing across the diode. No current will flow across the diode until enhanced field emission begins at an electric field of approximately 10 MV/m. Points on the effective area plots are meaningless until field emission begins. Figures 5.37 through 5.39 indicate the times at which the electric field strength reached the 10 MV/m necessary to cause enhanced field emission of electrons for the 55 kV, 75 kV, and 100 kV shots respectively. Figures 5.34 through 5.36 indicate that the effective area parameter begins small when field emission

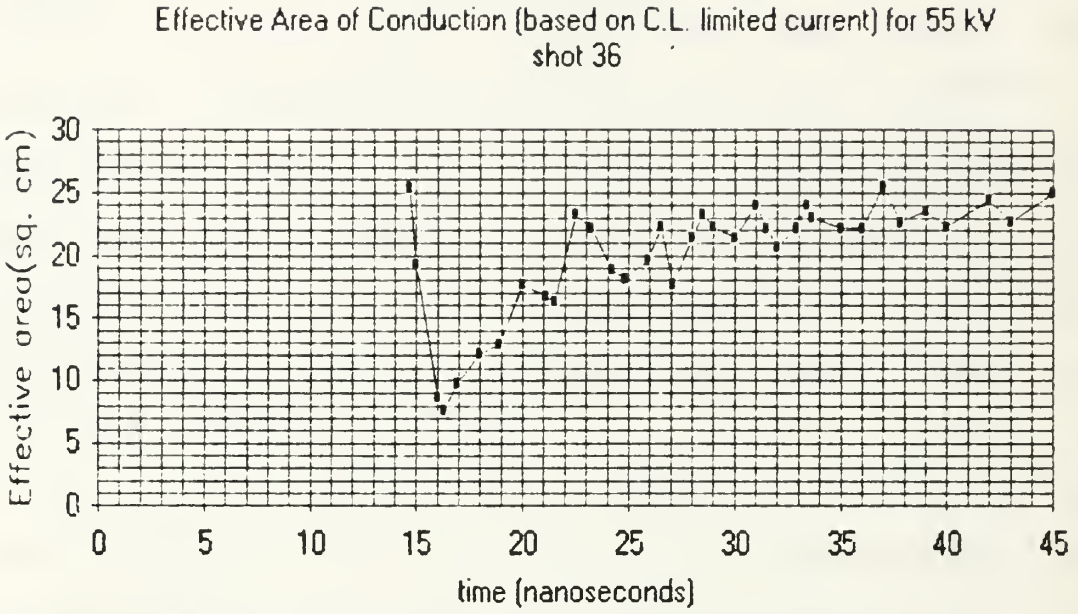

Figure 5.34 Effective area (Equation 5.1) vs. time for a 55 kV shot.

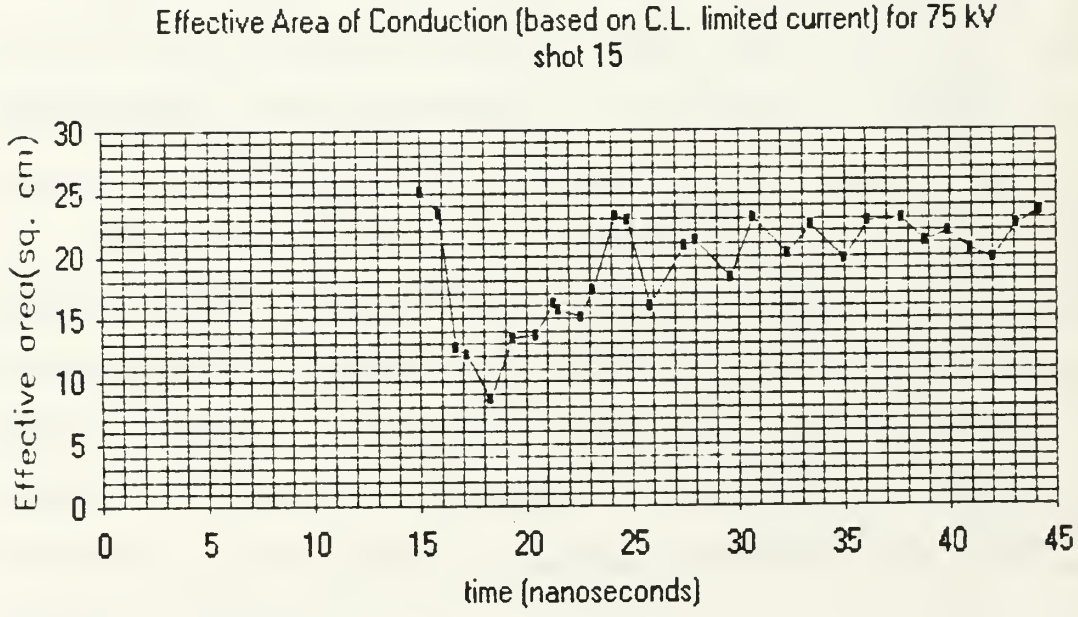

Figure 5.35 Effective area (Equation 5.1) vs. time for a 75 kV shot.

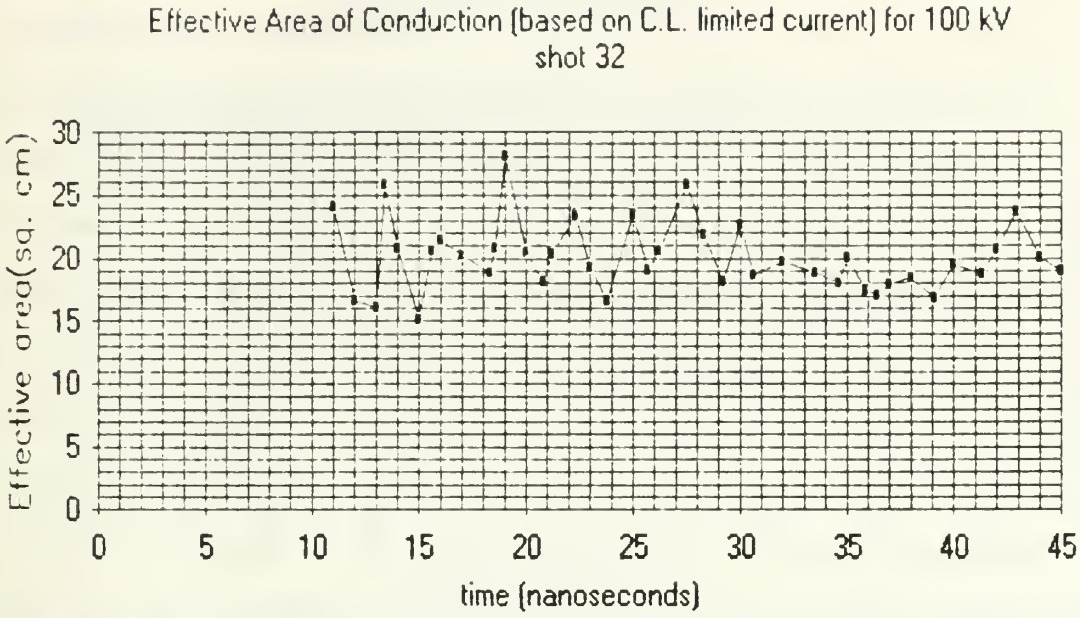

Figure 5.36 Effective area (Equation 5.1) vs. time for a 100 kV shot.

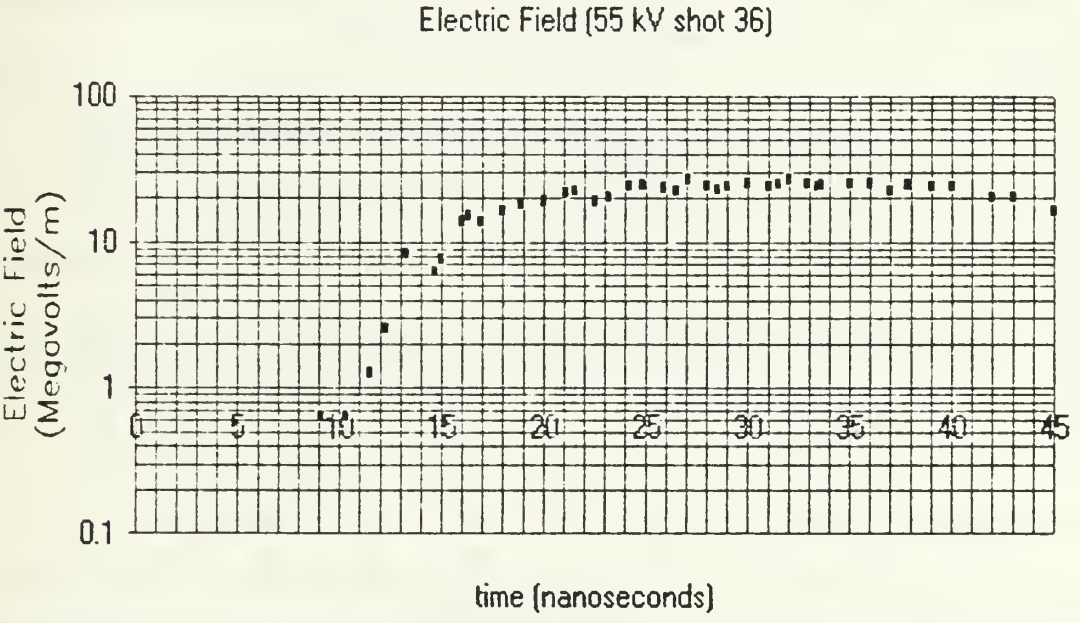

Figure 5.37 Electric Field vs. time for a 55 kV shot. The field crosses the 10 MV/m value at approximately 15 ns.

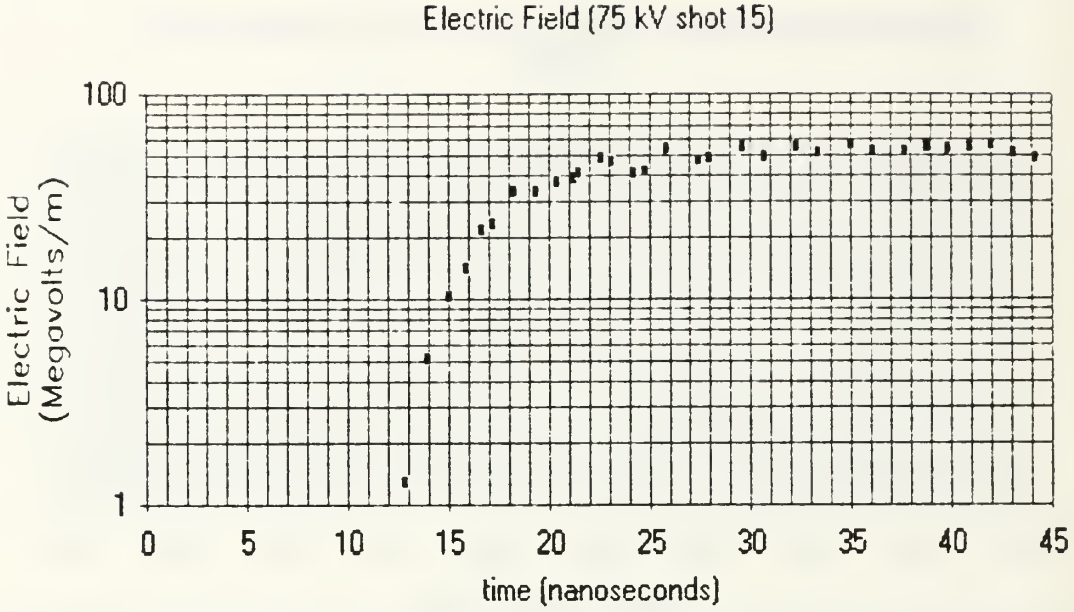

Figure 5.38 Electric Field vs. time for a 75 kV shot. The field crosses the 10 MV/m value at approximately 15 ns.

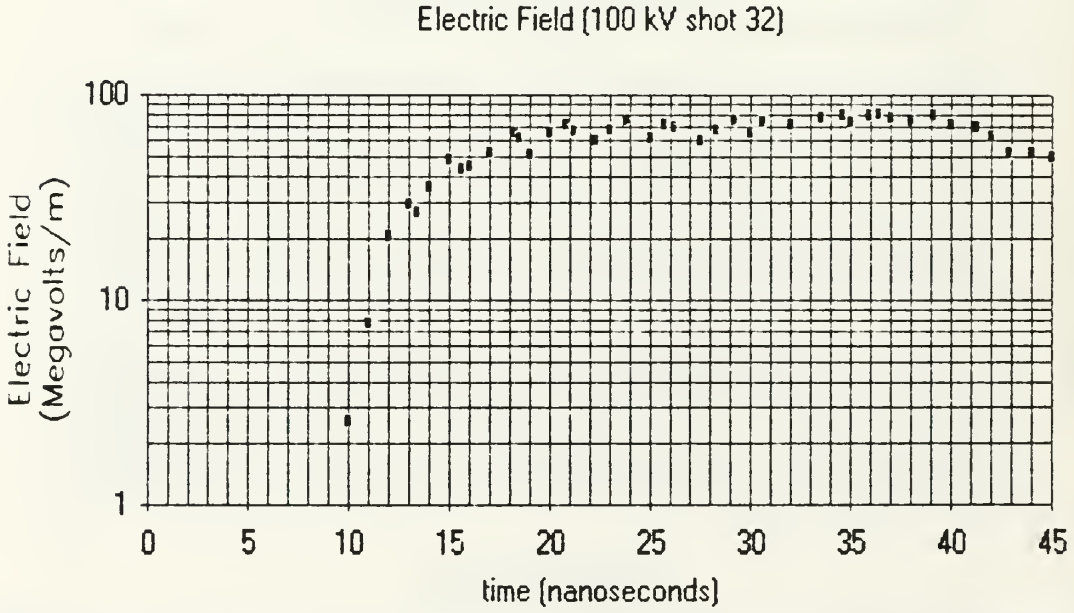

Figure 5.39 Electric Field vs. time for a 100 kV shot. The field crosses the 10 MV/m value at approximately 11 ns.

starts and then increases to a steady value. This can be interpreted as the diode current beginning as a small field emission current which quickly becomes Child-Langmuir limited. Once the current reaches the limit, the effective area parameter should take on the physical significance of a real area. One result of the three effective area plots shown is that they all approach an area of approximately 20 cm^2. It should be noted that due to the ± 12 % accuracy of the diode voltage and diode current data, the effective area parameter has an estimated accuracy of ± 22 %. The physical area of the cathode is approximately 8 cm^2 and the area of the anode is approximately 50 cm^2. The second result of the effective area plots is that the effective area parameter reaches its stable value more quickly on the higher voltage shots. This indicates that the current becomes Child-Langmuir limited more rapidly on the higher voltage shots.

d. Summary of comparison

Based on the comparison of the data to the planar diode theory discussed in Chapter II, the FXR diode used in the experiment does not significantly differ from a non-relativistic planar diode.

3. Comparison to Model

Now that data from a time varying voltage waveform is available, the procedure outlined in Chapter II.F.2 can be used to predict the onset of plasma formation. Figures 5.40

through 5.42 indicate the predictions for the 55 kV, 75 kV, and 100 kV shots respectively. The predicted delay times of plasma onset are 13 ns for the 55 kV shot, 8 ns for the 75 kV shot, and 6 ns for the 100 kV shot. These predicted times all fall on the sharp rise of their respective photodiode waveforms. The prediction is expected to lag the actual onset of plasma formation because the ionization cross section for the desorbed neutrals is not a step function which turns on suddenly at 100 eV. The cross section for ionization may be nearly as significant at 75 V potential as it is at 100 V thus the ionization will begin before the prediction (approximately 1 ns before on the 75 kV shot). It should also be noted that the model assumes that the neutrals travel away from the cathode with the sound velocity in air. Lighter molecules, such as H_2O and CH_4, would travel faster than predicted thus reaching the 100 V equipotential surface quicker than predicted.

The experiment showed a very rapid risetime for the onset of plasma formation. This is a reasonable consequence of the model. The dense region of desorbed neutrals expanding on the nanosecond time scale ($\approx$0.3 μm/ns) is met by the 100 V equipotential surface which is also traveling on the nanosecond time scale ($\approx$1.5 μm/ns for the 75 kV shot). These two regions proceed from a no overlap condition to a significant amount of overlap on the nanosecond time scale. This results in the sharp risetime for the onset of plasma.

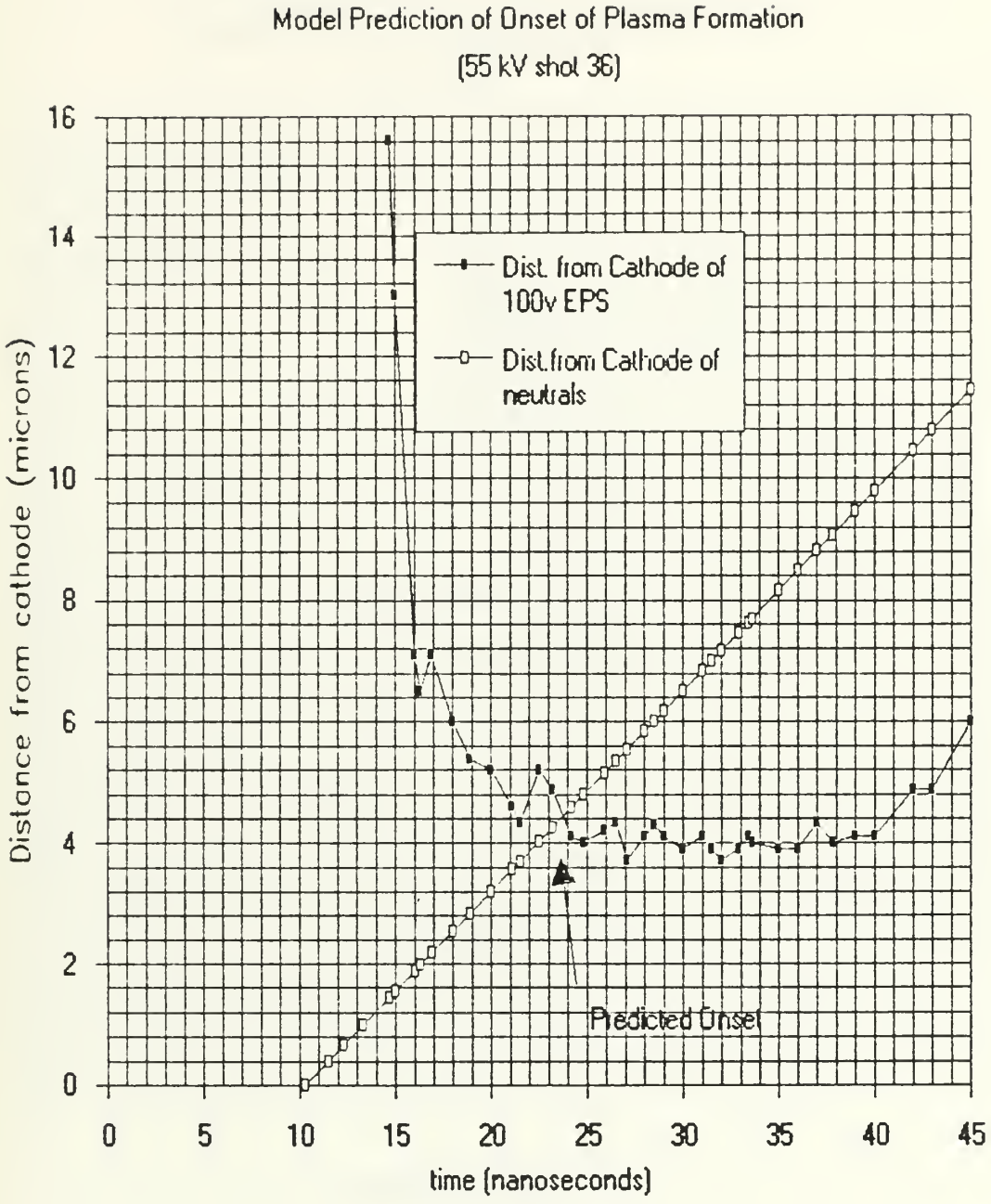

Figure 5.40 Distance from the cathode of the 100 V equipotential surface (EPS) and distance from cathode of expanding neutrals vs. time for a 55 kV shot. Delay from voltage onset =13 ns.

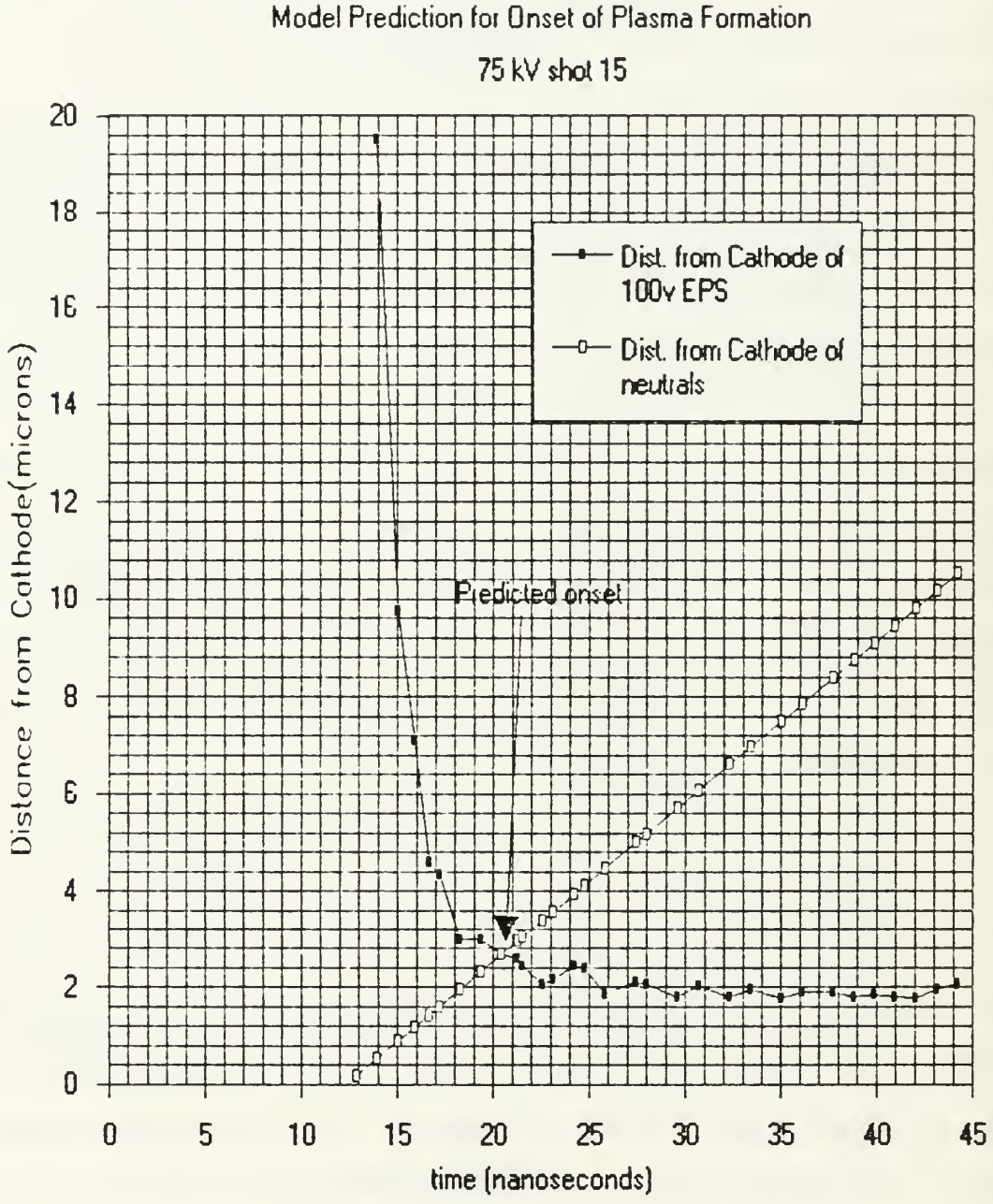

Figure 5.41 Distance from the cathode of the 100 V equipotential surface (EPS) and distance from cathode of expanding neutrals vs. time for a 75 kV shot. Delay from voltage onset = 8 ns.

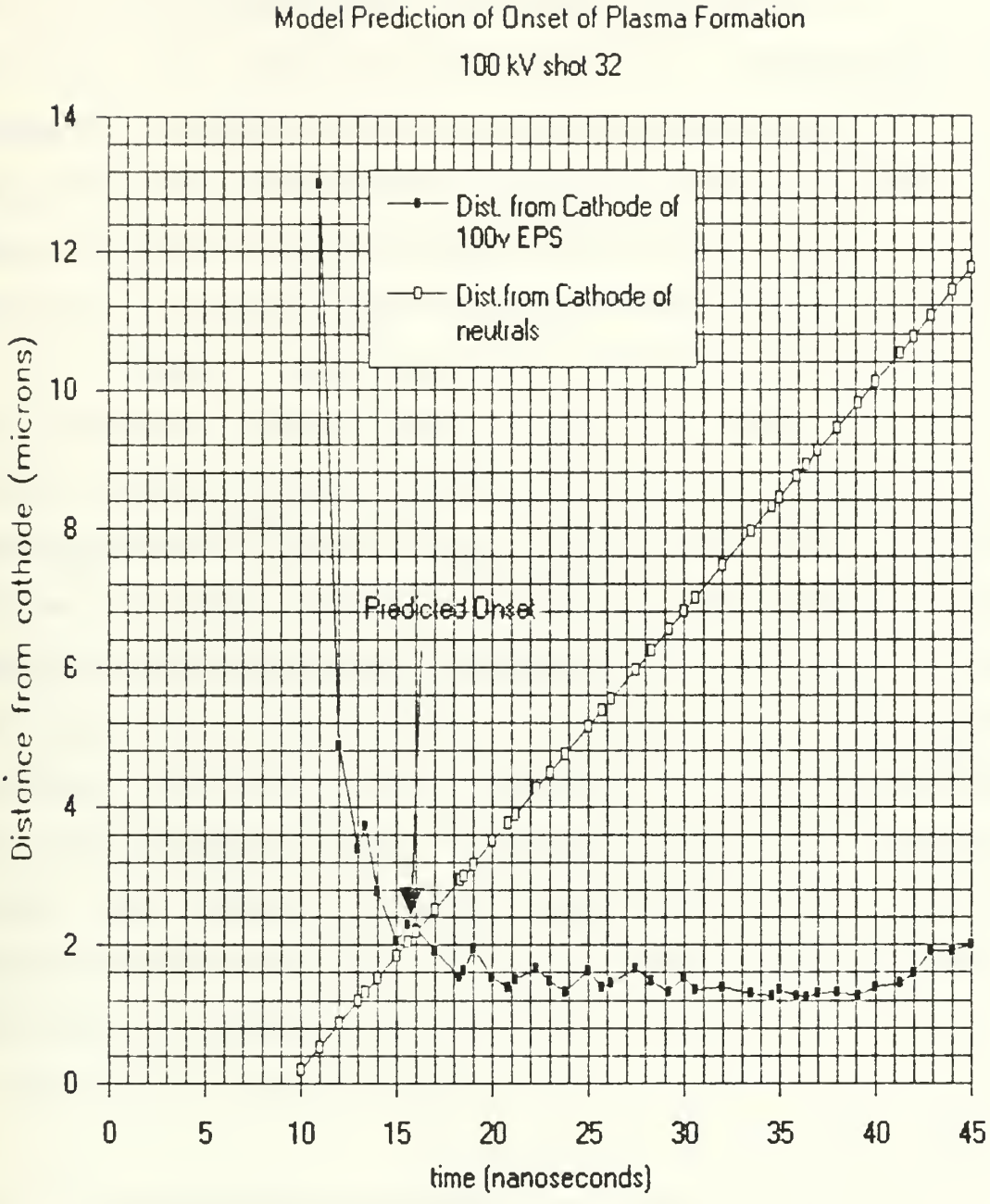

Figure 5.42 Distance from the cathode of the 100 V equipotential surface (EPS) and distance from cathode of expanding neutrals vs. time for a 100 kV shot. Delay from voltage onset = 6 ns.

VI. CONCLUSIONS AND RECOMMENDATIONS

A. CONCLUSIONS

The whisker explosive emission model does not adequately describe the onset of plasma formation in the fast pulsed vacuum diode. The model requires field emitted current densities much higher than the Child-Langmuir limit but provides no mechanism for that condition to occur.

The new model discussed in this thesis involves a very dense desorbed neutral gas traveling away from the cathode surface. The onset of the electric field is the mechanism which causes the desorption. Field emitted electrons traveling away from the cathode surface have their greatest probability of ionizing the neutrals when they have approximately 100 eV of energy (i.e., when they reach the 100 volt equipotential surface). In a pulsed diode, the 100 volt equipotential surface moves toward the cathode surface as the desorbed neutrals move away from the cathode surface. For a given waveform of the voltage pulse, the time delay from the onset of the voltage pulse to the onset of plasma formation can be predicted.

The experiment performed measured the diode voltage, diode current, and relative intensity of light emitted from the diode as simultaneous functions of time. The light emitted is

due to the de-excitation process which occurs essentially simultaneously with the excitation and ionization processes. Light is also emitted due to the recombination process within the plasma. The sudden appearance of light is interpreted as the onset of plasma formation on the cathode surface of the diode (the lens system was focused on the diode surface). The time lapsed photographs suggest that plasma formation also occurs on the anode surface. The shape of the trailing edge of the light pulse may be the result of recombination within the plasma.

The diode voltage and diode current waveforms taken during the experiment were shown to be consistent with known diode physics. The time delay of the onset of plasma formation was experimentally measured for three different operating voltages of the diode. The voltages at which the onset of plasma formation occurred were also determined. Table 6.1 displays the experimental results. The experiment also shows that the plasma onset has a very rapid rise time (~2 ns). This is consistent with the model. The model predictions are given in Table 6.2.

Table 6.1 SUMMARY OF EXPERIMENTAL RESULTS.

Marx Charge (kV)	Average Time Delay of Onset of Plasma Formation (ns)	Average Diode Voltage at Onset of Plasma Formation (kV)
55	6.1 ± 2	390 +80/-120
75	5.6 ± 2	630 +100/-150
100	3.7 ± 2	590 +500/-300

Table 6.2 SUMMARY OF MODEL PREDICTIONS.

Marx Charge (kV)	Predicted Delay of Onset (ns)	Predicted Diode Voltage at Onset (kV)
55	13	500
75	8	900
100	6	1250

The time delay predictions are consistently higher than the experimental results because the ionization of neutrals occurs in a region surrounding the 100 volt equipotential surface and thus plasma onset actually occurs earlier than the arrival of the 100 volt equipotential surface. The voltage at onset predictions are directly based on the time delay predictions and are high for the same reasons. Another factor causing the predicted onset to be later than the measured

onset is the presumption of the model that the neutrals travel at the sound velocity in air. Lighter molecules, such as H_2O and CH_4, will travel with a faster velocity causing a shorter delay time than predicted.

The results of the time lapsed photography suggest that the plasma formation occurs near the surfaces of the diode. This is also consistent with the model.

B. RECOMMENDATIONS

Since the speed of the desorbed neutrals depends on their mass, a series of experiments should be performed in which surface contaminants of greatly different masses are used. This might be accomplished by coating the cathode surface with different materials. Successful predictions under such circumstances would increase confidence in the model.

The shape of the trailing edge of the plasma formation light pulse should be investigated. If the decay of the pulse is due to recombination within the plasma, a curve fit through the data may provide information about the plasma density shortly after the onset of plasma formation.

APPENDIX A - DESCRIPTION OF THE NPS FLASH X-RAY FACILITY

A. FLASH X-RAY FACILITY BASIC DESCRIPTION

The NPS Flash X-Ray Facility uses a Model 112A Pulserad Pulsed X-Ray Generator built by the Physics International Company. The major components of the system are the Marx Generator, Blumlein Pulse Generator, and the Electron Accelerator Tube (vacuum diode). These components are depicted in Figure A.1 [Ref. 12].

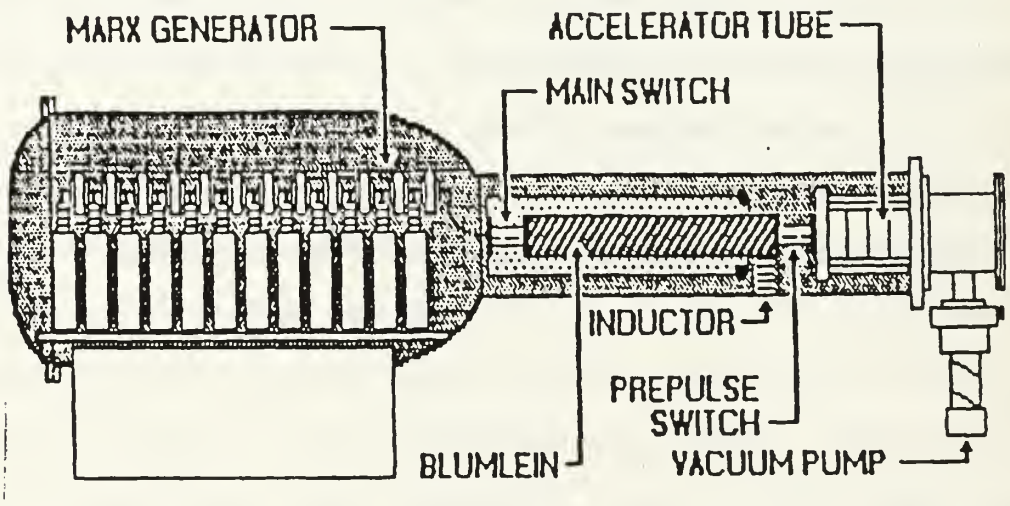

Figure A.1 Diagram of Pulserad 112A components.

The key component is the Marx Generator. The Marx Generator is a capacitive storage device in which a bank of capacitors are charged slowly in parallel and then discharged quickly in series. This results in the output voltage equalling the charging voltage multiplied by the number of capacitors in the bank. Figure A.2 depicts a simplified schematic of a Marx Generator with only four stages. The NPS

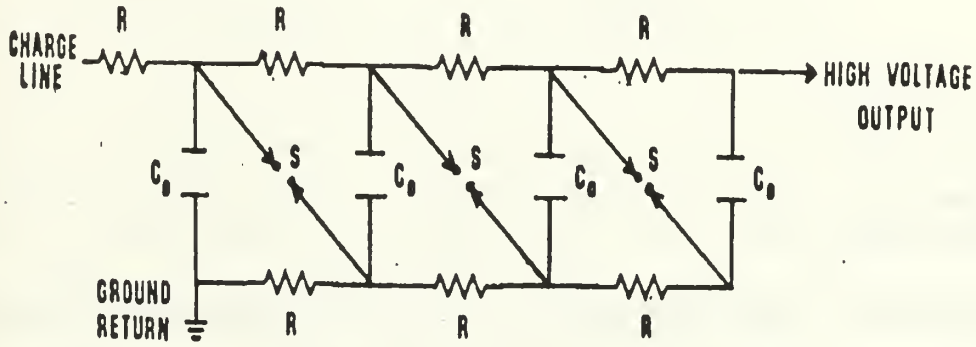

Figure A.2 Simplified schematic of a Marx generator.

Marx Generator has twelve stages with a maximum charging voltage of 100 kV and a maximum stored energy of 3 kJ. The raw pulse (referred to as the Marx voltage) has a full width at half maximum (FWHM) between 150 to 200 ns and a maximum peak voltage of 1.2 MV. A typical Marx voltage waveform is shown in Figure A.3. The switches between the stages are sulfur hexafluoride filled spark gap switches. These are

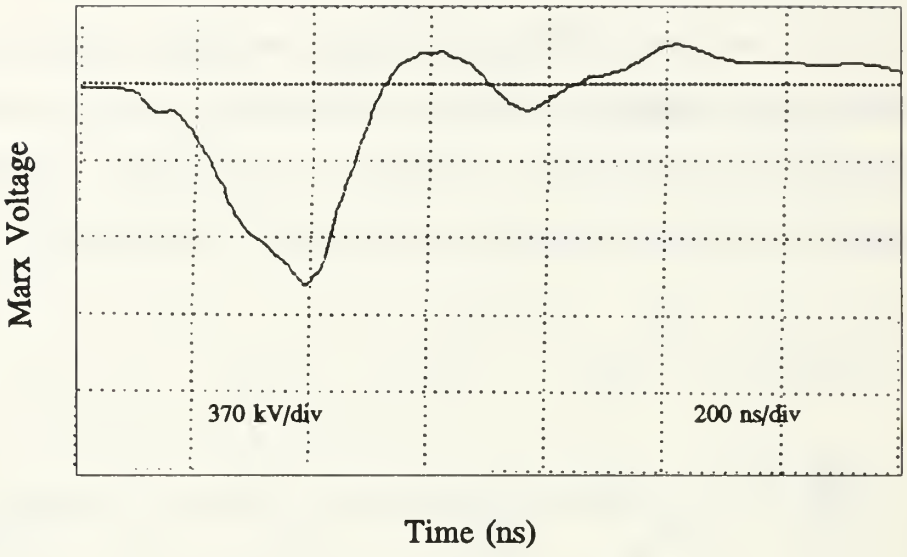

Figure A.3 Typical Marx voltage waveform for a 75 kV Marx Bank charge.

essentially just diodes filled with pressurized gas and a triggering electrode in the center to initiate breakdown. The sequential triggering of these switches to "erect" the Marx bank is a source of "jitter" between initiation of the firing of the machine and the arrival of the voltage pulse at the diode end of the machine. The resistors are all liquid resistors composed of plastic tubes filled with copper sulfate.

The next major component is the Blumlein Pulse Generator. The Blumlein circuit of the Pulserad 112A is composed of three concentric cylinders which form two coaxial transmission lines (see Figure A.4). The pulse from the Marx Generator is

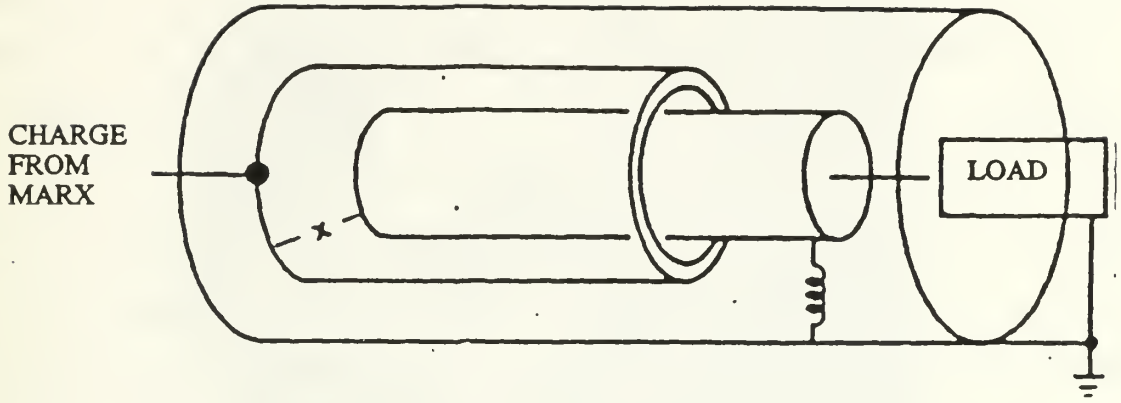

Figure A.4 Basic Drawing of a Blumlein Pulse Forming Line.

applied to the center cylinder with the inner and outer cylinders at ground potential. The innermost transmission line is shorted out when the pulse arrives, causing a reflected pulse of the same polarity as that in the outer transmission line [Ref. 13]. The composite pulse is of higher voltage and narrower width than the original pulse from the Marx Generator. The maximum output voltage from the Blumlein Generator is 1.7 MV with a 20 ns FWHM pulse. The final component to be discussed here is the Electron Accelerator Tube. The Electron Accelerator Tube is essentially a vacuum diode with a smaller diameter (3.15 cm) cylindrical solid stainless steel cathode and a larger

diameter (10.16 cm) flat tantalum foil anode (see Figure A.5). The entire diode end of the machine had to be modified for this experiment as discussed in the next section. The vacuum in the diode must be better than 5x10-4 torr for proper operation [Ref. 11]. Figures A.6 and A.7 are photographs of the diode end of the Flash X-ray machine prior to modifications. The voltage and current pulses across the vacuum diode are referred to as the diode voltage and the diode current. Figures A.8 and A.9 show typical diode voltage and diode current waveforms.

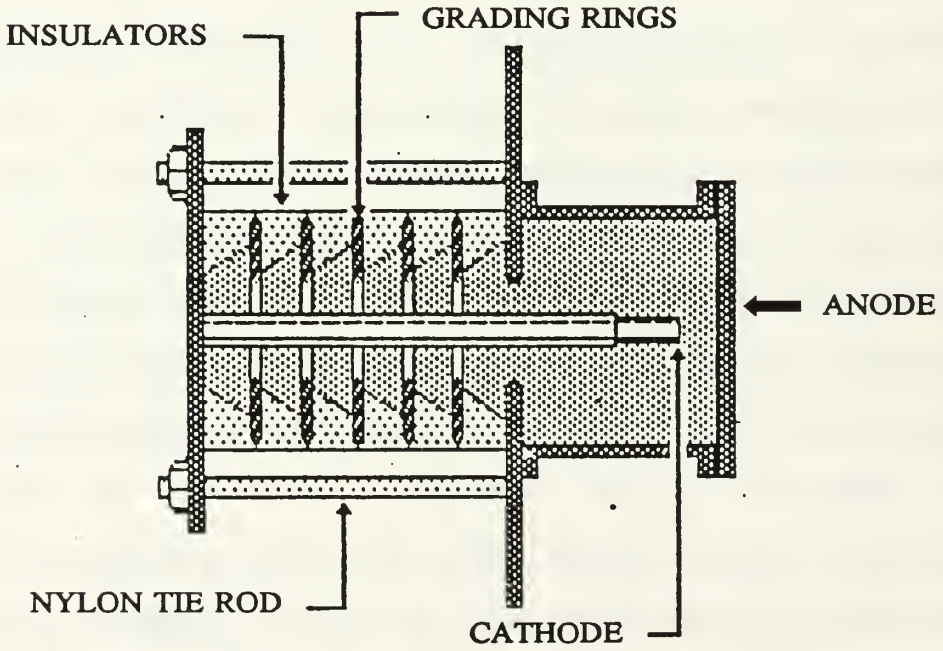

Figure A.5 Pulserad 112A Electron Accelerator Tube.

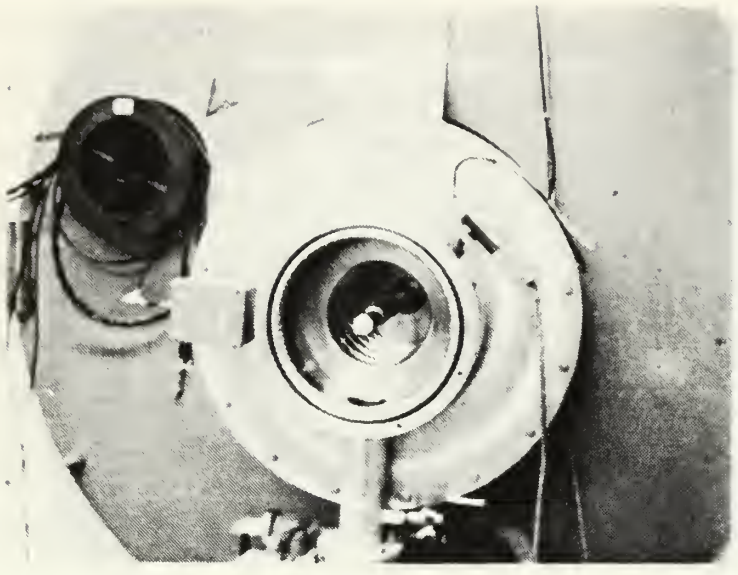

Figure A.6 Diode End of Pulserad 112A with anode plate removed.

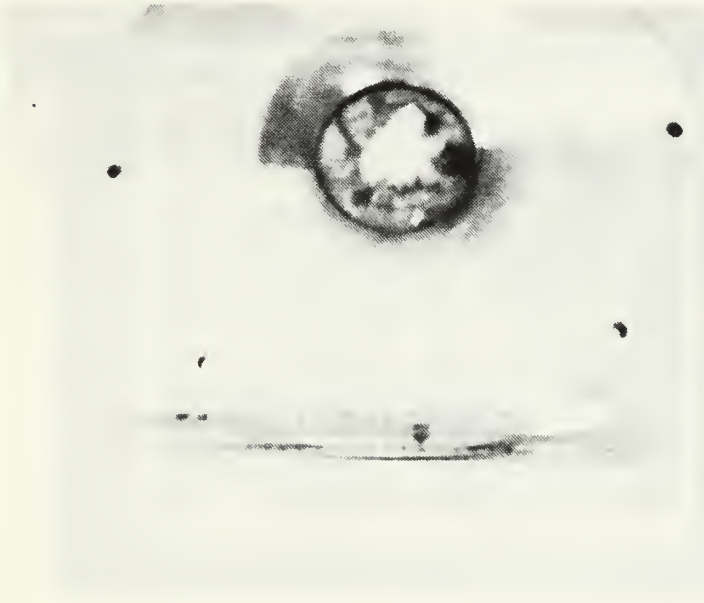

Figure A.7 Anode plate of Pulserad 112A. Tantalum foil in center.

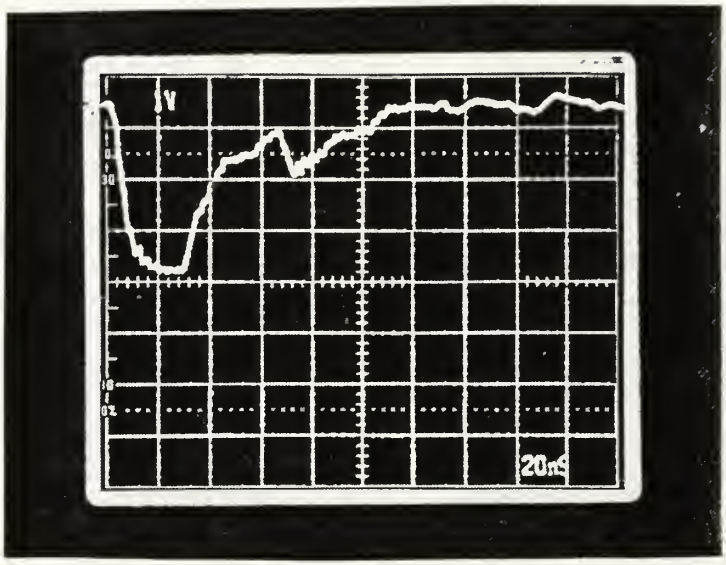

Figure A.8 Typical diode voltage waveform for a 75 kV shot (observed with 46dB attenuation at oscilloscope).

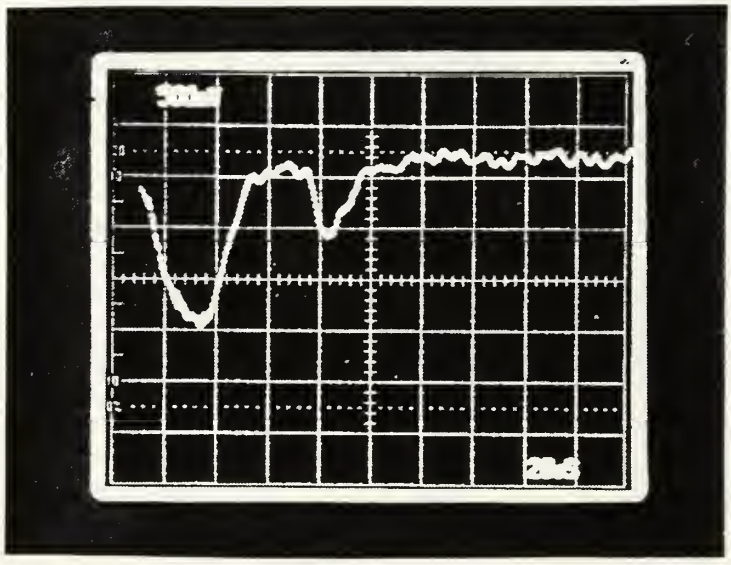

Figure A.9 Typical diode current waveform for a 75 kV shot (20 dB attenuation at oscilloscope).

B. MODIFICATIONS TO THE FLASH X-RAY MACHINE

The Flash X-ray Machine, as it previously existed, did not allow for direct observations of conditions inside the diode. To facilitate the experimental portion of this thesis, an observation window was installed. The existing design did not provide room for a window to be added, thus the vacuum diode end of the machine was extended with a window chamber. A four inch diameter replaceable pyrex window was used on the window chamber. The cathode and anode of the diode were redesigned such that the center of the cathode-anode gap could be viewed through the center of the window. The cathode was simply extended to reach the center of the window. The anode was significantly altered. The new anode is much thicker than the old anode and it is made of stainless steel instead of tantalum. The new anode has a diameter of 7.62 cm. Figure A.10 is a photograph of the modifications. Figures A.11 and A.12 contain detailed drawings of the modifications.

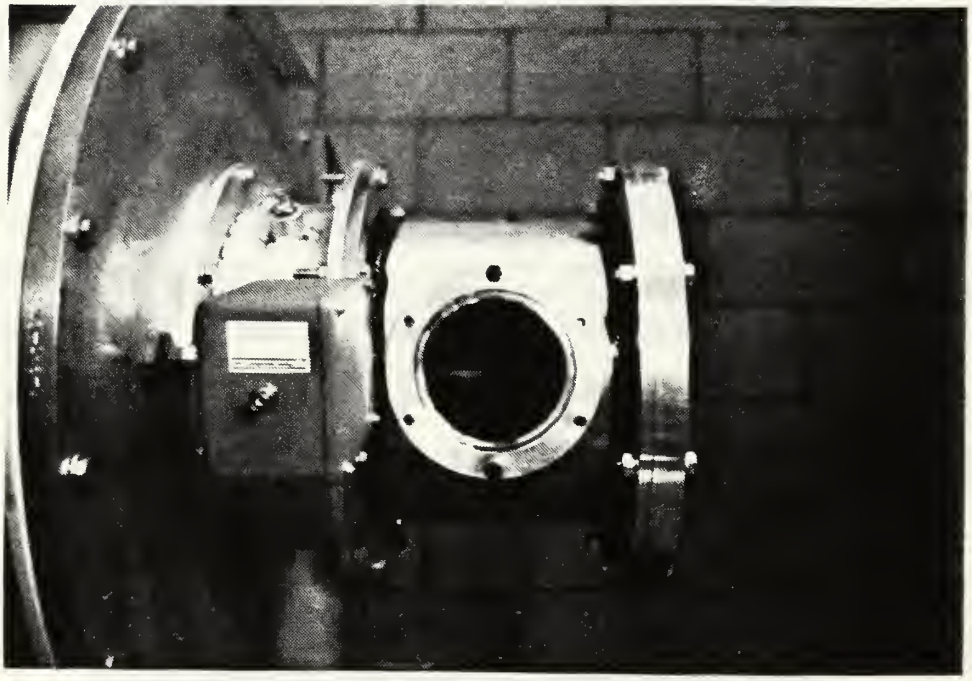

Figure A.10 Window chamber installed on Pulserad 112A. Cathode on left and anode on right as viewed through window.

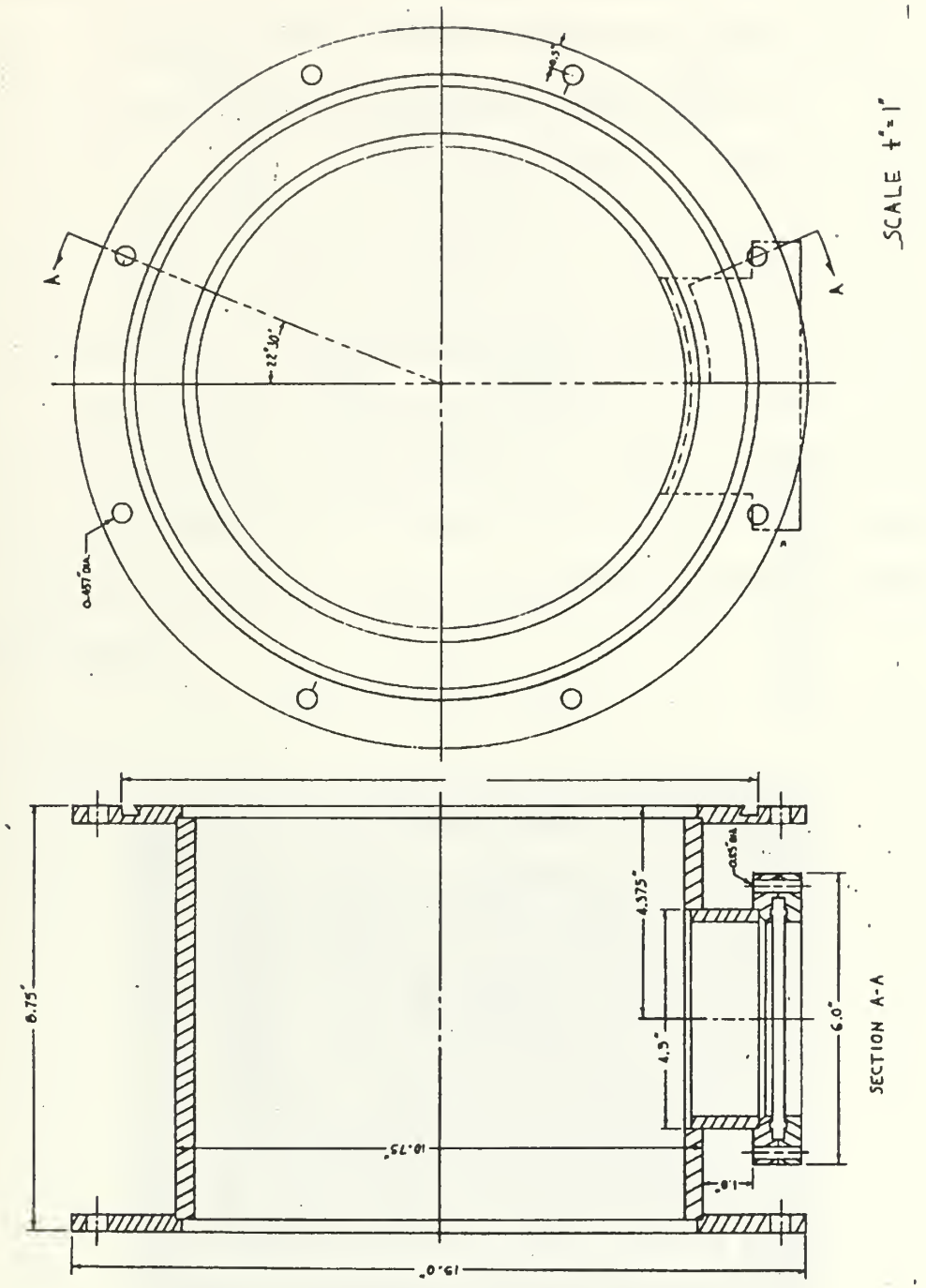

Figure A.11 Drawing of windowed vacuum chamber.

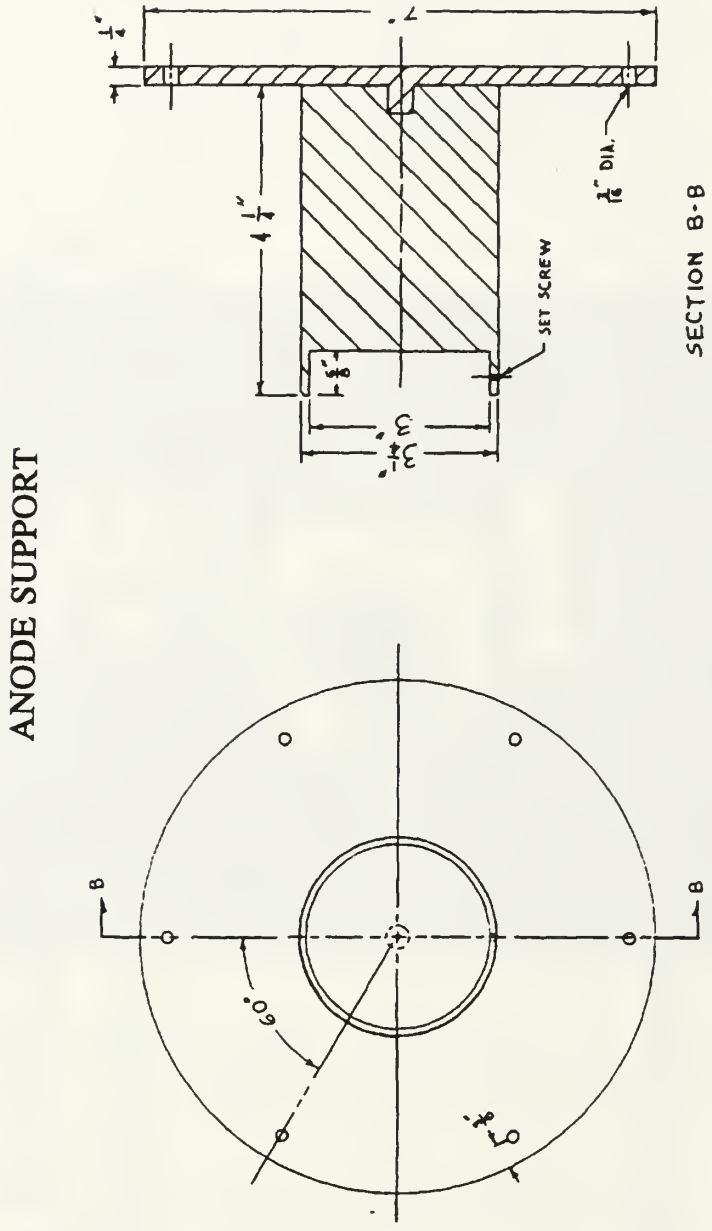

Figure A.12 Drawing of anode modification. Actual anode surface is a 2.54 cm thick 7.62 cm diameter stainless steel disk which is inserted into the indent and affixed with set screws.

The modifications to the Flash X-ray machine did not significantly alter the conditions inside the diode of the machine. Figures A.13 and A.14 show the voltage and current pulses through the diode after the modifications. The only significant change to the machine is that the x-ray production is drastically reduced. This is due to use of stainless steel anode instead of tantalum. The x-rays are also shielded more by the thick anode design. A typical x-ray dose at the end of the machine for one 75 kV shot prior to modification was 700 to 900 rad. After modification, a typical x-ray dose for one shot is 3 to 5 rad. The reduced x-ray production does not hinder the plasma experiment conducted in this thesis.

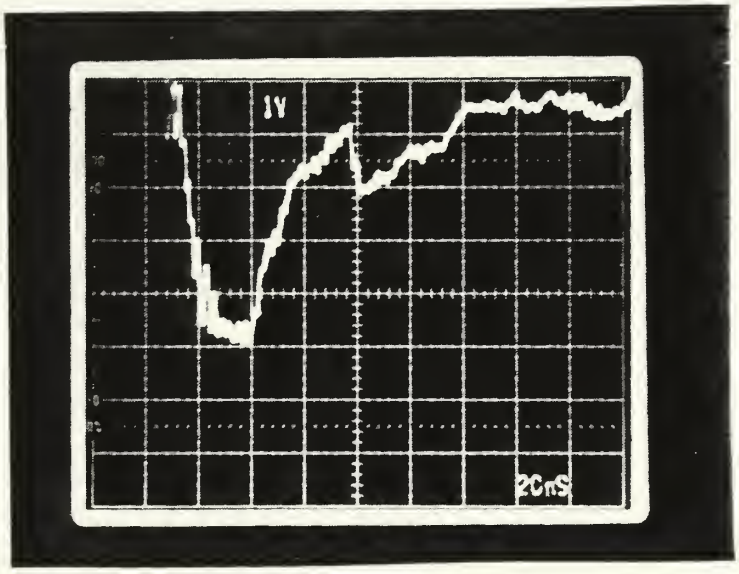

Figure A.13 Typical diode voltage waveform for a 75 kV shot (46 dB attenuation at oscilloscope).

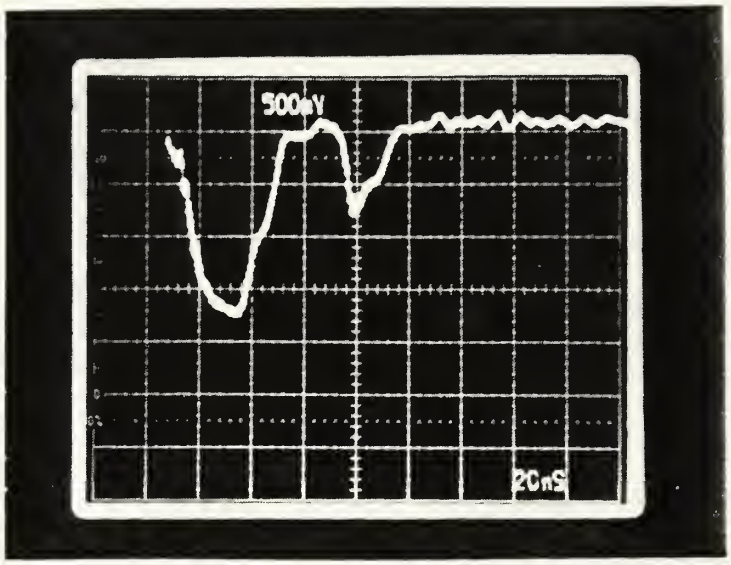

Figure A.14 Typical diode current waveform for a 75 kV shot (20 dB attenuation at oscilloscope).

All of the modifications to the Flash X-ray machine have been designed such that they can easily be reversed to conduct radiation exposure experiments. To reverse the modifications, simply unbolt the window chamber and reinstall the old cathode and anode.

APPENDIX B - SENSORS USED

A. DIODE VOLTAGE SENSOR

1. Description

The Diode voltage on the NPS Flash X-Ray machine is measured by the PIM-197A-25 voltage divider. The primary divider is a flexible tube of electrolyte which is approximately 40 cm long. The important specifications of the PIM-197A-25 are listed in Table B.1 [Ref. 14]. The sensor is designed to match a 50 ohm oscilloscope input impedance.

Table B.1 CHARACTERISTICS OF DIODE VOLTAGE SENSOR.

Peak design voltage (MV)	2.0
Maximum pulse length at full voltage (ns)	200
Resistance (ohms)	1480
Risetime (ns)	1.5
Sensitivity (kV/V)	1.6
Accuracy (%)	± 5

2. Interpretation of waveforms

To convert the oscilloscope traces into a diode voltage reading, the sensitivity of the detector as well as the attenuation used at the oscillocscope input must be taken into account. In this work, 46 dB attenuation was used at the input of the oscilloscope when monitoring diode voltage. This reduced the input voltage to the oscilloscope by a factor of 200. The formula to convert the oscilloscope trace into diode voltage is

$$V = \frac{V_o}{attenuation} \times sensitivity = V_o \times 200 \times 1.6 \qquad \textbf{(B.1)}$$

where V_o is the voltage (in volts) as read on the oscilloscope and V is the diode voltage measured in kilovolts [Ref.13].

B. DIODE CURRENT SENSOR

1. Description

The diode current on the NPS FXR machine is measured by the PIM-199B fluxmeter. The fluxmeter is a single-turn,inductively coupled flux probe which gives an output voltage proportional to the flux linking the turn [Ref. 15]. The important specifications of the PIM-199B fluxmeter are listed in Table B.2. This sensor is designed to match a 50 ohm oscilloscope input impedance.

Table B.2 CHARACTERISTICS OF DIODE CURRENT SENSOR.

Loop diameter (cm)	2.5
Risetime (nsec)	0.4
Sensitivity (V/T)	875
Peak operating level (T)	0.4
Distance from center loop to center of cathode (cm)	12.8
Accuracy (%)	± 5

2. Interpretation of waveforms

The diode voltage waveforms taken in this work used 20 dB attenuation of the oscilloscope input. This attenuation reduces the signal by a factor of 10. The formula to convert the oscilloscope trace into diode current is

$$I = \left(\frac{V_o}{attenuation}\right) \times \frac{2\pi R}{\mu_o \times sensitivity} = 7.31 \times V_o \quad \textbf{(B.2)}$$

where V_o is the voltage (in volts) as read on the oscilloscope, R is the distance from the center of the cathode to the center of the detector loop, $\mu_o = 4\pi \times 10^{-7}$, and I is the diode current measured in amperes [Ref. 13].

C. PHOTODIODE

The photodiode used in this work was the Opto-Electronics Inc. PD-30-03. The PD-30-03 is a germanium avalanche type photodiode. The PD-30 is biased to -130 volts with the Opto-

Electronics Inc. PS-30 battery powered power supply. The germanium photodiode is sensitive to visible light. The relative spectral response for a typical germanium avalanche photodiode is shown in Figure B.1 [Ref. 16]. The avalanche photodiode has a very fast rise time (approximately 50 ps) as demonstrated in Figure B.2 [Ref. 17].

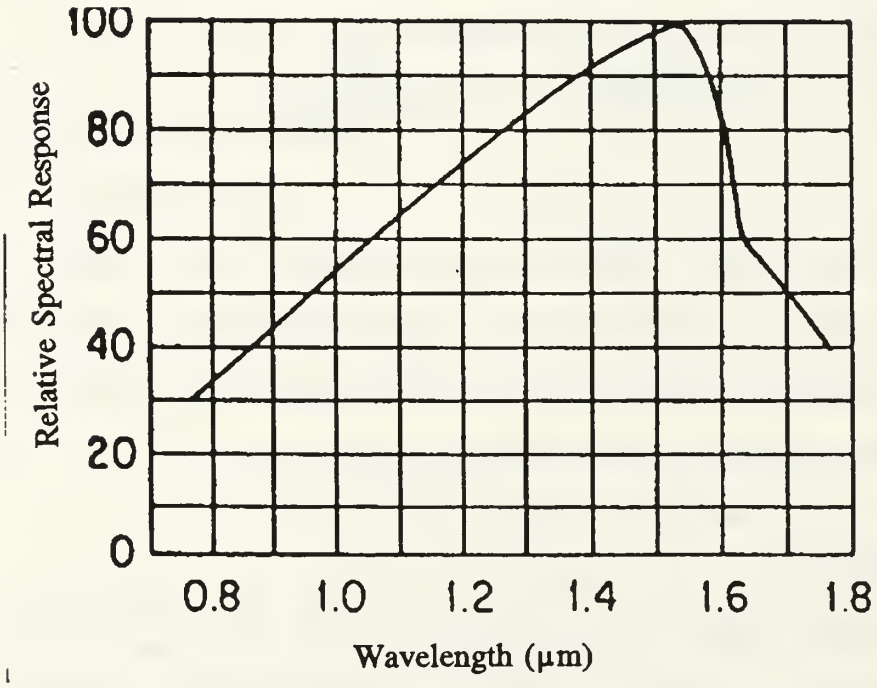

Figure B.1 Typical spectral response for a germanium photodiode [Ref.16].

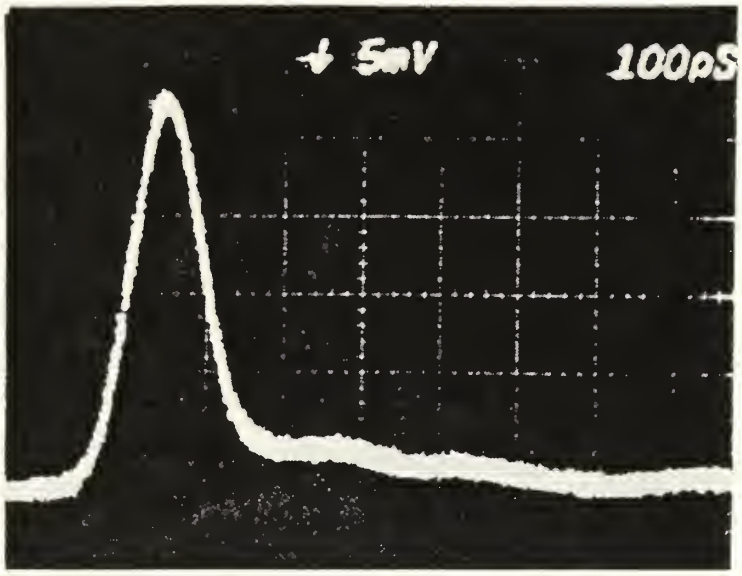

Figure B.2 Photodiode response to a 100 ps pulse.

APPENDIX C - METHOD TO SYNCHRONIZE OSCILLOSCOPE TRACES

A. DISCUSSION

Synchronization of the oscilloscope traces is essential when comparing nanosecond length pulses on different oscilloscopes. There are many sources of electrical time delay in this experiment (e.g., lengths of signal cables, attenuators, etc.). Rather than measuring each individual delay and summing the result, it was determined that measuring the delay of the entire system would be better. A multi-channel delay generator was then used to compensate for the different delays on different legs of the measured signals. Any remaining delay discrepancies are measured using the timing procedure below which produces a time delay correction. This Time Delay Correction (TDC) is then applied to the data to synchronize the different waveforms in time.

B. METHOD

The three signal paths to be synchronized were those of the diode voltage, diode current and photodiode signals. The three coaxial cables were disconnected from their detectors and connected together with Tee's at the sensor end of the experiment. The three connected cables were then connected to the output of a Hewlett Packard pulse generator. The pulse generator was set to give a 20 ns width 20 volt pulse into the

three tee'd cables simultaneously (see Figure C.1). An advance trigger was sent from the pulse generator to trigger the Stanford Research DG-535 multi-channel digital delay generator. The DG-535 was used to trigger the three oscilloscopes. Different delays were set for each channel of the DG-535 so that the signal from the pulse generator was captured at the same position on each oscilloscope even though the signal paths were different lengths.

A slight modification to this idea was necessary for the photodiode signal cable. The use of a 3 meter long fiber optic bundle between the plasma event being monitored and the photodiode introduces an optical delay which must be considered. The optical delay was determined to be 18 ns (see Appendix D). To account for this optical delay during the oscilloscope synchronization procedure (timing procedure), the trace on the photodiode oscilloscope was set to begin 18 ns sooner than the trace on the diode voltage and diode current oscilloscopes.

Due to the difficulty in precisely aligning the oscilloscope traces, photographs of the traces were taken upon arrival of the timing pulse. Any difference in arrival time of the pulse on different oscilloscopes can then be accounted for by a delay correction. The Time Delay Correction will be applied by the individual when he interprets the actual waveform photographs. For example, say the simultaneously sent pulse from the signal generator begins at 30 ns on the

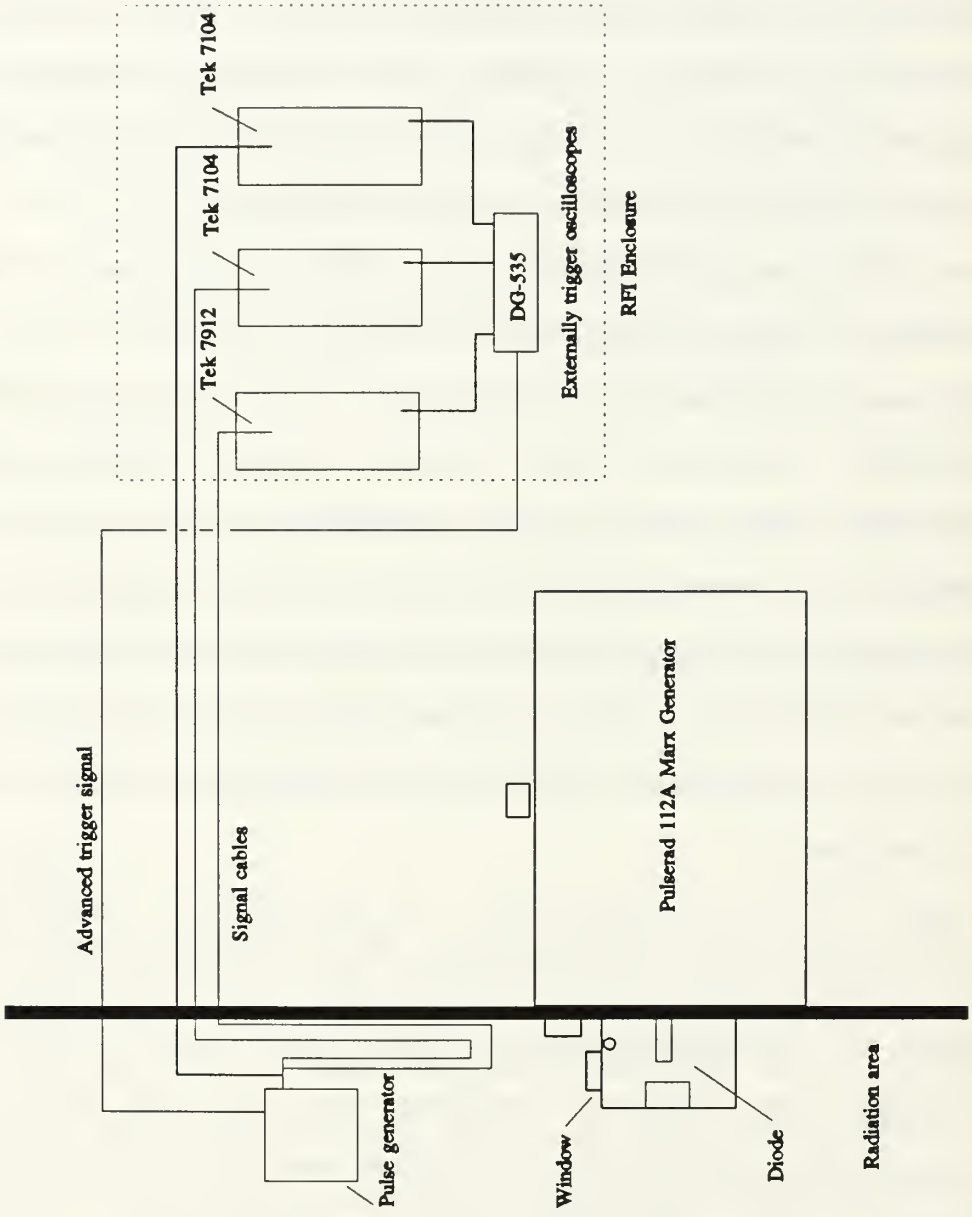

Figure C.1 Schematic drawing of setup to synchronize oscilloscope traces.

diode voltage oscilloscope and 31 ns on the diode current oscilloscope. This indicates that the signal path for the diode current oscilloscope is 1 ns longer than the signal path of the diode voltage oscilloscope. To synchronize the two waveforms when interpreting the data, the individual must subtract 1 ns from the diode current waveform using the diode voltage waveform as a reference.

C. TIMING PROCEDURE

1. Step 1

Connect the signal cables and trigger cables in accordance with Figure C.1.

2. Step 2

Set the pulse generator to deliver a manually triggered single pulse of 20 ns width.

3. Step 3

Set the pulse generator advance trigger to approximately 100 ns.

4. Step 4

Set the oscilloscopes on the desired settings which will be used for the experiment.

5. Step 5

Open the shutters on the three oscilloscope cameras.

6. Step 6

Manually trigger the pulse generator.

7. Step 7

Close the shutters on the cameras and remove the exposed film.

8. Step 8

Compare the three traces to obtain the Time Delay Corrections. This is done as follows:

- Use the diode current timing pulse as a reference.
- Compare diode voltage timing pulse to the reference to determine the Time Delay Correction for diode voltage signal.
- Add 18 ns to photodiode timing pulse and then compare to the reference to determine the Time Delay Correction for photodiode signal.

D. OSCILLOSCOPE TIME BASE CORRECTIONS

1. Comparison of Time Bases

After the experiment was completed, it was discovered that the three oscilloscopes had significant time base sweep speed discrepancies. The time bases of the three oscilloscopes were compared using a calibrated Tektronix model 2901 time mark generator. Eight periods of a 5 ns period sine wave was the signal used to compare the oscilloscopes. The results of the comparison are given in Table C.1.

Table C.1 DETERMINATION OF TIME BASE CORRECTION FACTORS.

Oscilloscope (referred to by sensor usually monitored)	Tek HB7912 with 7B90P time base (Diode current)	Tek 7104 with 7B92A time base (Diode Voltage)	Tek 7104 with 7B92A time base (Photodiode)
Response to 40 ns signal	39.7 ns	37.0 ns	38.3 ns
Percentage error	.8%	7.5%	4.3%
Time Base Correction Factor (TBCF)	1	40/37	40/38.3

The diode current oscilloscope % error is small enough to be neglected in this experiment. The diode voltage and photodiode waveforms must be corrected for the time base discrepancies by multiplying by the Time Base Correction Factors given in Table C.1.

2. Effect of Time Base Correction on Timing Procedure

The time base correction discussed above had to be applied to the timing procedure photographs prior to calculating the time delay correction. All of the digitized waveforms of Chapter V have the time base correction factor as well as the time delay correction included.

APPENDIX D - OPTICAL DELAY DETERMINATION

A. DISCUSSION

The light emitted from the plasma must travel 61 cm through the vacuum chamber and lens system and then through 3 m of fiber optic bundle to reach the photodiode. The synchronization procedure described in Appendix C requires that the optical delay correction be determined.

If the index of refraction of the fiber optic bundle were precisely known, a simple calculation would determine the optical delay. Since the index of refraction of the fiber optic bundle was not known, the optical delay had to be determined experimentally.

B. EXPERIMENTAL DETERMINATION OF OPTICAL DELAY

1. Setup

Figure D.1 shows the setup used to determine the optical delay of the fiber optic bundle. A Xenon Corporation model 437A Nanopulser (Nanolamp) was used as the light source. The Nanolamp delivers a 20 ns width light pulse. The Nanolamp was placed at the center of a 20 cm radius arc of three photodetectors. The PD-30 was used to trigger the DG-535 which in turn triggered the two oscilloscopes. One EG&G FND-100 photodiode was used as a reference signal. The Tektronix HB7912 oscilloscope was used to monitor the reference

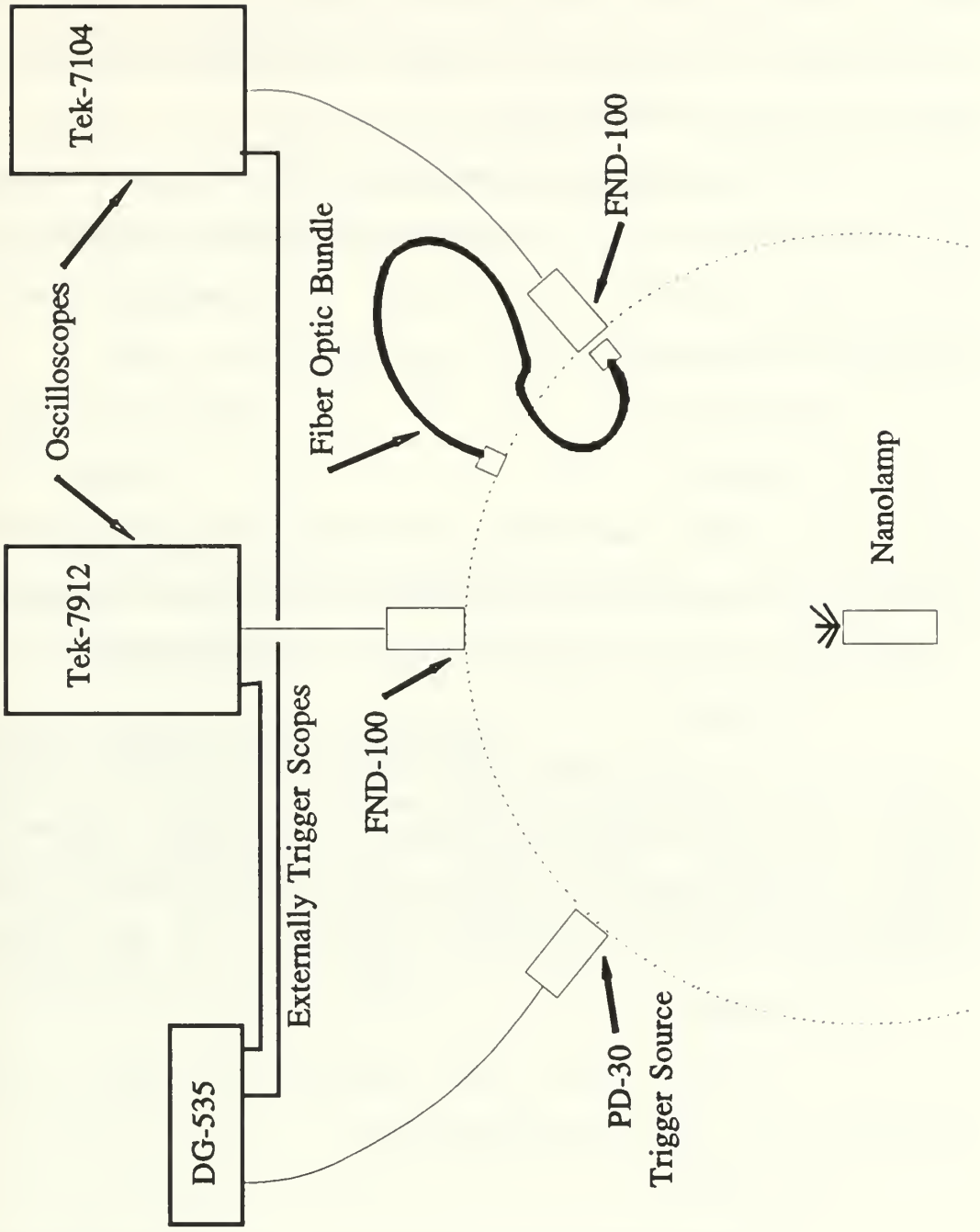

Figure D.1 Schematic drawing of experimental setup to determine optical delay. Actual length of trigger cabling is much shorter than signal cabling.

photodiode. One end of the fiber optic bundle was placed on the arc while the other end was fed into a second FND-100 photodiode. The second FND-100 signal was monitored on a Tektronix 7104 oscilloscope.

The signal cables between the FND-100 photodiodes and the oscilloscopes were of the same length. The oscilloscope time base corrections described in Appendix C were also applied as required.

2. Procedure

a. Step 1

First the fiber optic bundle was removed from the aperture of the FND-100 photodiode so that the Nanolamp could illuminate both FND-100 photodiodes simultaneously.

b. Step 2

The Nanolamp was triggered and the photodiode signals were photographed at the oscilloscopes. Comparison of these two photographs determine the relationship between the "reference leg" and the "measurement leg" of the experiment.

c. Step 3

Step 2 above was repeated 10 times so that an average value could be determined.

d. Step 4

The fiber optic bundle was re-installed such that one end was on the arc and the other end was fed into the FND-100 photodiode.

e. Step 5

The Nanolamp was triggered and the photodiode signals were photographed at the oscilloscopes. Comparison of these signals and application of the relation between the reference leg and the measurement leg (Step 2 above) allowed determination of the optical delay.

f. Step 6

Step 5 was repeated ten times so an average value could be determined.

3. Results

The optical delay due to the fiber optic bundle was determined to be 16 ± 1ns. The ± 1ns is based on the error analysis of Appendix E.

C. TOTAL OPTICAL DELAY CORRECTION

The light signal in the plasma experiment must travel 61 cm before reaching the fiber optic bundle. This corresponds to a 2 ns delay. Therefore, the total optical delay correction is 18 ± 1ns.

APPENDIX E - ERROR ANALYSIS

A. VOLTAGE MEASUREMENTS

This section applies to all measurements involving signals read as vertical deflections on the oscilloscopes. Table E.1 gives the accuracies of the components involved in voltage measurements.

Table E.1 VOLTAGE AND CURRENT ACCURACIES.

PIM-197A-25 or PIM-199B*	+/- 5%
Oscilloscope vertical plug-in (7A29 or 7A16P amplifiers)*	+/- 2%
Value of attenuation**	+/- 5%
Visual interpretation of trace#	+/- 10%

* Based on manufacturer's specifications.
** Estimated error.
# Estimate based on experimenter's experience.

These fractional errors are independent and can be added in quadrature [Ref. 18]. Therefore, the total error in voltage measurements is ± 12 %.

B. TIME MEASUREMENTS

Table E.2 gives the accuracy of the components involved in time measurements made on the 5 ns/division sweep speed.

Table E.2 TIMING ACCURACIES.

Oscilloscope time bases (7B92A or 7B90P)*	± 3%
DG-535 absolute error*	± 500 ps
DG-535 RMS jitter*	± 50 ps
Visual interpretation of trace**	± 0.3 ns

* Based on manufacturer's specifications.
** Estimate based on experimenter's experience.

The oscilloscope time base error is a fractional error which ranges from 0.1 ns to 1.2 ns over the center eight divisions on the 5 ns/division sweep speed. This error analysis will be performed for an absolute oscilloscope error of 0.6 ns since most of the signals of interest were measured near the beginning or center of the oscilloscope traces. Once again the errors are independent and can be added in quadrature. Therefore, the total error in time measurements is ± 0.8 ns. This error will be rounded to ± 1 ns.

C. OPTICAL SIGNAL TIMING

The time measurement error analysis above also applies to the experimental determination of the optical delay of the fiber optic cable (Appendix D). Since there is ± 0.8 ns error in determining the optical delay correction, the corrected photodiode waveforms have a total error of ± 1.6 ns. This error will be rounded to ±2 ns. These errors were not added in quadrature because they both came from the same source.

APPENDIX F - DATA

Tables F.1 through F.3 display the data used to compute the average values of delay of plasma formation and average diode voltage at onset of plasma formation for each data run presented in Chapter V. Figures F.1 and F.2 graphically display the given data.

Table F.1 RESULTS OF THE 55 kV DATA RUN.

Shot #	Delay of Plasma Onset (ns) ±2	Diode Voltage at Plasma Onset (kV) +80/-120
34	6.2	384
35	5.6	384
36	6.7	384
38	7.1	384
40	5.6	384
41	5.1	320
42	6.7	416
43	6.0	416
44	5.6	416

Table F.2 RESULTS OF THE 75 kV DATA RUN.

Shot #	Delay of Plasma Onset (ns) ±2	Diode Voltage at Plasma Onset (kV) +100/-150
7	4.6	704
8	6.1	576
9	6.2	640
10	4.6	640
11	4.9	576
12	5.5	608
13	7.1	640
14	6.0	640
15	5.5	640
16	5.0	640

Table F.3 RESULTS OF THE 100 kV DATA RUN.

Shot #	Delay of Plasma Onset (ns) ± 2	Diode Voltage at Plasma Onset (kV) +500/-300
23	3.9	576
24	3.6	576
25	2.7	576
26	3.3	576
27	3.5	576
28	3.0	448
29	3.8	544
30	4.5	800
31	4.7	640
32	2.7	480
33	4.5	640

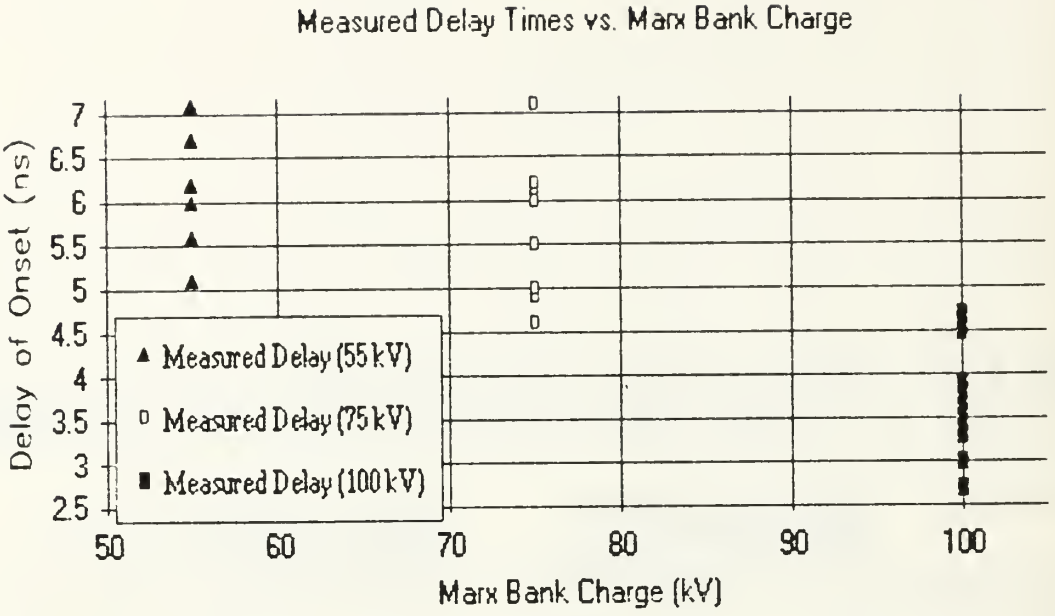

Figure F.1 Delay Time of Plasma Onset vs. Marx Bank Charge for the 55 kV, 75 kV and 100 kV Data Runs.

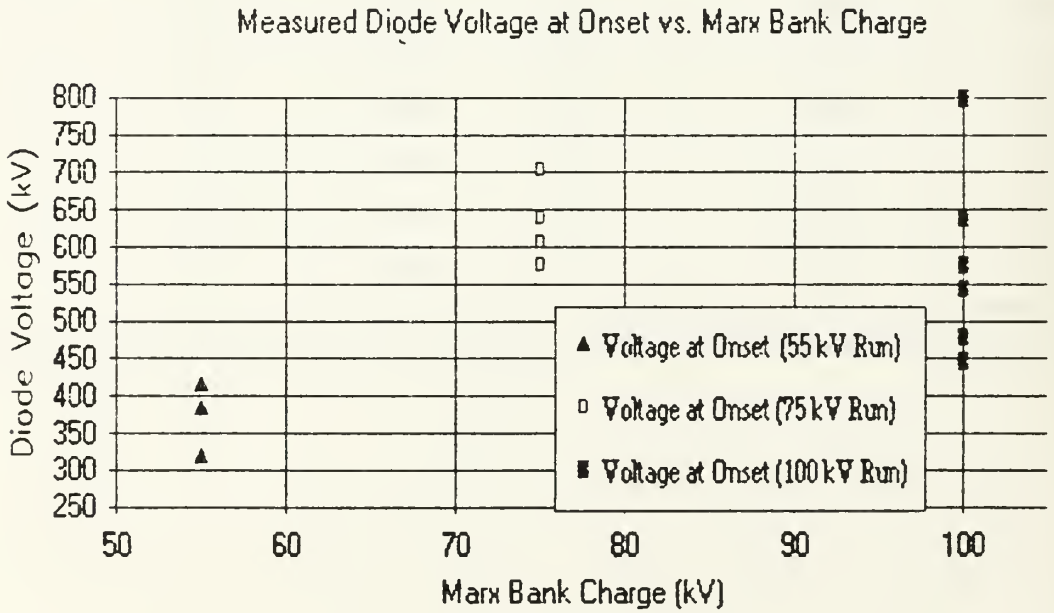

Figure F.2 Diode Voltage at Plasma Onset vs. Marx Bank Charge for the 55 kV, 75 kV, and 100 kV Data Runs.

LIST OF REFERENCES

1. "Onset of Breakdown in a Vacuum Diode", F. Schwirzke, X.K. Maruyama, S.A. Minnick, Proceedings of the Eighth International Conference on High-Power Particle Beams, Vol. 2, World Scientific, Singapore, p. 958,1991.

2. Hinshelwood, D., Explosive Emission Cathode Plasmas in Intense Relativistic Electron Beam Diodes, Ph.D. Dissertation, Massachusetts Institute of Technology, Cambridge, MA,January 1985.

3. Minnick, S.A., Unipolar Arcing on the Cathode Surface of a High Voltage Diode, Master's Thesis, Naval Postgraduate School, Monterey, California, December 1989.

4. Miller, R.B., An Introduction to the Physics of Intense Charged Particle Beams, Plenum Press, 1982.

5. Mesyats, G.A., and Proskurovsky, D.I., Pulsed Electrical Discharge in Vacuum, v.5, Springer-Verlag, 1989.

6. Schwirzke,f., "Laser Induced Breakdown and High Voltage Induced Vacuum Breakdown on Metal Surfaces" to be published as a chapter in a book: Laser Interaction and Related Plasma Phenomena, H. Hora and G.H. Miley, ads., Plenum Publishing Corporation, forthcoming in 1991.

7. Bulletin of American Physical Society, Schwirzke, F., and Hallal, M.P.,Jr., "Explosive Plasma Formation on Electrodes," paper presented at the Annual Meeting-APS Division of Plasma Physics, 32nd, Cincinnati, Ohio, 12-16 November 1990.

8. Barnett, C.F., Ray, J.A., and Thompson, J.C., Atomic and Molecular Collision Cross Sections of Interest in Controlled Thermonuclear Research , p. 141, Oakridge National Laboratory, August 1964.

9. Journal of Nuclear Materials 128 & 129, Unipolar Arc Model, by F. Schwirzke, pp. 609-612, 1984.

10. Galarowicz, D., Instrumentation Requirements for Tree Effects Data Collection at the Naval Postgraduate School Flash X-Ray Facility, Master's Thesis, Naval Postgraduate School, Monterey, California, June 1990.

11. Physics International Company, Model 112A Pulserad pulsed X-Ray Generator Operations and Maintenance Manual, January 1986.

12. Physics International Company, Model 112B Pulserad X-Ray Generator Operations and Maintenance Manual, February 1987.

13. Pietruska, R.B., Operation and Characteristics of the Flash X-Ray Generator at the Naval Postgraduate School, Master's Thesis, Naval Postgraduate School, Monterey, California, June 1989.

14. Physics International Company," PIM-197 Voltage Dividers Data Sheet," March 1978.

15. Physics International Company, "PIM-199 Fluxmeters data sheet," October 1981.

16. Handbook of Optics, Walter Driscoll and William Vaughan, eds., p.4-39, Mcgraw-Hill Publishing Co., 1978.

17. Opto-Electronics Inc., Operations Manual for Series PD-30 Ultra High Speed Photodetector, Oakville, Ontario, Canada, February 1983.

18. Taylor,J.R., An Introduction to Error Analysis, Oxford University Press, 1982.

INITIAL DISTRIBUTION LIST

		No. Copies
1.	Defense Technical Information Center Cameron Station Alexandria, Virginia 22304-6145	2
2.	Library, Code 52 Naval Postgraduate School Monterey, California 93943-5002	2
3.	Dr. K. E. Woehler, Code PhWh Department of Physics Naval Postgraduate School Monterey, California 93943-5100	1
4.	Dr. F. Schwirzke, Code PhSw Naval Postgraduate School Monterey, California 93943-5100	5
5.	Dr. X. K. Maruyama, Code PhMx Naval Postgraduate School Monterey, California 93943-5100	3
6.	Physics Library, Code Ph Department of Physics Naval Postgraduate School Monterey, California 93943-5100	2
7.	LT Michael P. Hallal, Jr. 8333 Benjamin St. Chalmette, Louisiana 70043	2
8.	Mr. Harold Rietdyk, Code Ph Accelerator Laboratory Department of Physics Naval Postgraduate School Monterey, California 93943-5100	1
9.	Mr. Donald Snyder, Code Ph Accelerator Laboratory Department of Physics Naval Postgraduate School Monterey, California 93943-510	1
11.	Mr. Bernie Bernstein Physics International Company P.O. Box 5010 San Leandro, California 94577-0599	1

Thesis
H16117 Hallal
c.1 The onset of breakdown
in a fast pulsed vacuum
diode.